Investigation for Mechanism of Earthquake Occurrence and Relationship Upheaval and Subsidence Based on Structural Geology

January 2015

Tsuneo OHSUMI

Investigation for Mechanism of Earthquake Occurrence and Relationship Upheaval and Subsidence Based on Structural Geology

A Dissertation Submitted to
the Graduate School of Life and Environmental Sciences,
the University of Tsukuba
in Partial Fulfillment of the Requirements
for the Degree of Doctor of Philosophy in Science
(Doctoral Program in Earth Evolution Sciences)

Tsuneo OHSUMI

Contents

Chapter1: Vein Structure

Chapter 2: Boundary conditions for realistic crustal movement along strike-slip faults: constraints based on numerical and analog model experiments

Chapter 3: Strong Motion Evaluation for the AD 365 Crete Earthquake

Chapter 4: Investigation of Rock Thin Sections from Landslide Screes due to the 2008 Eastern Honshu Earthquake

Abstract

According to da Vinci, man was placed at the center of the universe may seem a truism, and man was the model as the center microcosm reflected in the macrocosm. That was where one had to start and that was where one had to end if one truly intended finding the general law holding together the universe.

To investigate any “Fractural mechanism”, is needed to look at it from the microscopic level, magnified level, aerial level and satellite level. Vein structure is the starting point of the fault rupture shape. In the field of structural geology, the formation of regularly arrayed vein structures present in rock thin sections, organize the relationship between the distance and the generation process of cracks formed on the surface of the seafloor by an earthquake. With vein structures of several mm, there is a commonality with the echelon cracks of strike-slip faults. The relationship of traces on the Earth's surface due to an earthquake fault, is also in relationship to upheavals and subsidence. The upheaval caused by the AD 365 earthquake on the Greek coast in the Holocene period records the event to this day. In this study ground motion estimations by the stochastic Green’s function method were applied.

Photomicrograph investigation of rock thin sections taken from landslides’ scree and seismic waveforms of the Aratozawa landslide (estimated by empirical Green’s function method based on empirical site amplification and phase effects) from the Eastern Honshu Earthquake, 2008. Thus, large acceleration caused landslides in these areas. Since the first activity of Kurikoma volcano 50,000 years ago, the volcanic ash has been spread widely throughout the western area from the volcano. In the photomicrograph investigations,

factors for each scale of collapse pattern and rock materials were investigated. Thus, this proves that sediments from the caldera period accumulated on the large scale pyroclastic flow sediments which filled the caldera. This study found, that the Aratozawa landslide was lateraly spread on a slippery stratum. Also, that many landslides were translational slides of the bedding plane-slide type.

In Chapter 1, Vein structure, a distinctive structure in deep-sea hemipelagic clayey and siliceous mudstones at convergent plate boundaries, consists of closely spaced mud-filled veins forming an array usually parallel to the bedding plane. This structure has been regarded as a seismite that formed during earthquake shaking by resonance of fractures. The detailed field observations and shaking model experiments verified that both basic (first-stage) and advanced (developed-stage) vein structures can be explained by a systematic theory. Essentially, a vein structure forms in an array of fractures as a result of shearing, not by push waves but by shear waves of very short wavelength, by a mechanism very similar to that which forms ripple marks. This study found the height of a vein array (H) to be systematically related to vein spacing (S) such that $H=5S$, suggesting that the shear strength of the sediment is proportional to the thickness of the standing wave part of a sediment layer. Shear or oscillatory flow occurs in the top part of a sediment layer, under which standing waves with wavelengths on the order of millimeters to centimeters lead to vein structure formation. Vein structure can develop not only in response to earthquake shaking but also by propagation of shear waves along a large fault or by other kinds of shears associated with debris flows, landslids or faulting.

In Chapter 2, Strike-slip movement along active fault regions affects small-scale fractures and topography as well as large-scale topography over long periods. This study aims to model fracture patterns in a simple-shear regime. An analog dislocation model experiment using rubber and quartz powder and dynamic and nonlinear finite element method numerical experiments were carried out. In the analog experiment, at both ends of the shear box, clockwise rotation of blocks was generated, indicated by the discontinuous displacement of the markers. In a strike-slip fault, fractures are generated in the region under tension of dilatation. In the strike-slip numerical experiments, fractures were simulated in a sedimentary layer under three types of boundary conditions: both ends fixed, both ends free, and one end fixed with the other free. The various boundary conditions produced different results, including geometric dilatation produced by extensional basins and the development of sag ponds along the strike-slip fault. We discuss these features in relation to large-scale tectonic formations in Japan, including 100-km-scale active faults in the geological fault line passing through the middle of Japan, where the movement was found to be either fixed or free at both ends, or one end fixed and the other free.

In Chapter 3, Seismicity in Mediterranean sea and evaluation of the strong motion applied for the AD 365 Crete Earthquake by the stochastic Green’s Function West Asian region is a very active area of a crustal deformation, many historically huge earthquakes have occurred, there and crustal movement has continued up to today. To investigate the most suitable solution for the crustal movement will contribute greatly to this region’s earthquake and tsunami disaster mitigation. Pirazzoli *et al.* (1996) suggests that traces of upheaval caused by the AD 365 earthquake on the Greek coast in the Holocene shows the event which occurred in the period called the Early Byzantine tectonic paroxysm (EBTP) turbulent period from the mid-4th to the mid-6th centuries. Evidence of a 9 m upheaval by the AD 365 earthquake movement was found in a detailed survey and by radiocarbon dates by Pirazzoli *et al.* (1996), the date of the casualties' were estimated from coins found in a collapsed house by Stiros (2010), and by the ruins of an old harbor that existed, give the proof of the position of the sea surface at that time by the location of the quay wall. Applying the crustal upheaval modeling, which along/within a subduction plate, study by Fischer (2007), Shaw *et al.* (2008) and Stiros (2010) using the calculation formula of Okada (1992). This study selected the most reliable parameters, which each researcher defined, and non-uniform distribution in the fault plane, which is based on Papadimitriou *et al*. (2008). Next, ground motion estimation by the stochastic Green's function method using the selected parameters. This study used realistic phases from earthquake records of the Crete Island, M_w6.4, 12 Oct. 2013 and the aftershock. Comparison of the estimated velocity and the Earthquake map of the Crete Island (Sieberg, 1932), the areas stretching from Chania and Iraklio are expected to be high seismic intensity areas.

In Chapter 4, Photomicrograph investigation of rock thin sections taken from landslides scree by the Eastern Honshu Earthquake, 2008. Housing damage due to this earthquake was quite light. On the other hand, heavy damage was sustained due to landslides. It was pointed out that large-scale landslides occurred around the Aratozawa area which lies to south of the Kurikoma mountain caldera. Since the first activity of Kurikoma volcano 50,000 years ago, the volcanic ash has been spread widely throughout the western area from the volcano. In this study, the scale of the caldera is compared to that of the landslides. At Aratozawa landslide point, the estimated ground acceleration was approximately 3 G. Thus, large acceleration caused landslides in this area. Seismic waveform at the Aratozawa

landslide was estimated by empirical Green’s function method based on empirical site amplification and phase effects. Site amplification characteristics at the Aratozawa landslide were evaluated based on the aftershock observation records. Moreover, a characterized source model for strong ground motion prediction was constructed based on the results of waveform inversion for this earthquake. A sample of mudstone from Aratozawa point consisted of lamination, and sand mud alternating strata. Diatoms can be seen clearly in the mudstone taken from Aratozawa Point. Thus, this proves that sediments from the caldera period accumulated on the large scale pyroclastic flow sediments which filled the caldera. Based on the photomicrograph investigations, factors for each scale of collapse pattern and rock materials were investigated.

Key words : vein structure, experiment, strike-slip fault, AD 365 Crete earthquake, earthquake ground motions, Green’s function, Eastern Honshu Earthquake, landslides, photomicrograph

List of Figures

Chapter1

Chapter 2

Chapter 3

Chapter 4

Chapter 5

Appendix

List of Table

Chapter 3

Chapter 0

Overview

In **Chapter 1** and **Chapter 2**, the phenomenon of basic rupture zone features and progressive evolution of vein structure was investigated by analog experiment and numerical experiment. In **Chapter 3** and **Chapter 4**, as an application for society in which human beings live, this study investigated how strong ground motion would influence upheaval and subsidence and the ensuing danger to human life.

Chapter1 investigated the regularity of the vein structure found in the Boso Peninsula. Vein structure, a distinctive structure in deep-sea at convergent plate boundaries, consisted of closely spaced mud-filled veins forming an array usually parallel to the bedding plane, and also investigated the relationship between the different layers at the boundary. As a result, first, the regular spacing order within a single array reflects mechanical resonance. Second, the constant ratio between array height and vein spacing further shows what factor reacts to what factor in resonance. Third, is the shape of the veins and their arrangement that cause reflects Riedel shearing. These three factors must be explained to resolve the true mechanism of vein structure formation.

Chapter 2 (investigated by analog experiment). Reproduced the origin of the fracture surface and showed a different shape of the destruction in the extension field and contraction field. Also, Chapter 2 (investigated by numerical experiment). Validated the analog experiment, and the association with the formation of topography in nature. As a result, the analog experiments revealed that fractures were generated in a strike-slip fault. At both ends of the fault, the fracture shape was controlled by clockwise rotation. The numerical experiments revealed that the boundary conditions had a significant influence on the stress required to initiate fault rupture.

Chapter 3 is based on the evidence from the ancient upheaval of the AD365 Crete earthquake in Greece, to validate the parameters of the earthquake from a large number of researchers. This study estimated the ground motion by using the stochastic Green's function. Also, this study verified the collapse status of masonry structures from the ground motion. In addition, ground motion of the deposited layer in urban areas was also calculated. This study suggests that those areas are still in lurking danger of ground motion amplification. As a result, in the north-west of Crete is expected to be high seismic intensity area. Thus, it is necessary to pay attention to the seismic risk at the high densely area with thick sedimentary layers.

Chapter 4 used the empirical Green's function on aftershock records from Aratozawa point that caused a large-scale collapse during The Eastern Honshu Earthquake 2008. The estimated large ground motions were obtained and this study investigated the relationship between the collapsed factors and the destabilizing factors. As a result, the estimated ground acceleration is approximately 3 G. Thus, large ground motion caused landslides in this area at Aratozawa landslide point.

Chapter1

Vein Structure

1. Introduction

Vein structure was first reported on land from outcrops of Neogene deep-sea, clayey, siliceous (mostly diatomaceous) hemipelagic sedimentary rocks on the Miura and Boso peninsulas, central Japan (Ogawa, 1980; Hanamura and Ogawa, 1993). Similar structures have been recognized in DSDP-ODP cores, mostly from trench slopes, for example, from the Mid-America trench off Guatemala (Cowan, 1982; Ogawa and Miyata, 1985; Helm and Vollbrecht, 1985), the Japan trench (Arthur et al., 1980; Leggett et al., 1987; Knipe, 1986), the Izu-Bonin trench (Ogawa *et al.*, 1992), and the Chile trench (Kemp and Lindsley-Griffin, 1990; Kemp, 1990; Lindsley-Griffin *et al.*, 1990), as well as in many on-land examples from the Monterey and Santa Cruz formations, California (Brothers *et al.*, 1996).

The major characteristics of vein structure have been well described by Brothers *et al.* (1996). The veins of a vein structure are regularly spaced, forming an array subparallel to the bedding plane, and filled with fine, dark materials (dominantly clay or mica minerals) (**Fig. 1**). The veins themselves may be straight and vertical, or sigmoidal to varying degrees and either S- or Z-shaped (**Figs. 1 and 2**). Vein structures develop in sediments of limited age and lithology, and with a limited distribution, implying that their formation is controlled by specific conditions.

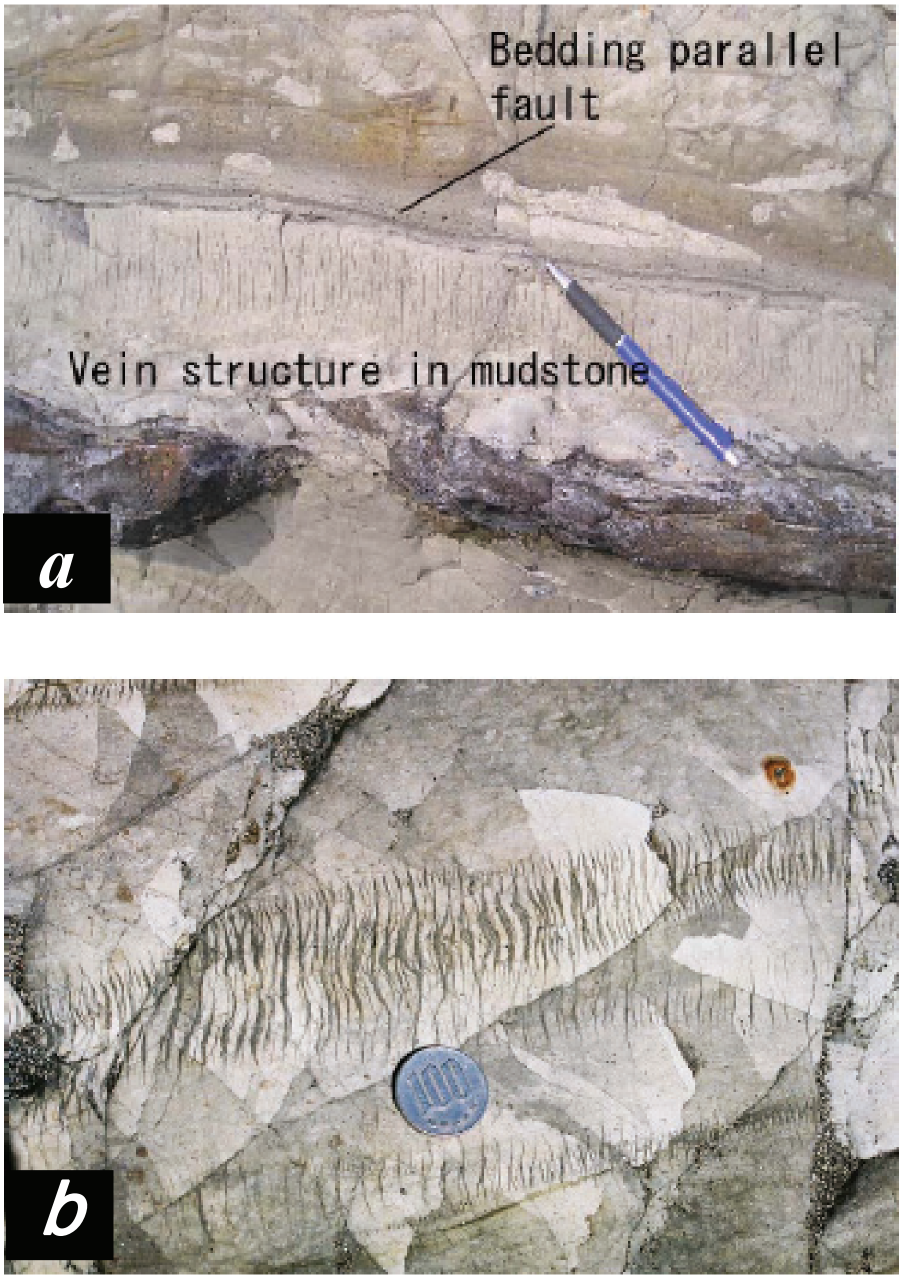

Fig. 1. Typical vein structures in upper Miocene diatomaceous mudstone, Boso Peninsula, Japan. a) Example from Nishikawana, showing a vein array formed below a bedding-parallel fault. b) Example from Motoda, showing high, bold veins with a sigmoidal shape, in between which some shorter, thinner veins are developed. Coin is 22 mm in diameter.

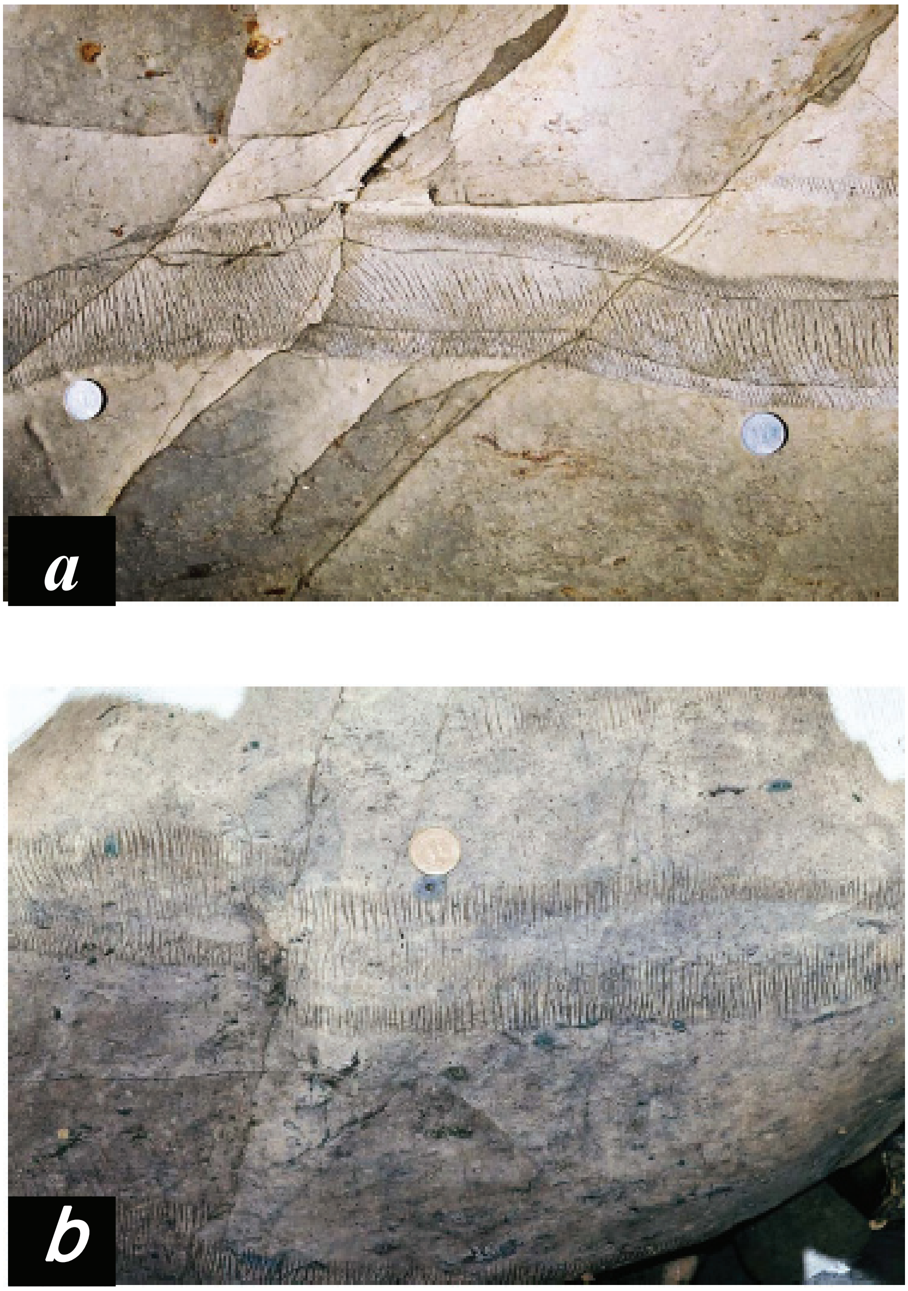

Fig. 2. Typical vein structures at Shimatogura, Boso Peninsula, showing good examples of resonance. a) The spacing ratios of the veins are 1:1/2:1/3 from wide to narrow veins. b) The spacing ratios of the veins are 1:1/2:1/3:1/4. Coin is 20 mm in diameter.

In an experimental study, Brothers *et al.* (1996) attributed the origin of vein structures to strain waves propagating between an upper liquefied sediment part and a relatively strong lower sediment part in which standing pressure waves form systematic fractures (veins) alternating with ghost veins during seismic wave shaking (vibration). Brothers *et al.* (1996) considered the responsible waves to be a combination of shear and pressure waves, but they did not explain the critical relationship between vein shape and arrangement regularities nor its cause. In this study, on the basis of field observations and experimental results, we explain the origin of the arrangement regularities by shearing in a liquefied sediment layer above the standing wave layer in which the vein structure forms.

This study found three regularities during our critical observations in the field in the Boso Peninsula. First, the regular spacing order within a single array reflects mechanical resonance. Second, the constant ratio between array height and vein spacing further shows what factor reacts to what factor in resonance. Third, is the shape of the veins and their arrangement reflects Riedel shearing. These three regularities must be explained to resolve the true mechanism of vein structure formation.

The theory of direct origin by seismic waves cannot easily account for the wave type that is responsible for the fractures, namely one with a very short period on the order of millimeters to centimeters. Snell's law for seismic wave transmission explains that earthquake body waves approach the surface in an almost vertical direction as *P*-waves and *S*-waves. Horizontal transmission along the earth's surface occurs by surface waves such as Love and Rayleigh waves. During a large earthquake lasting tens of seconds to some minutes, the land surface close to the hypocenter shakes strongly, with a dominant frequency of approximately 0.5 to 2 Hz.

Earthquake waves have a wavelength some kilometers long, which is too long to be responsible for the millimeter to centimeter vein spacing. Therefore, such earthquake waves cannot directly cause vein structure formation. Another theory is needed to explain the various modes of the regular occurrence of vein structures, including the regular spacing and array height–vein spacing relationship.

Moreover, vein structures sometimes exhibit an *X*-shaped arrangement where two vein arrays intersect, one with *S*-shaped veins and the other with *Z*-shaped veins. These are commonly associated with bedding-parallel faults. This study discuss the geological implications of this vein structure arrangement later.

2. Vein shape and spacing and the array height–vein spacing relationship

2-1. Resonance

The spacing of the veins of a vein structure is very systematic. Spaces between veins are usually one to several millimeters wide and up to several centimeters long, and the spacing is extremely regular within a particular array (**Figs. 1 and 2**). Within a single array, there may be several vein types of different heights (long or short) and width (bold or thin) and with different forms. This study recorded the spacing of veins by measuring how many veins of each specific type occurred within a 10-cm array length on photographs taken at outcrops with a vertically exposed plane at right angles to the strike of the vein surface.

This study found a fractal relationship within the spacing ratio for vein types (ordered from long to short), that is, 1:1/2:1/4:1/8, etc. (normalized as 1 is the width of the longest vein with the widest spacing). In addition, this study recognized an order including odd numbers in some cases: 1:1/2:1/3:1/4:1/5, etc. (**Fig. 2**).

The relationship 1:1/2:1/4, etc. was reported previously by Brothers *et al.* (1996), who also recognized the resonance. However, they did not explain the origin of such short spacing. In addition, with regard to the resonance, what is its mechanical cause? What kind of wave causes vein structure to form?

2-2. Array height–vein spacing relationship

Brothers *et al.* (1996) plotted array height and vein spacing in exposures of the Monterey Formation in California and in ocean cores drilled off Chile. They reported no systematic relationship between array height and vein spacing, perhaps because they could record only the apparent spacing, because the measured surfaces were not always at right angles to the strike of the vein surface.

This study plotted the height of the vein array (*H*) against the vein spacing (*S*) of the basic, main (**Figs. 1 and 2**). This study found, both for vein height shorter than 1 cm as well as for longer ones (several to tens of centimeters at maximum), a systematic relationship of $H = 5S$ (**Fig. 3**), where *H* is the height of the array and *S* is the vein spacing within the array, although in some examples, the fit was better with multipliers larger than 5. It is clear, however, that at minimum, the height of a vein array is five times the vein spacing.

As already noted by Ogawa and Miyata (1985), Hanamura and Ogawa (1993) and Brothers *et al*. (1996), each vein in a vein structure is a fracture filled with fine, clayey particles. In addition to the relationship between the height of the vein array and vein spacing, the thickness of the individual veins may be related to the sediment strength, because the degree of fracturing depends on sediment strength.

The millimeter spacing of veins may represent half wavelengths related to certain properties of the sediment. However, as noted in the Introduction, the wavelengths of normally transmitted seismic waves are too long to explain the vein spacing. Thus, this study now have to consider how the close spacing occurs.

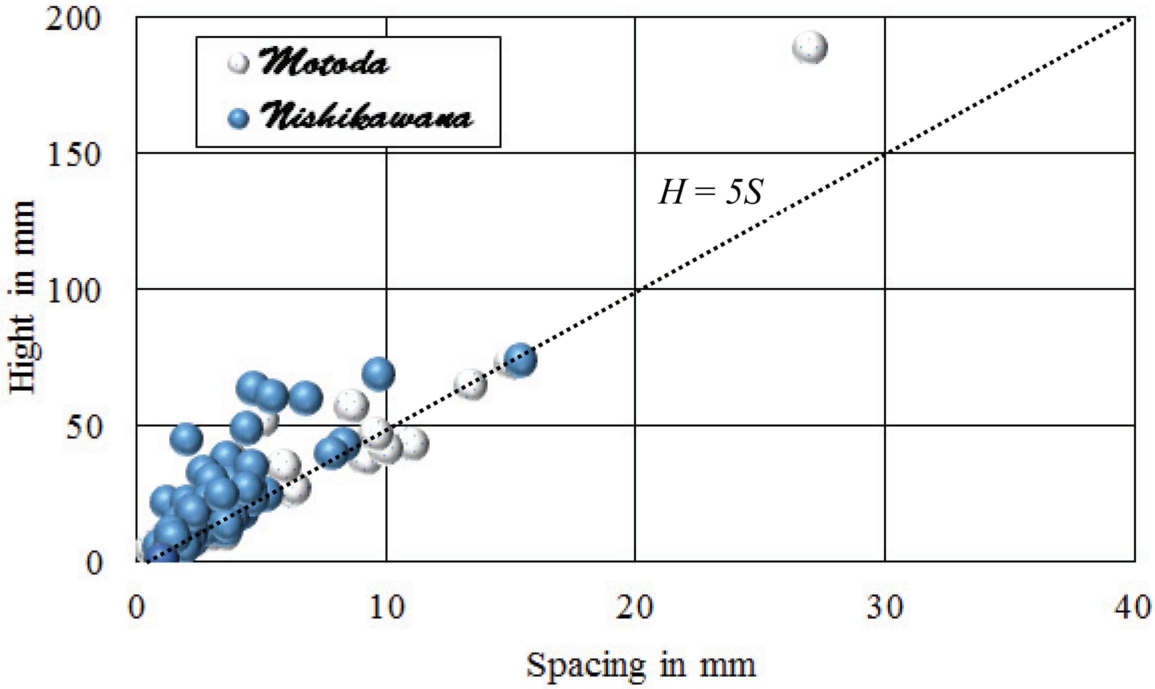

Fig. 3. Diagram showing the relation between vein spacing (*S*, mm) and array height (*H*, mm) of vein structures from two representative locations, Motoda and Nishikawana, Boso Peninsula. The lower limit suggests the strictly linear relation $H = 5S$.

Definition

The name of Riedel shear originated from the pioneer works of Riedel who first performed the shear box test, and then Skempton (1966) defined the range of the relative dislocation direction of convergence of the oblique planes to be 10 to 30 degrees, which are arranged in en echelon pattern. Riedel shears are used as in this paper.

Theory

Ideally R_1 (synthetic Riedel shear) and R_2 (antithetic Riedel shear of opposite sense) are associated, and in fact the former is dominantly observed, while R_2 is not so often observed. The process is explained as the maximum principal compressive stress axes (σ_1), occurs at approximately 45 degrees to the *Y*-plane (principal displacement shear), depending upon the Coulomb fracture theory which has shear plane with φ and $45\text{-}2\varphi$ two directions. φ is defined as an internal friction angle. In the shear plane process R_2 and R_1 stages are first developed and second *T*-plane with tension components (**Fig.4**).

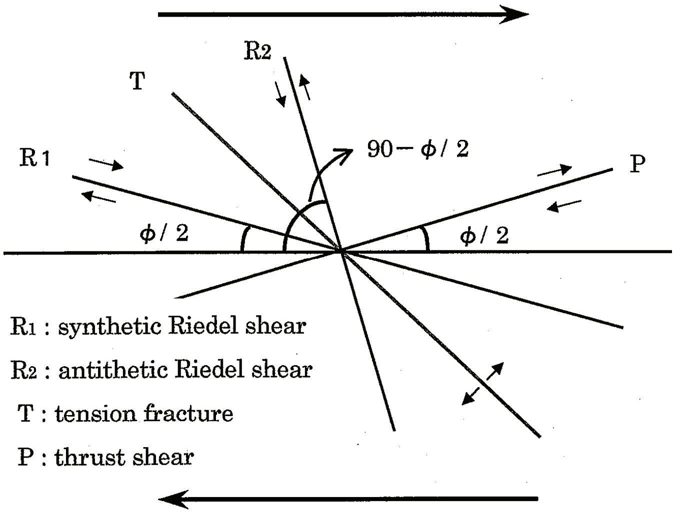

Fig.4 R_1 and R_2 are synthetic and antithetic Riedel shears respectively, and *T* and *P* are addition shear fractures developed during progressive deformation.

Hanamura and Ogawa (1993) classified layer-parallel faults, thrust duplexes, imbricate thrusts and vein structures into three stages. Vein structure comprises of bedding-parallel faulting associated with gravitational sliding and sediment injection. The earthquake shake model first proposed for vein structure, formation, by Helm *et al.* (1985), followed by Hanamura and Ogawa (1993), Brothers *et al.* (1996), which are mostly parallel to the seafloor due to compressional or shear waves.

Helm *et al.* (1985) conducted a shear box test. The vein, occurred as an antithetic Riedel (R2) shear plane was further subjected to vibration test by Hanamura (Kyushu university master degree thesis, 1992). Hanamura fixed video cameras to the shear box to observe the images of progressive evolution of the vein. From these images Hanamura was able to construct schematics that illustrated the evolution of vein structures by horizontal shaking. In this case the low shear strain had subvertical compressive stress. Rapid arrangement of veins makes an irregular spaced one. The bifurcation seemed to form by reciprocal shake, both to the left and right. Sigmoidal vein evolved. Thus, this reciprocal shake produced vein structures. This process was that horizontal dominant shears that were associated with bedding parallel faults. Next, vein occurred as an antithetic Riedel (R2) shear plane, then was subsequently rotated by synthetic Riedel (R1) shear zone. A propagated vein cut and dislocated the bedding-parallel fault in an antithetic fashion. Lastly, the next vein further cut and dislocated the former veins and faults in an antithetic fashion. However, these experiments used dry powder. Similar cases have also been observed in diatomaceous sedimentary rocks containing a vein structure in wet state.

Ogawa and Miyata (1985) analyzed the vein structures of the deformation and tectonics of the Middle America Trench landward slope area off Guatemala in muddy sedimentary Oligocene to Miocene rocks. This progressive evolution of vein structures was in relation with liquefaction. This study used drilling samples to investigate the mode of development of veins.

3. Box experiment results and origin of the close vein spacing

3-1. Shearing below Mass movement

The phenomena observed during experimental shaking of powder, as described by Brothers *et al*. (1996), who expanded on a suggestion made originally by Hanamura and Ogawa (1993), are as follows. When a box filled with dry clay powder (10 µm in average grain size) is shaken horizontally, the surface layer of powder in the box behaves differently from the main part below. It undergoes liquefaction, which enables the surface layer to flow. Even before oscillatory shaking begins, a system of periodic fractures similar to a vein structure always forms in the main part below the surface layer soon after the box is tilted. During continuous oscillatory shaking with horizontal dislocation of several to ten cm, each cycle being one second or so, or with much faster or longer period, density flow occurs in the top several centimeters of the powder, and a standing wave forms in the denser layer below the surface layer, leading to vein structure formation (**Fig.5**). Even in wet mud, a vein structure forms, although it is less visible from outside. This study first explain the simplest case at the beginning of shaking, and then the more developed case, which occurs at a later stage.

As the box is shaken, the powder separates into two parts. The upper part behaves as if liquefied, whereas the lower part remains solid and both a standing wave and fractures form. Density and strength differ in the two parts, leading to density flow and shearing. The density flow with shear causes friction between the upper and lower parts, so that a shear wave occurs along the boundary, and fractures form in the lower part by action of this shear force.

This study performed various trials of a push wave experiment in which high-frequency shaking was achieved by a motor, and in no case did vein structures form. Therefore, push waves probably cannot directly cause a vein structure to form.

These observations suggest that shaking is a possible cause of vein structure formation, but a push wave is not. In general, density flow with shearing is a plausible cause, because it can generate short shear waves along and below the flow boundary, which create fractures and veins. Further, this mechanism can also explain later modification of the vein structure by Riedel shearing. This series of processes is illustrated in **Fig. 6** for the simplest case of top-to-the-right shaking of the box.

With oscillatory shaking, reciprocal displacement can occur along the boundary, causing first oscillatory shearing, then, finally, Riedel shearing creates a conjugate set of vein structure arrays, one with the top shear to the right, and the other with the top shear to the left. A natural example of a similar case is described later.

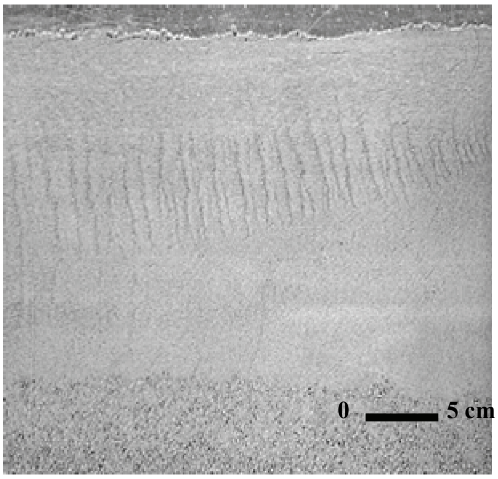

Fig. 5. Simple shaking experiment in which a basic type of vein structure formed in dry clay powder. The clear fractures (wider) are the original vein structure, and the short, slightly vague streaks are so-called ghost veins. The experiment was conducted under various conditions with the same general result. In this case, the duration was 60 s, the shaking frequency 1.4 Hz, and the oscillation amplitude 130 mm. Courtesy of Dr. D.E.Md.K. Hamed.

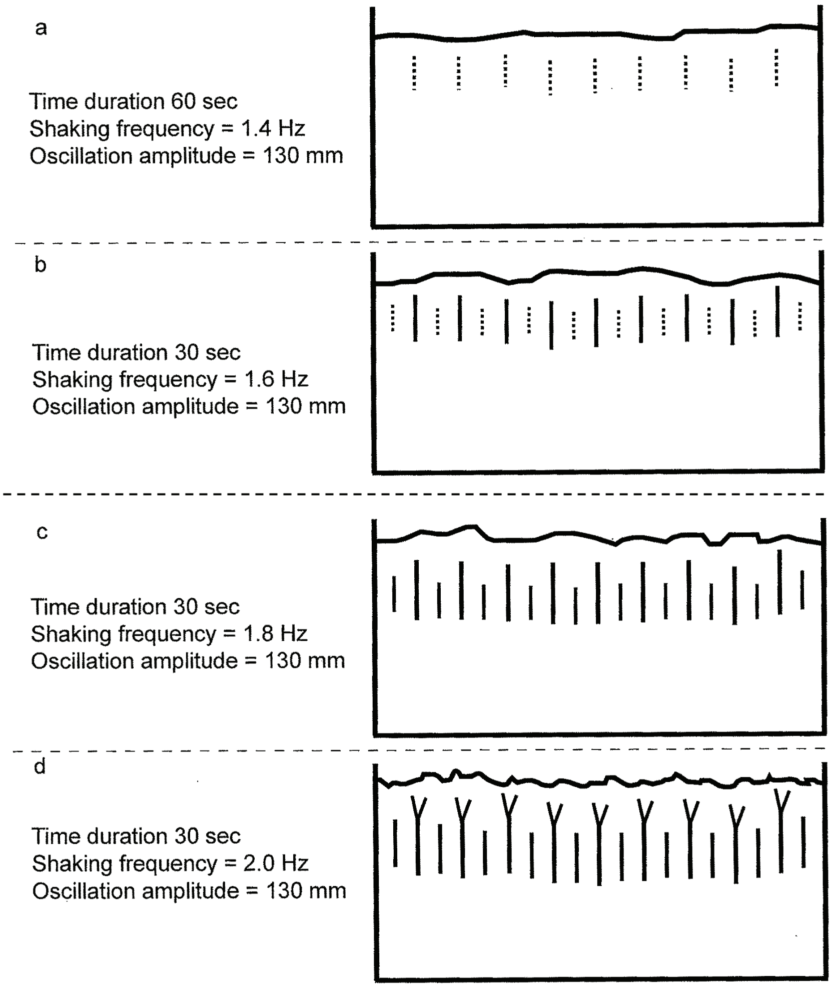

Fig.6. The progressive evolution vain structures produced during shaking experiment

3-2. Mechanism of Short Spacing: Similarity to Ripple Mark

As noted above, a shear wave occurred below the density flow, and this study propose here that the features of our model are analogous to the formation of ripple marks in stream sediments. Sedimentological studies and textbooks (Bagnold, 1946; Yalin, 1972; Inokuchi, 1975) have reported that ripple marks display a systematic relation between wavelength (λ) and the grain size (d) of the sediment, as follows:

$$\lambda = 1000\, d,$$

independent of other factors.

This observation may help us explain the formation of systematic vein structures. A ripple is a small topographic shape on the top surface of sediment underlying a flow (either a unidirectional current or oscillatory flow). The wavelength of a ripple is independent of the current velocity or the wave frequency; it depends only on the grain size, as mentioned above. If we assume that the grain size of the sediment below the flow is approximately 0.01 mm (10 μm), then λ is 10 mm, which is close to double the spacing of the common, basic vein structure. In fact, in both our experiments and field observations, the grain size was around this range.

During continuous shaking lasting at least 10 s, the veins of a vein structure became differentiated into two kinds: a fracture and a “ghost” vein, which is composed of finer materials. Brothers et al. (1996) considered the ghost veins to form at the nodes of standing waves, where finer materials became concentrated. During resonance, subsequent fractures might occur at the sites of the ghost veins, obliterating the ghost veins as a result. The spacing ratios of 1:1/2:1/3:1/4, etc. can be explained by resonance of fractures in natural numbers with the half-wave length (λ/2) as the basic spacing for the antinode.

During development, the vein fractures would become oblique to the vertical, because of dislocation by the shear stress component along an oblique plane, and then further rotated into a sigmoidal shape (**Fig. 7**, lowermost panel). The veins would become the seeming antithetic Riedel shears (*R*'), but they are not primary. In each case, the constant spacing and the periodic arrangement of both veins and ripples are important. These features can be explained by the basic spacing of the veins being proportional to the sediment grain size, which affects the strength of the specific part.

Any natural phenomenon that can cause a density flow, including landslides, debris flows, and faulting, can provide the external force to form vein structures. All are associated with high-frequency shear waves, which are needed for the formation of the regularly spaced fractures observed in vein structures. Density flows caused by landslides have a much shorter wavelength than earthquake vibrations; these waves have a frequency of 80 or higher (Ohsumi *et al.*, 2006). In an accretionary prism, much large-scale shearing occurs in association with faulting. In such circumstances, vein structures might develop over a wide area within the prism.

In the case of oscillatory shearing, for example, during earthquake vibration, reciprocal shears may occur repeatedly, forming an upper liquefied part and a lower standing wave part, in between which the oscillatory shears occur. Then, bidirectional Riedel shears can form an *X*-shape arrangement of vein structures (**Fig. 8**). One array has S-shaped veins, formed by top shear to the right, and the other Z-shaped veins, formed by top shear to the left (**Fig. 8**). This study have observed various examples caused by such oscillatory shaking, and in most cases earthquake vibration of the topmost part of the sediment was the cause of the reciprocal shear underneath. However, the basic cause of the vein structure phenomenon is not necessarily earthquake vibration but is more likely dislocation by shear stress.

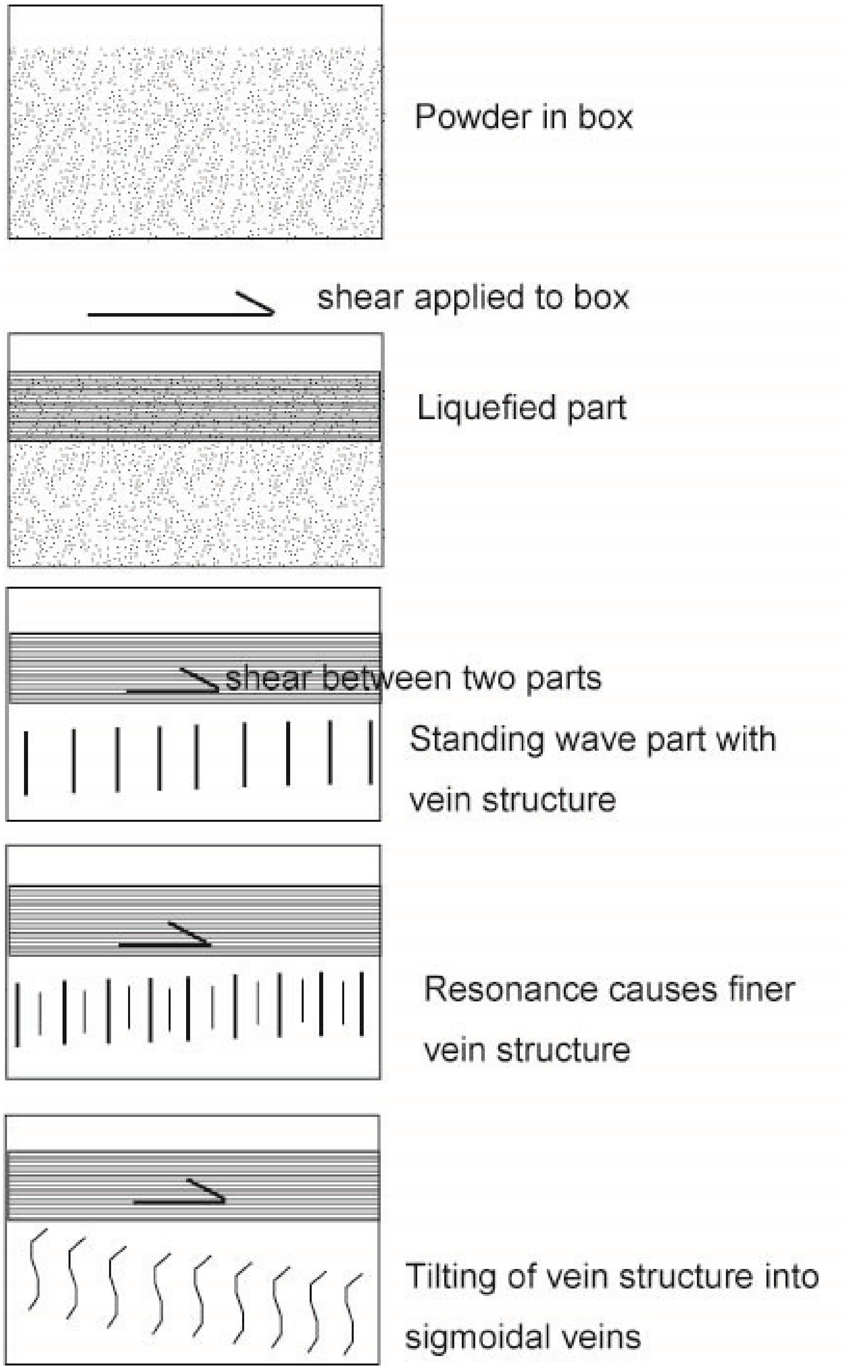

Fig. 7. Schematic diagrams showing the development of a vein structure in a shear box test. For simplicity, only the simplest example of a single shear above and to the right is illustrated. The darker top zone is the liquefied part, below which shearing occurs. Vein structures formed first as systematic fractures, then they were developed by resonance into several orders with closer spacing. Finally, veins developed in a Riedel shear zone causing the array to tilt to the right and the veins to become sigmoidal in shape.

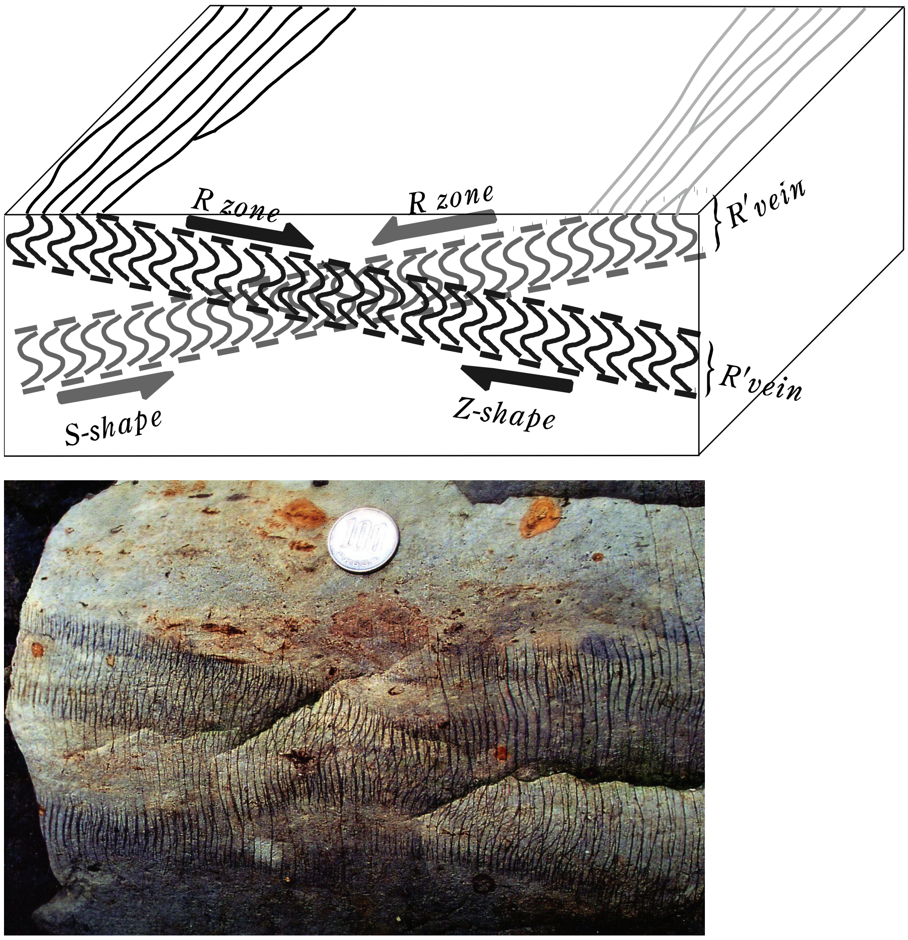

Fig. 8. Typical example of complex vein structures after oscillatory shaking by an earthquake. Two distinct vein arrays, one with Z-shaped veins and the other with S-shaped veins, were formed in Riedel shear zones (top to the right and top to the left, respectively). Sample from Shimatogura, Boso Peninsula. Coin is 22 mm in diameter.

4. Conclusions

Vein structures have been described as a kind of seismite, but careful field observation of array height versus vein spacing and the results of a clay powder box shaking experiment, along with consideration of several possible factors, suggest that vein structures are not the direct product of earthquake shaking nor necessarily of oscillatory shaking, but are caused by shearing below a bedding plane. Vein spacing is not caused by push waves but by shear waves of very short wavelength induced by the density flow, and the spacing–grain size relationship can be explained by a mechanism similar to that by which ripple marks form. The main requirement is shear or oscillatory flow directly above the zone where vein structures form, and formation of a standing wave of short wavelength (on the order of millimeters to centimeters) in the zone where the vein structure forms.

Acknowledgments

This study thank Diaa Eldin Mohamed Kamel Hamed, who helped us with the experimental work in the early part of the study. The early draft was reviewed and revised by Alexander Maltman and Nicholas Hayman, to whom we this study grateful, but this study are responsible for any errors.

Chapter 2

Boundary conditions for realistic crustal movement along strike-slip faults: constraints based on numerical and analog model experiments

1. Introduction

The 1995 Kobe Earthquake in Japan, known as "The Great Hanshin-Awaji Earthquake," and the 1999 Kocaeli Earthquake in Turkey damaged building structures and infrastructure. The damage was caused by the strong ground motion as well as strike-slip displacement along the surface faults. It is important to carefully study the cause of these surface fractures to improve earthquake-resistant design methods and thereby mitigate earthquake-related damage to buildings and infrastructure.

During the Kobe Earthquake, Riedel shear cracks appeared as surface fractures on Awaji Island (Kanaori 1997). These cracks formed under a simple-shear regime transferred from deeper levels within the crust. Riedel shears are commonly observed in nature and in laboratory experiments, but their three-dimensional (3*D*) geometric expression at the scale of 10–100 km is not yet fully understood.

To simulate the fracture patterns in a simple-shear regime, this study designed an analog dislocation model experiment using rubber and quartz powder. Furthermore, to compare the analog and numerical strain fields, this study carried out a dynamic, nonlinear numerical experiment using the finite element method (FEM). The analog dislocation experiment was performed using rubber as a sheared basement that dislocates a surface cover of powder. The shear movement in the shallow crust was simulated to produce right-lateral (dextral) shear, and the results were compared with the deformation patterns observed in natural sedimentary cover rocks in areas of active strike-slip faulting from a wide range of tectonically active regimes.

In the analog experiments, the offsets of discontinuous markers were observed, revealing regions of horizontal extension at both ends of the fractures. Dynamic and nonlinear FEM experiments were carried out under three different boundary conditions: free at both ends, fixed at both ends, and free at one end and fixed at the other. This study then considered the application of the experiment results to the topography of active strike-slip faults.

The experimental results indicate that the geometric patterns of the surface fractures resulting from active strike-slip movement are a significant factor in the long-term topographic development of peninsulas and island arcs. This mechanism can be explained by models with free and fixed boundary conditions. Analyses of historical records and traces of active faults reveal that present-day geological features are the result of the long-term (tens of thousands of years) accumulation of episodic, rapid changes associated with earthquake events (coseismic) and gradual changes that occur between events (interseismic). Thus, the 3*D* nature of strike-slip deformation should be considered in analyzing large-scale (10–100 km) geometric patterns in active strike-slip regimes within Japan.

Based on the theories of Riedel (1929), Skempton (1966), Tchalenko *et al.* (1970), Naylor et al. (1986), and other researchers, Cristallini *et al.* (2004) tried to explain the deformation expression on the surface or in some cases the 3D movement along strike-slip fault systems. However, the authors only examined the apparent movement, without giving definitive boundary conditions, either free or fixed, at the edge of the model. In nature, however, all the strike-slip faults have one of the two boundary conditions, and the fault borders must be defined. In this study, this study define the boundary conditions of the fault and discuss the difference between systems with various boundary conditions. Moreover, the horizontal movement, either extension or compression, in 2*D* modeling must affect the 3*D* model, *i.e.*, for horizontal extension, down-warping occurs, and vice versa. This must be expressed in the Quaternary topography on the strike-slip faults, because such instantaneous movement usually accumulates during the long history of repeated earthquake movement during the Quaternary, and must appear in the geometric models (Nakata *et al*., 1989). Therefore, in our study this study considered three elements: analog and numerical experiments, and application to the topography of the strike-slip fault systems.

2. Analog Experiments

2-1. Riedel Shear Theory

There are many types of Riedel shear box tests conducted in the horizontal slip model. For example, Naylor *et al.* (1986) showed many experiments of various initial stress states, and obtained basement movement and its effect of features or processes of Riedel shears. Bartlet *et al.* (1981) performed tri-axial experiments in limestone board sandwiched within sandstone, and obtained the common style of deformation as Riedel shears in the limestone.

Several types of Riedel shears have been recognized in natural fractures along active faults and in laboratory experiment results (Tchalenko *et al.* 1970). Since these early studies, many types of Riedel shear-box tests have been conducted using a horizontal slip model. For example, Naylor *et al.* (1986) showed the 3*D* relationship for the relative ages, dip, strike, and 3*D* shape of faults in basement-controlled wrench faulting. The geometries of the Riedel shears were established based on the results of numerous experiments conducted with varying initial stress states.

2-2. Methodology of the Analog Experiment

Many researchers have performed shear-box dislocation experiments. These tests represent the deformation of sedimentary cover rocks in response to dislocation in the underlying basement. The general situation in natural cases is already understood, as strike-slip faults are associated with subordinate faults or fractures oriented parallel or sub-parallel to the main fault.

In our experiments, this study used an elastic rubber sheet between the basements, as the modeled elastic transitional layer must be placed between the rigid basements and overlying plastic cover. The sheet mimics the deformation and dislocation in the basement and cover sediments (**Fig. 1**).

Compared with strike-slip movement along an active fault, analog experiments must be performed at a greatly reduced scale. In general, strike-slip movement generates flower structures in overlying sediment layers. Such movement occurs at depths of 3–30 km. Because analog experiments must be performed at a reduced scale, an elastic material should be selected to replicate the sediment layer. Hence, this study chose to use a rubber sheet in the present experiments (**Fig. 2**).

In our analog experiments, the basement rubber sheet is made of 3-mm-thick elastic rubber, and the 2-cm-thick covering layer is made of quartz powder with an average grain diameter of 8 μm. Using these materials, an echelon fold patterns develop in the basement rubber sheet (Takami, 2002, Ohsumi and Ogawa., 2002).

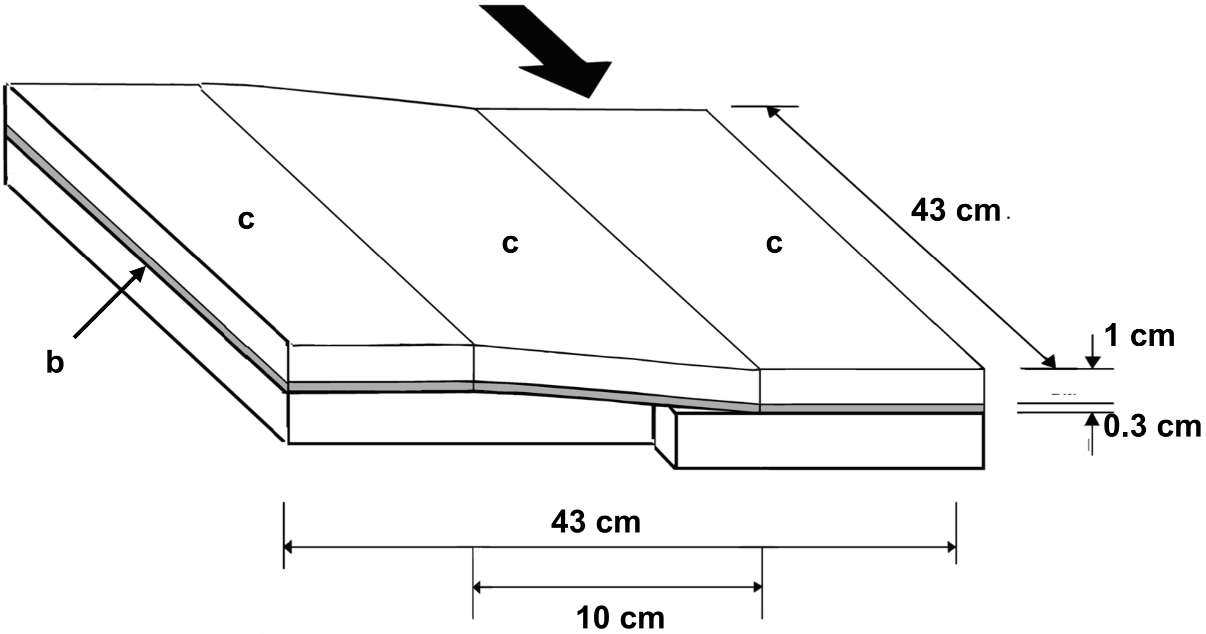

Fig. 1. Details of the Riedel shear-box test for the analog experiment. a. Wooden boards that serve as the basement. b. A rubber sheet is used as a cover over the dislocating board to ensure sufficient fractures between the board and the overlying powder. c. A layer of sedimentary quartz powder (1–4 cm thick) is placed on the rubber layer, and the surface of the sediment is bonded using glue.

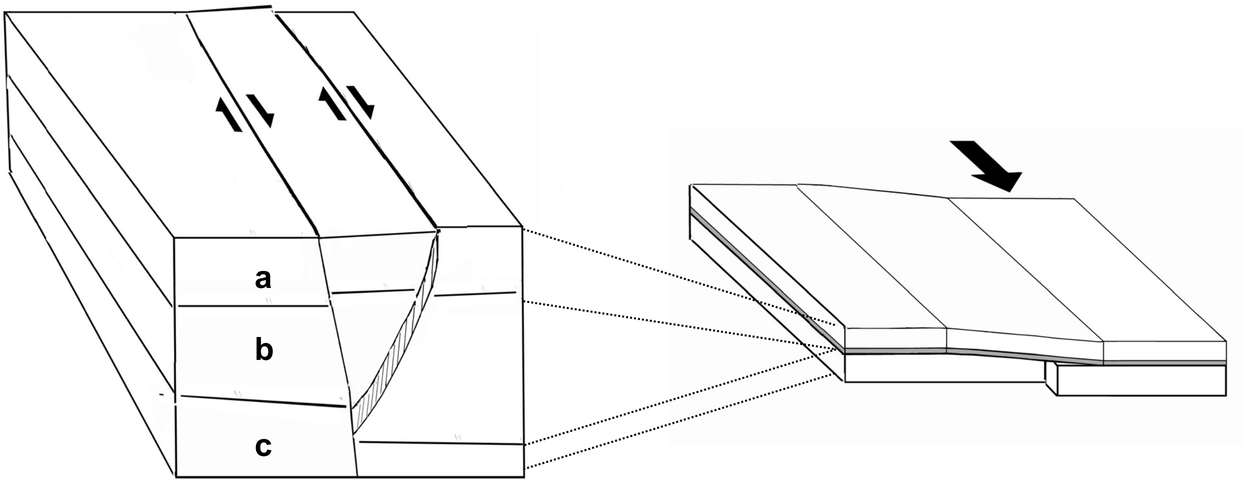

Fig.2. Schematic of tectonic formations relating to the analog experiment.

2-3. Results and Interpretation

Fracture process in the analog experiment

The fractures R_1 (R, synthetic Riedel shear) and R_2 (*R*', antithetic Riedel shear) developed in the basement layer and appear in the layer of powder above the elastic rubber (**Fig. 3**). Regions of horizontal extension and contraction developed in conjunction with the two types of fractures in the dislocated area. The diagonal portions of the defined *T*-planes developed at both ends of the extension region, followed by clockwise rotation of the fracture, as revealed by the displacement of the markers. In the central part, the fracture folded into a sigmoidal shape because of the clockwise rotation at the ends. In contrast, the fractures were rotated counterclockwise at the central parts.

The variation of the displacement modes between the ends and central parts of the fractures within the sedimentary cover layer (the quartz powder) explains the origin of crustal block rotation during displacement along strike-slip faults (**Fig. 3**). Clockwise rotation occurs in the case of strike-slip extension, when rotation occurs with dextral displacement. Anti-clockwise rotation of the blocks occurs during strike-slip contraction (Martel *et al.* 1988; the original report considers a left-lateral strike-slip fault regime).

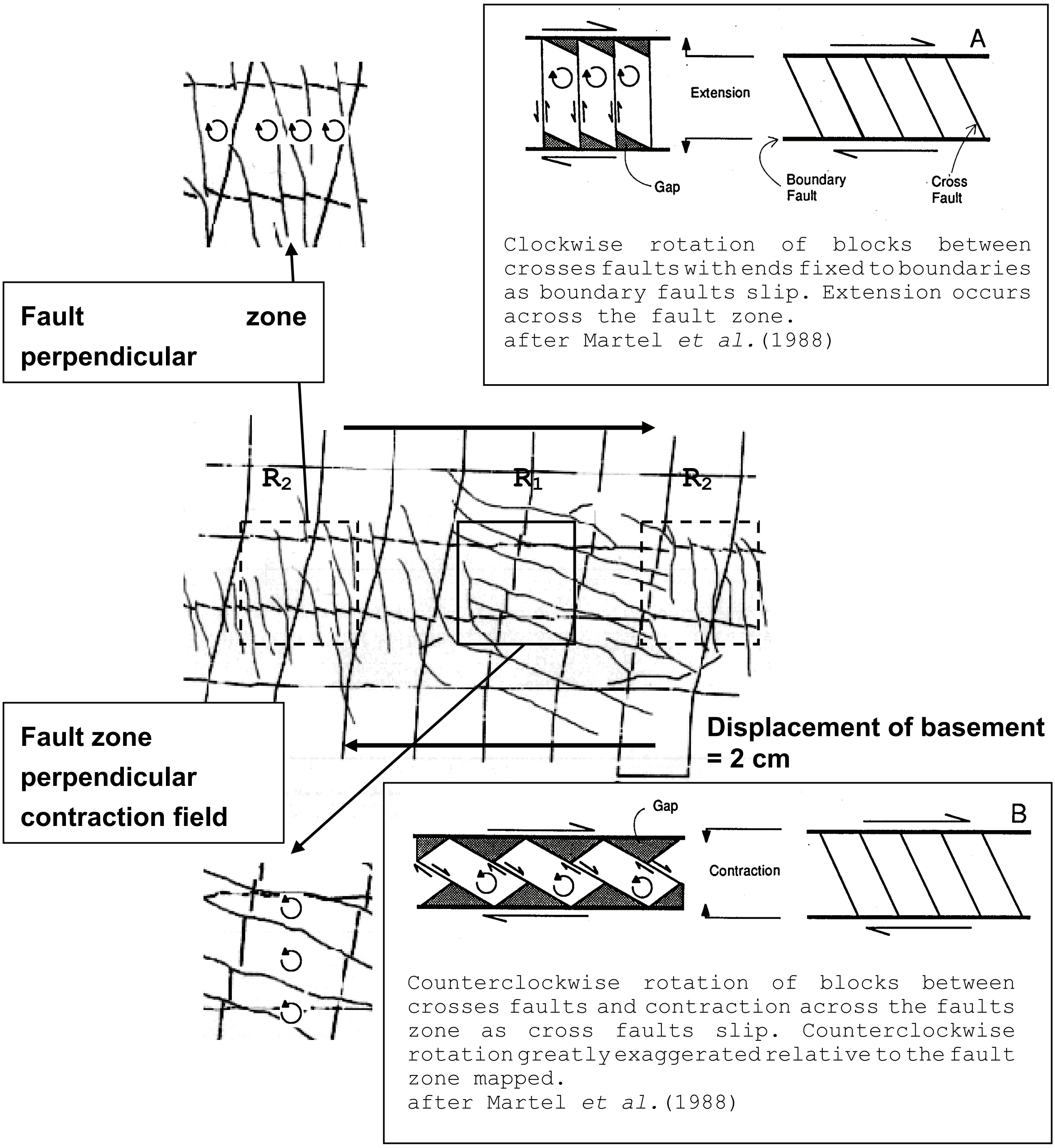

Clockwise rotation of blocks between crosses faults with ends fixed to boundaries as boundary faults slip. Extension occurs across the fault zone.
after Martel *et al.* (1988)

Counterclockwise rotation of blocks between crosses faults and contraction across the faults zone as cross faults slip. Counterclockwise rotation greatly exaggerated relative to the fault zone mapped.
after Martel *et al.* (1988)

Fig.3. Fractures are generated in a strike-slip fault. At both ends of the fault, the fracture shape is controlled by clockwise rotation. Within the central part of the fault, the fracture shape is controlled by counterclockwise rotation (compare the different movement directions of the markers).

3. FEM Analyses

3-1. Analytical Method

This study used dynamic, nonlinear FEM analysis to generate stress/strain patterns for a simple-shear field. TDAP III software was used for 3*D* modeling, employing three different boundary conditions. Because this model considers vertical component deformation for a single unit depth, the experiment represents a 3*D* analysis (**Fig. 4**). That is, areas of horizontal extension coincide with subsidence, whereas areas of horizontal contraction represent uplift.

In this model, a rubber sheet and quartz powder are used to represent the lower and upper layers, respectively, on top of the fault-displaced basement. In terms of the physical properties of the two layers, the rubber sheet corresponds to an elastically linear material and the quartz powder to a nonlinear, brittle material (**Fig. 4**). The linear material properties for the rubber were taken from PWRI (1998) as follows: shearing stiffness modulus G = 80 MPa; Poisson ratio $\mu = 0.4$; density $\rho = 5.9$ kN/m^3; and damping factor h = 0.1. The nonlinear material properties for the quartz powder were taken from Mitchell (1993) as follows: shear modulus G = 3 MPa; Poisson ratio $\mu = 0.4$; density $\rho = 16.7$ kN/m^3; damping factor h = 0.025; cohesion C = 0; and friction angle $\varphi = 26$ degree. In this type of analysis, the important area is the central part of the upper layer (Dresen, 1991).

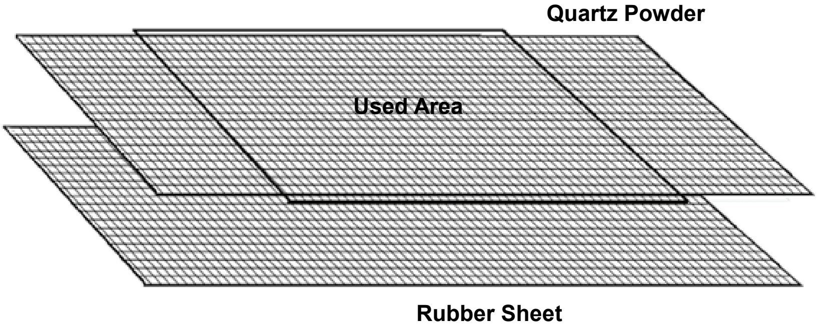

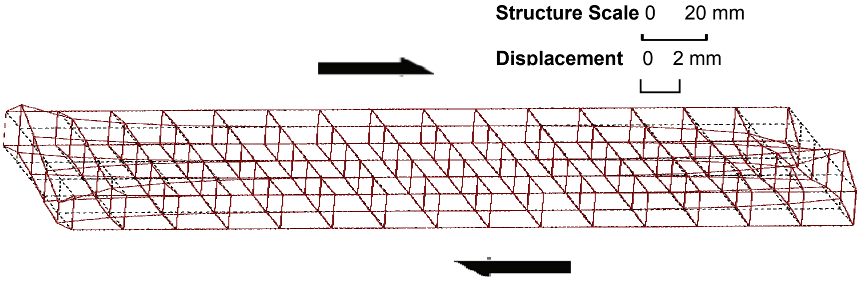

Fig.4. The experiment comprises two layers: a rubber sheet and quartz powder. The area of interest is the middle section of the upper layer. Lower figure is the bird's-eye view of rubber sheet's displacement by right-lateral strike-slip (Case1). Vertical displacement occurred at contraction area.

3-2. Experimental Cases

This study considered three experimental types of strike-slip fault: Case 1 – both ends are free (**Fig. 5**); Case 2 – both ends are fixed (**Fig. 6**); and Case 3 – one end is free and the other fixed (**Fig. 7**).

Case 1: Free model

In this case, both ends of the fault are free, corresponding to the analog experiment described above. In terms of displacement, the stress distribution at the ends of the fault is different from that at the center (**Fig. 8**). This model produces extensional fields in the top-right and bottom-left sections of the block (as viewed in the figure), while contractional fields occur in the central area, top-left, and bottom-right.

Case 2: Fixed-end model

In this case, both ends of the fault are fixed. This mimics the deformation of a typical dextral fault, in which both ends are stationary and do not dislocate (**Fig. 9**). This model has extensional fracture fields at the bottom-right and top-left sections of the modeled area, and radiation patterns appear at the center top-right and bottom-left areas.

Case 3: One-end-fixed model

In this case, one end of the dislocated basement is fixed and the other is free (**Fig. 10)**. The free-end area shows similar behavior to that observed in Case 1, while the fixed-end area shows behavior similar to that observed in Case 2.

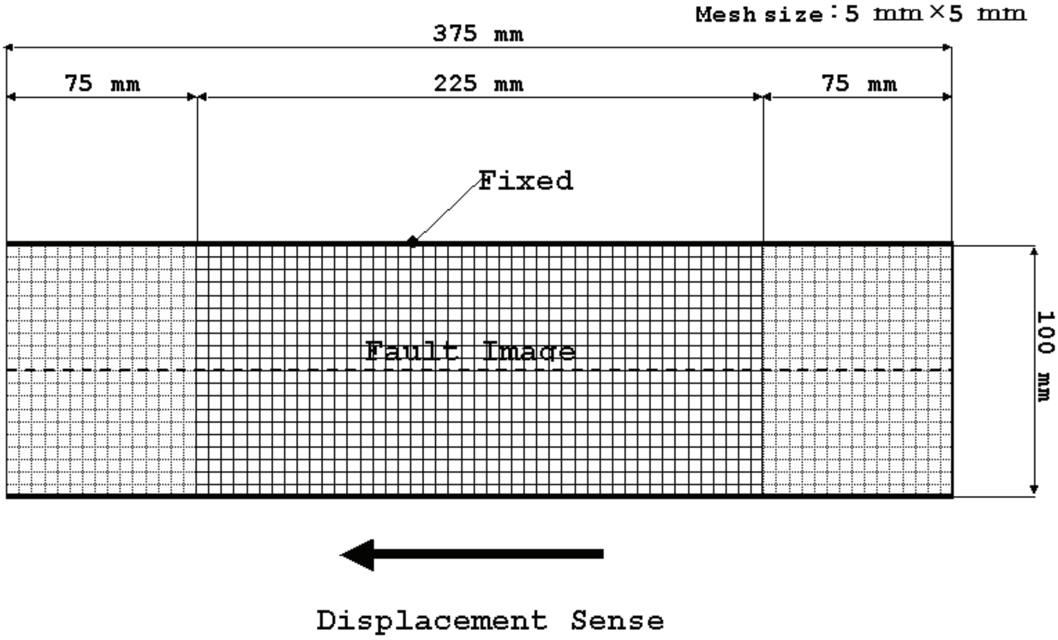

Fig.5. Free model (Case 1).

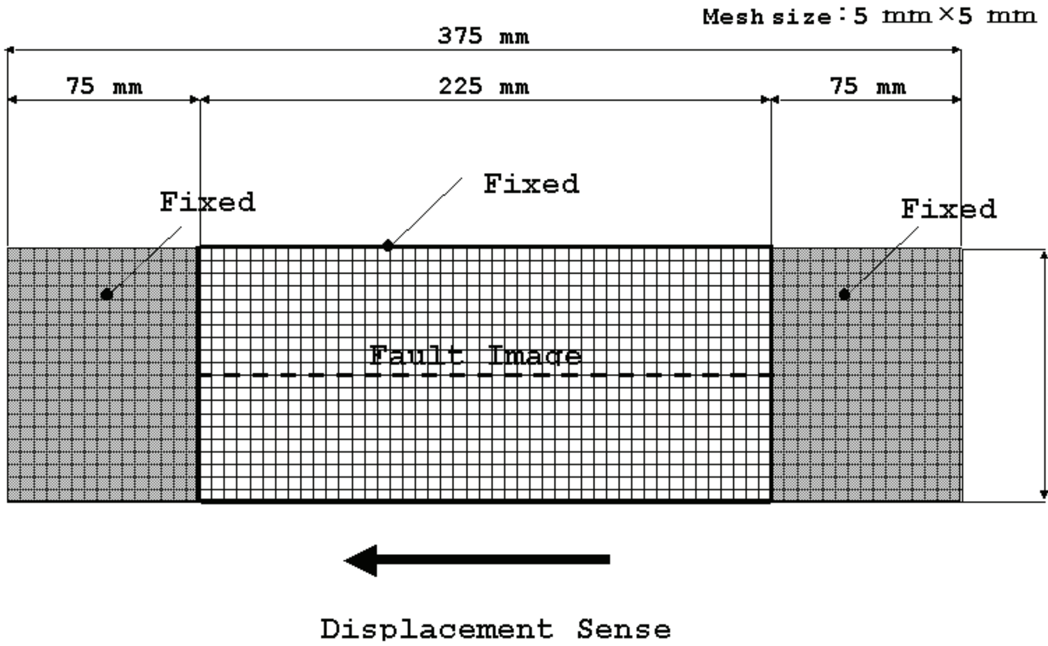

Fig.6. Fixed-end model (Case 2).

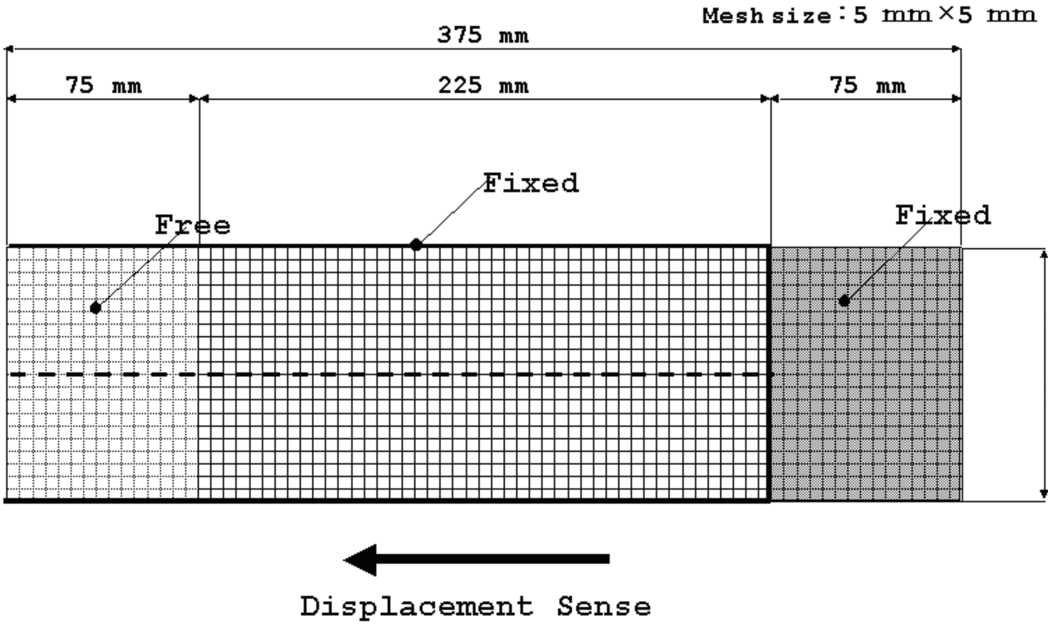

Fig.7. One-end-fixed model (Case 3).

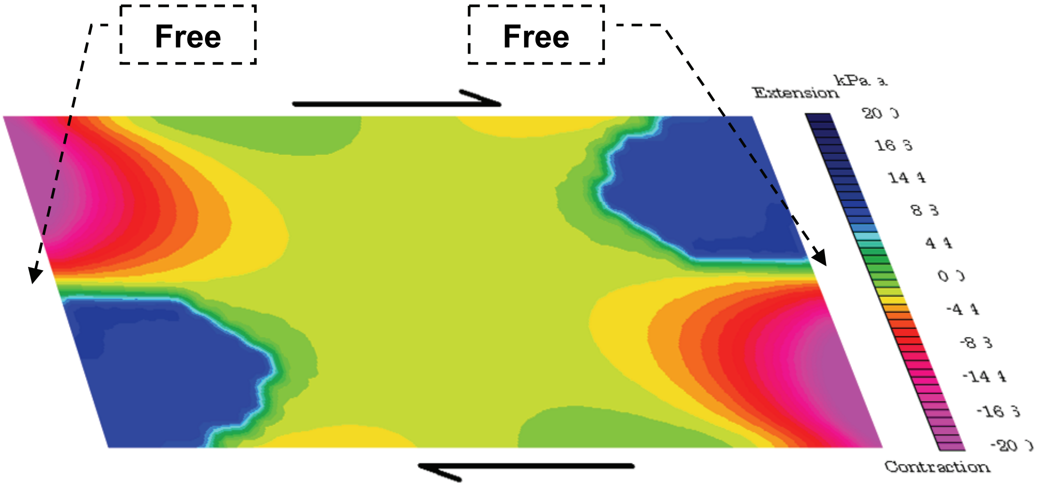

Fig.8. Model results showing the extension field (cool colors) and contraction field (warm colors) at each end of the free model (Case 1).

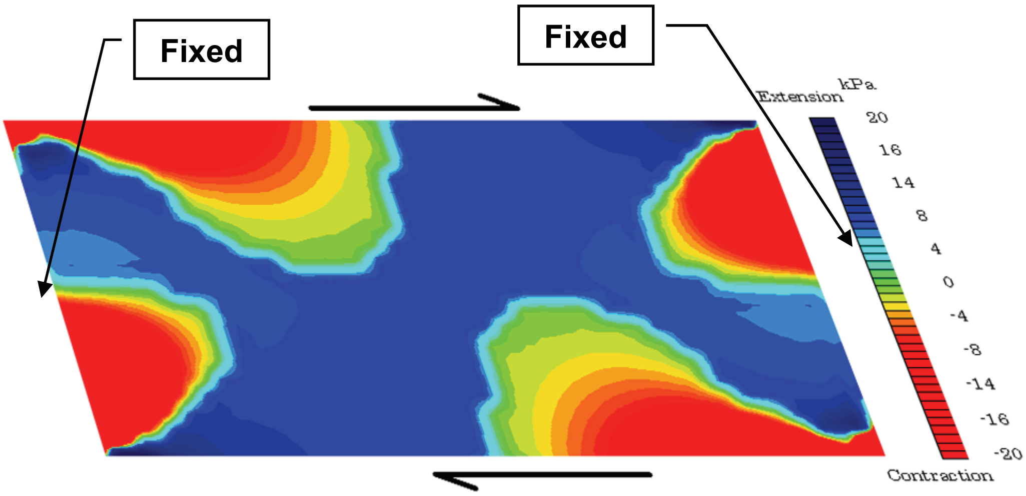

Fig.9. Model results showing the extension field (cool colors) and contraction field (warm colors) at each end of the fixed model (Case 2).

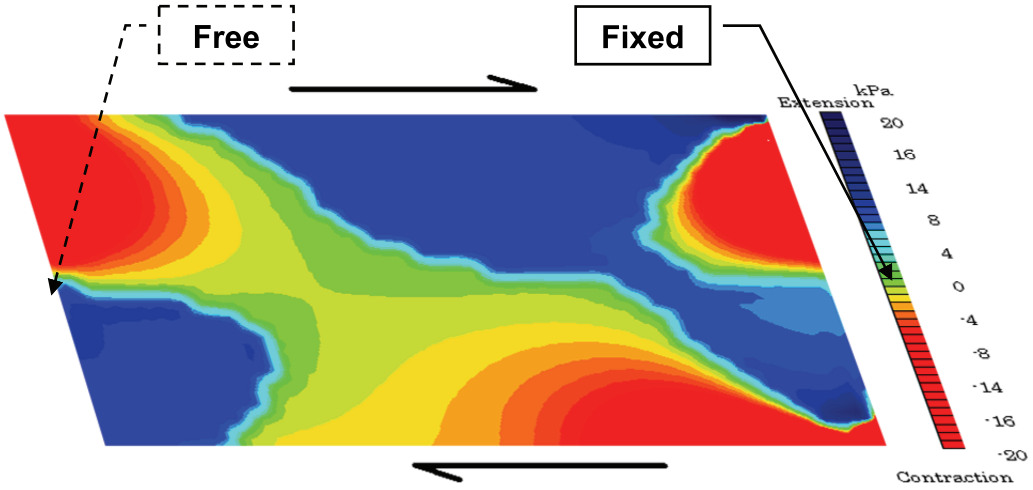

Fig.10. Model results showing the extension field (cool colors) at the free end and the contraction field (warm colors) at the fixed end of the one-sided model (Case 3).

4. Discussion

Analog Experiments

The analog experiment chose to use a rubber sheet, which was the elastic material should be selected to replicate the sediment layer in the experiments. At both ends of the shear box, clockwise rotation of blocks are generated, indicated by the discontinuous displacement of the markers. In a strike-slip fault, fractures are generated in the region under tension of dilatation. The fractures $R1$ and $R2$ developed in the basement layer and appeared in the layer of powder above the elastic rubber sheets. In the central part of the layer the fracture folded into a sigmoidal shape because of the clockwise rotation at the ends. In contrast, the fractures were rotated counterclockwise at the central parts. Clockwise rotation occurs in the case of strike-slip extension, when rotation occurs with dextral displacement. Anti-clockwise rotation of the blocks occurs during strike-slip contraction.

Numerical Experiments

The model in which both ends are free indicated the development of extensional basins or sag ponds along the strike-slip fault. Woodcook *et al.* (1986) suggested that extensional fields are susceptible to subsidence, while contraction fields are susceptible to upheaval (**Fig. 11**). This result explains the typical dextral fault as a pull-apart basin (*e.g.*, the Mineoka Tectonic Belt in the Boso Peninsula, Japan).

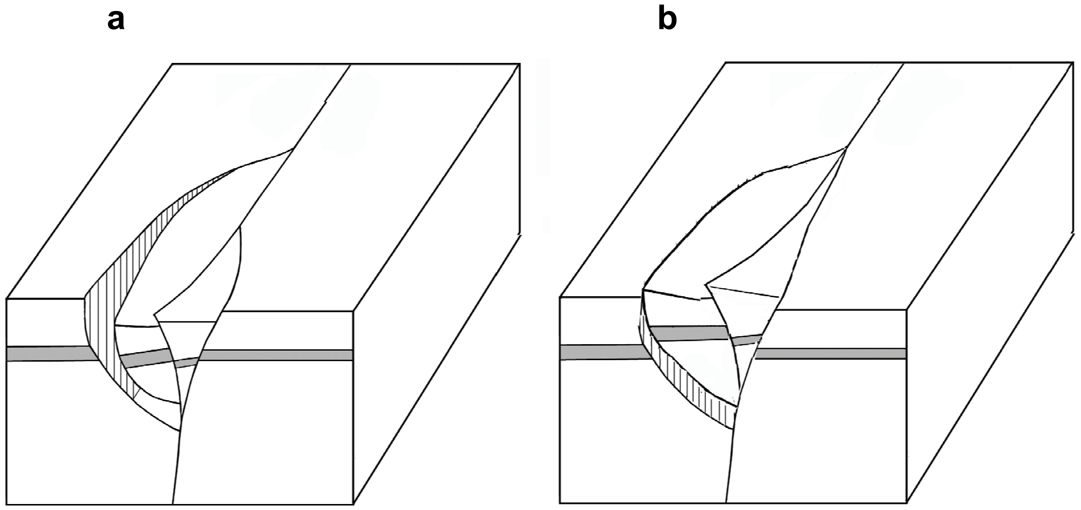

Fig.11. Postulated three-dimensional forms of (a) an extensional duplex (showing a negative flower structure; a pull-apart basin) and (b) a contractional duplex (showing a positive flower structure) in the strike-slip model (Woodcock *et al.,* 1986).

The free boundary model

The results of our analog and numerical experiments have implications for our understanding of natural examples of strike-slip faults.

The fault pattern observed in forearc areas in Japan, where many active faults cut across peninsulas, may correspond to the experimental results obtained in this case, as the free ends permit deformation of the land surface. For example, the Mineoka Tectonic Belt on the Boso Peninsula (**Fig. 12**), Central Japan (*e.g.,* Ogawa *et al.* 1988, 1989) creates a sharp knife-edge fault as observed from aerial photographs. The nearby sea area is ca. 3,000 m deep, and strike-slip displacements are found on the seafloor part of the Mineoka Tectonic Belt (**Fig. 13**). Here, part of the long fault was naturally destroyed, corresponding to experimental Case 1.

The fixed-end model

This phenomenon is observed in the deformation of typical dextral faults. The displacement along the central part of the fault can be explained by the double-couple stress state in the strike-slip model (Maruyama 1963; Aki and Richards 2002) (**Fig. 14**). Nakata and Goto (1998) tested these criteria on several recent surface ruptures and active faults, and applied them to the segmentation of the active fault system of the Median Tectonic Line (MTL) in Shikoku, Southwest Japan. The authors' investigation of recent seismogenic fault ruptures revealed an interdependent relationship between the pattern of surface ruptures and their propagation directions (**Fig. 15**). The authors found that the horizontal displacement has reversed borders along the central part of the fault line, resembling a hinge pattern.

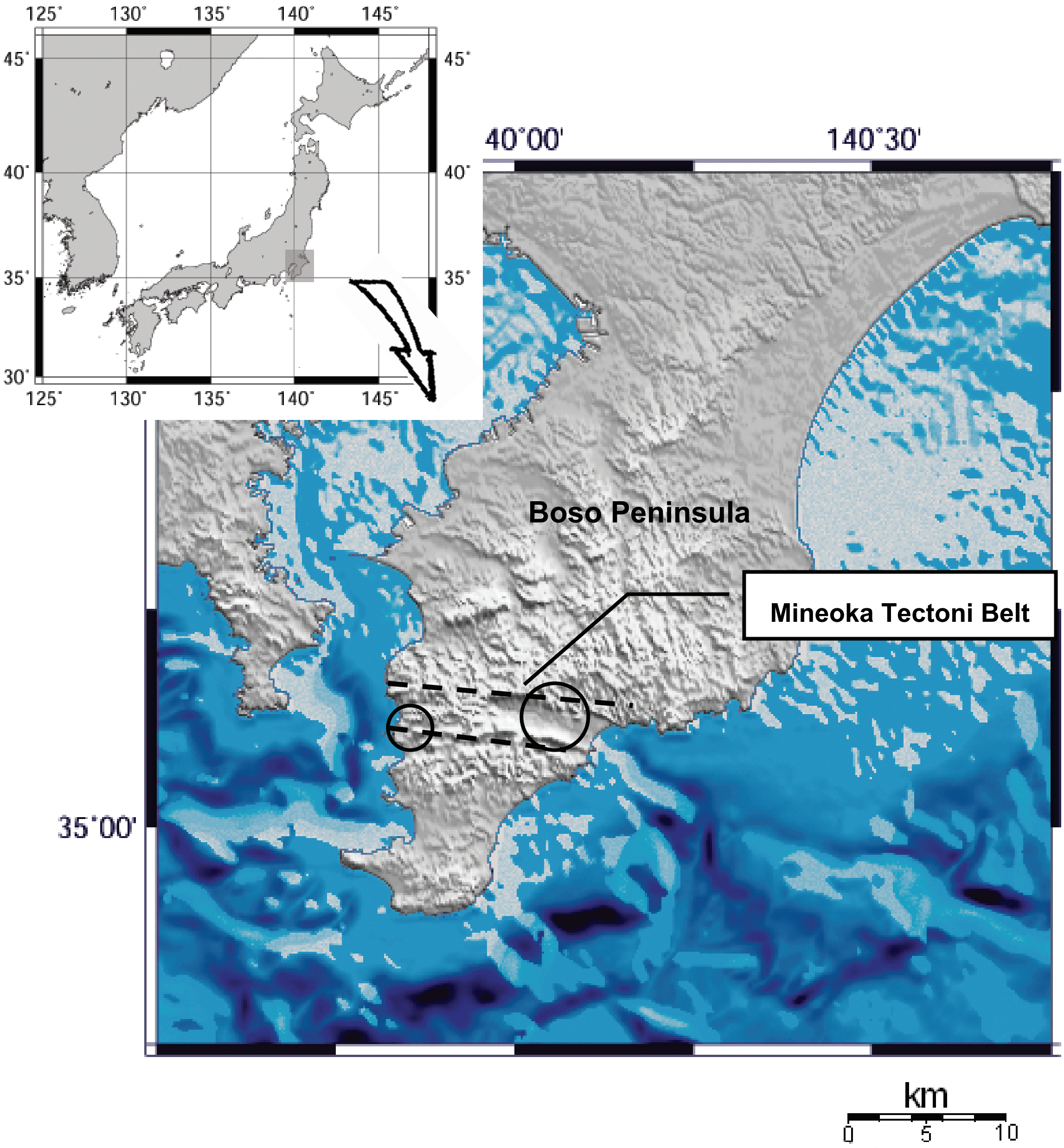

Fig.12. Numerical elevation map (50 m grid) of the Boso Peninsula (Geographical Survey Institute of Japan 2005). The marine data source is JTOPO30, as compiled by the Marine Information Research Center, Japan, using a multi-beam survey and post-processing. Dashed lines mark the zone of the Mineoka Tectonic Belt. Areas of subsidence are indicated by circles.

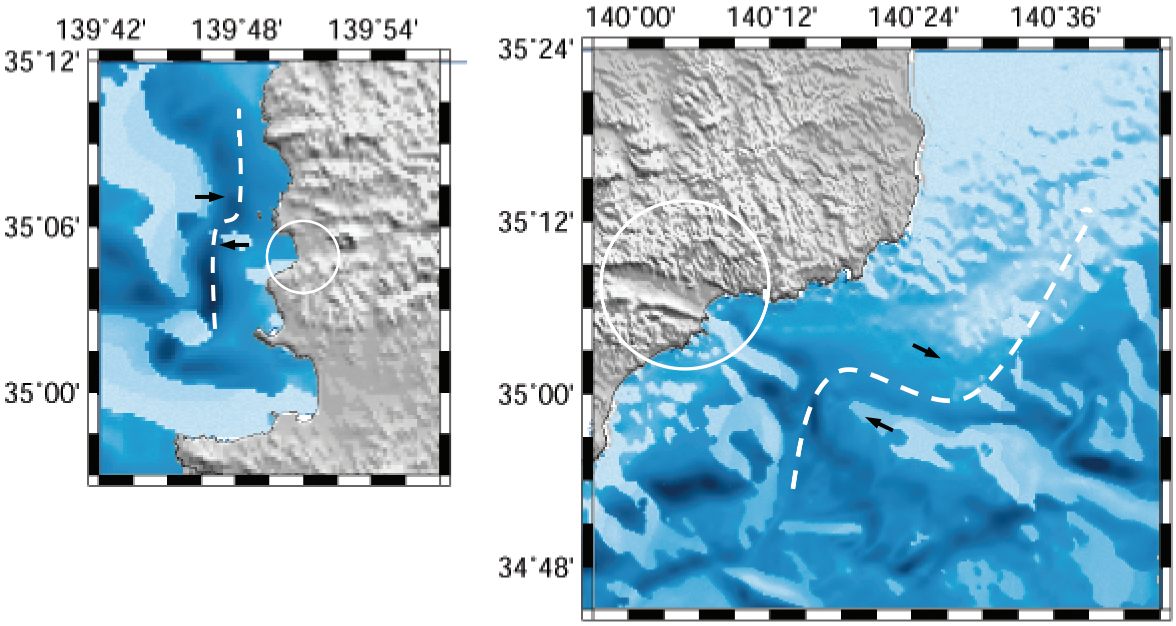

Fig.13. Strike-slip gaps on the seafloor on both sides of the Mineoka Tectonic Belt. The nearby sea area is ca. 3,000 m deep and the strike-slip gaps are found on the seafloor in areas of extension along the Mineoka Tectonic Belt.

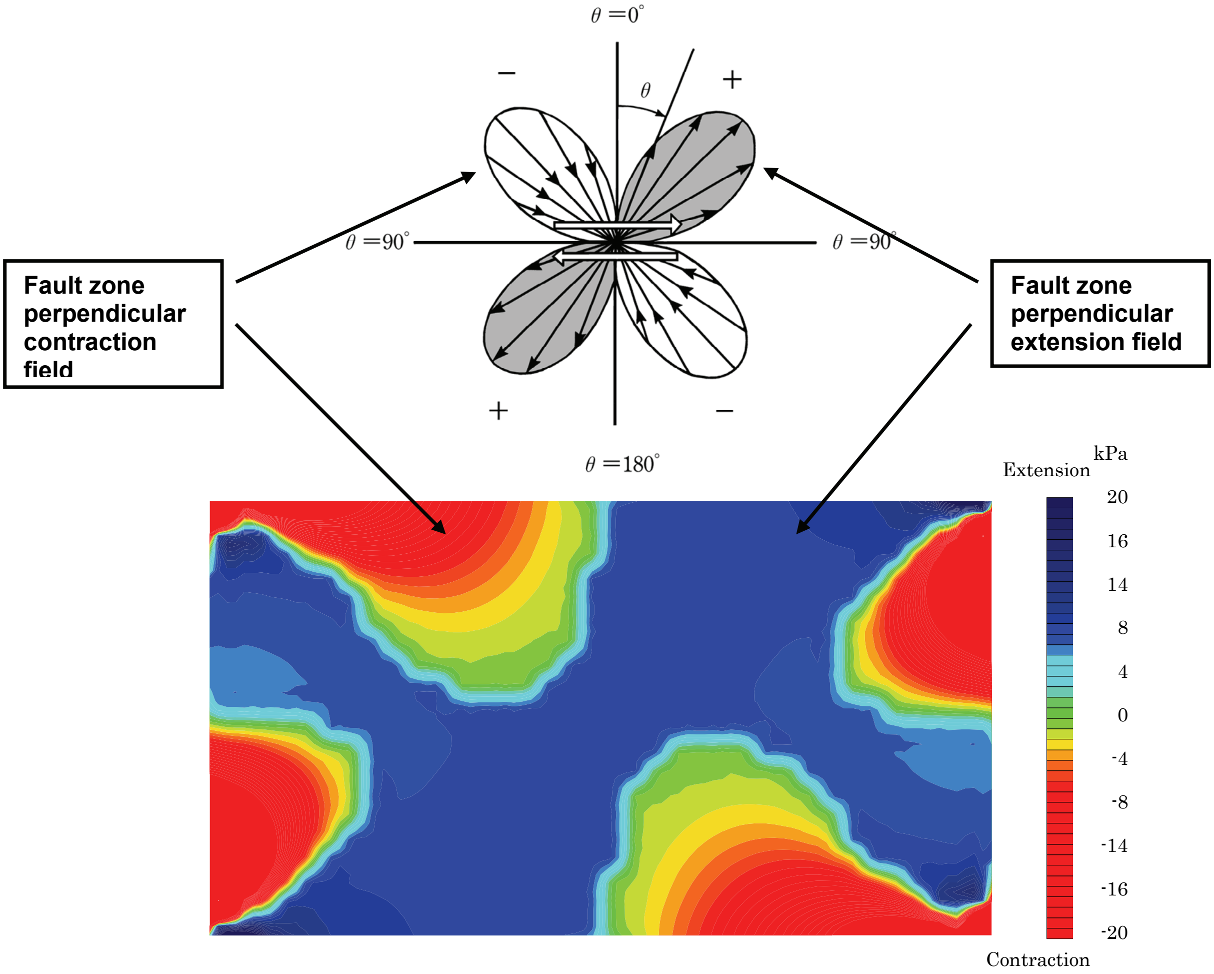

Fig.14. The central part of the modeled stress field can explain the double-couple stress state in the strike-slip model (Maruyama 1963; Aki and Richards 2002).

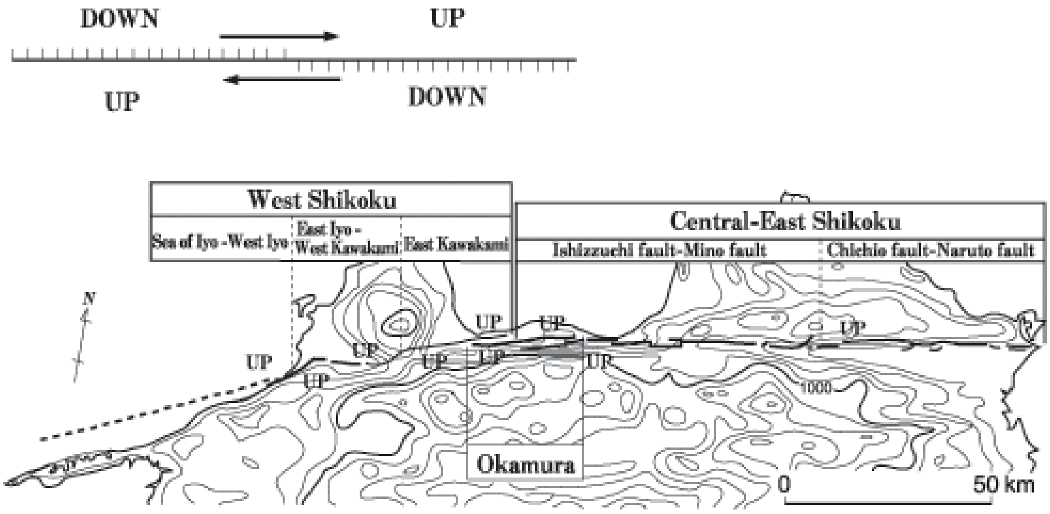

Fig.15. New segmentation model for the active fault system of the Median Tectonic Line in Shikoku (Nakata and Goto 1998). 1. Known fault traces 2. Newly identified fault traces relative to the upper side along the active faults.

Acknowledgments

This study thank Mr. Y. Takami for permission to use the sketch of the fractures shown in **Fig. 3**.

Chapter 3

Strong Motion Evaluation for the AD 365 Crete Earthquake

1. Introduction

West Asia is an area of active crustal deformation and has a history of large magnitude earthquakes. Because crustal movement continues today, scientific investigation of seismicity in this region may contribute to understanding and protecting against earthquake and tsunami disasters.

According to Hori and Kaneda (2013), the relative plate motion of tectonics from the area around Mediterranean Sea and west to India is 2~4 cm/ year. This movement is smaller compared to other convergent plate boundaries that are similar to the collision zone in the Himalayas–Tibet mountain belt. However, they are characterized by a subduction zone (solid line in the **Fig.1**) and a predominance of strike-slip fault such as the north Anatolia dislocation. In these subduction zones there are large earthquakes and tsunamis. These areas caused tsunami damage in the Marmara Sea along the north Anatolia fault in the past.

In West Asia, the African plate is subducting beneath the Anatolian plate at a rate of 1 to 3.5 cm/yr., large magnitude earthquakes frequently occur in this subduction zone. In AD 365 (**Fig.2**), a large magnitude (M8.5) earthquake occurred near Crete (*e.g.,* Fischer (2007), Shaw *et al.* (2008), Stiros (2010), Papadimitriou and Karakostas (2008)). The AD 365 earthquake, one of the best known ancient earthquakes in the eastern Mediterranean, caused a tsunami that resulted in great damage to Syria, northern Egypt and the Greek coast.

According to Pirazzoli (1986), who investigated the upheaval of the coastline of the eastern Mediterranean, the period between 350 and 550 was the most seismically active period in the past 2,000 years.

Crete, located 160 km south of the Greek mainland, is the largest (area of 8,336 km^2) among approximately 3,000 Islands in the Aegean. Ancient earthquakes in Crete have been reported in various books by Ambraseys (*e.g.*, 1994). In the 4th century, Ammiaus, a historian and military service member, wrote history books consisting of 31 volumes. Due to the Christian propagation, which began in the age of the Roman Empire, many historical records were made in the 4th–5th centuries.

The tsunami caused by the AD 365 earthquake resulted in more damage in the Peloponnese peninsula than resulted from the earthquake itself. Because the magnitude was higher than M8, tremor propagated across a large area surrounding the Mediterranean. Smaller magnitude earthquakes that recently occurred in the Greek Islands also affected a wide area around the Mediterranean. John Cassian, a theologian in the 4th–5th century, and Sozomenes, a Byzantine historian in the 5th century, described evidence of widespread flooding from the tsunami by tracing damage on the roofs of buildings, and subsequent retreat of the coastline. A Byzantine historian, George the Monk, mentioned the tsunami in a 9th century chronicle. The tsunami caused by the AD 365 earthquake was also chronicled by Theopanos in the 8th–9th centuries, Cedrenus in the 11th century, and Glycas in the 12th century. According to the literature, the tsunami destroyed 50,000 houses and had 5,000 casualties in Alexandria, Egypt.

Because large magnitude earthquakes and associated disasters could occur again in the future, this study investigates and describes the characteristics of the AD 365 Crete earthquake.

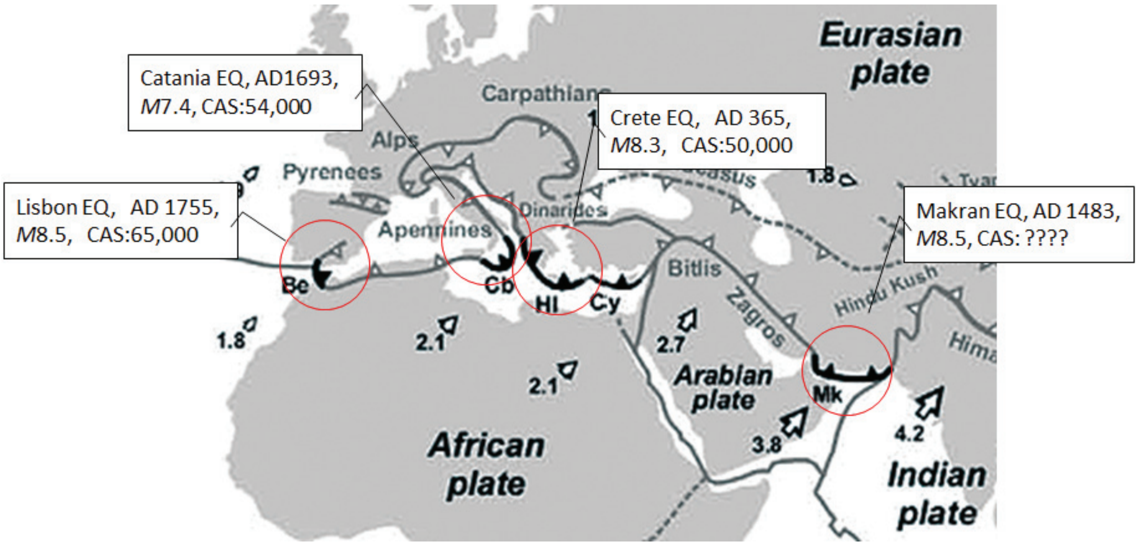

Fig.1. Tectonics from the area around Mediterranean Sea and that west to India (modified from Schellart and Rawlinson, 2010). Some subduction zones in Mediterranean (Be: Betic—Rif, Cb: Calabria, Hl:Hellenic, Mk: Makran) and North Anatolian fault in Turkey are mentioned. (Hori, T. and Kaneda, Y., 2013).

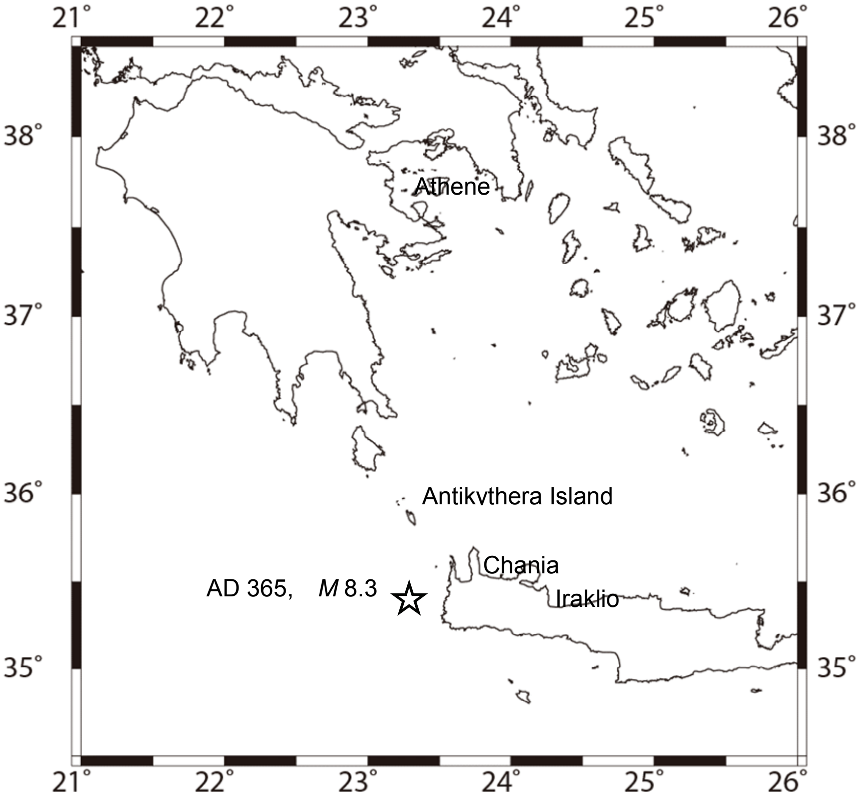

Fig.2. Epicentre of The AD 365 Crete Earthquake.

2. Crustal movements

Flemming (1978) evaluated land subsidence and upheaval and estimated the relative rate of annual sea level rise (1.05 mm/yr) based on research on the south-west coast of Turkey and at about 175 points in Cyprus. Change in the sea surface in western Crete under the condition of a continuous sea-level rise and intermittent land uplift is shown in **Fig. 3.**

Pirazzoli (1996) suggests that there is a trace of upheaval along the Greek coast from an earthquake that occurred between the mid-4th and mid-6th centuries in the Early Byzantine tectonic paroxysm (EBTP) turbulent period. Pirazzoli *et al*. revised his previous interpretation (1982, 1986) after his detailed survey and radiocarbon dating of the samples obtained from Antikyhira Island. Significant co-seismic uplift that took place during a short period was demonstrated by over 30 radiocarbon dates from 12 regions in Greece and by very precise sea-level indicators in the eastern Mediterranean. Therefore, it is assumed that the scale of uplift in Crete was 0.5 to 1.0 m in general but gradually increased towards the south-west and reached approximately 9 m. Radiocarbon dates show that the largest change occurred between 261 and 425.

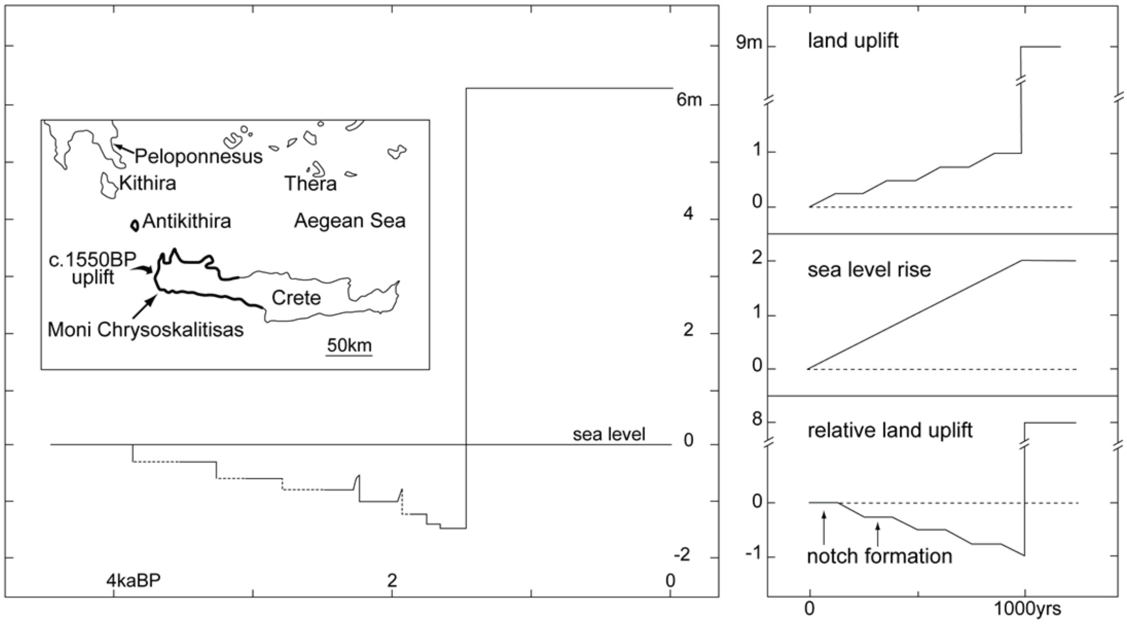

Fig. 3. Left: Upheaval history of the oldest (lowermost) layer, assuming a fixed sea-level based on the data by Thommeret *et al.* (1981) and Pirazzoli *et al.* (1982). Right: A scenario explaining the change in the relative sea level in west Crete based on the hypothesis of constant rise of the sea level and intermittent rise of the land. （*after* Stiros, 1996）

3. Data and Method

3-1. Observed Record of Small Earthquake

This study used some observed records of small earthquakes located near the hypocentre of the AD365 Crete Earthquake. These data are used to calculate stochastic Green's functions. The stochastic Green's function uses random phases or realistic phases. This study used realistic phases scrutinized from earthquake records. Earthquake records of the Crete Island, Mw6.4, 12 Oct. 2013, provided these phases for the stochastic Green's function. The dislocation model is based on Papadimitriou and Karakostas (2008). Some of these velocity records were saturated (off-scale) at Antikythera, Chana and Iraklio (**Fig.4 upper graph**). Considering the scaling relationship, M_w 6.4 is a better selection as a small event. This study also consider records from a smaller magnitude event. Thus, this study selected the screening data for aftershock records (M_w 4.0, 12 Oct. 2013: **Fig.4 lower graph**) at Antikythera, Chana, Aptera and Iraklio. At Phalasarna, there is no recording/ observation point. Thus, the Aptra record is used for the estimation at Phalasarna. At Athens, the aftershock record included noise, this study used main shock phase at this point.

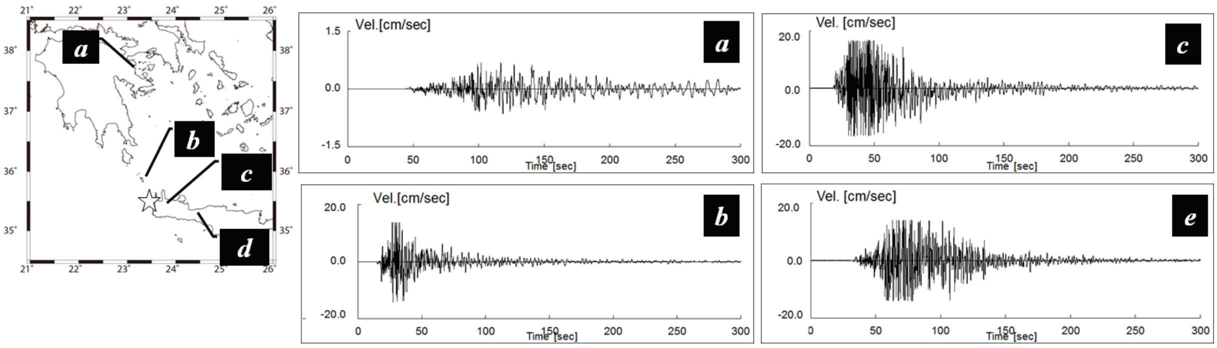

Main shock records of the Crete Island, *Mw*6.4, 12, Oct. 2013.

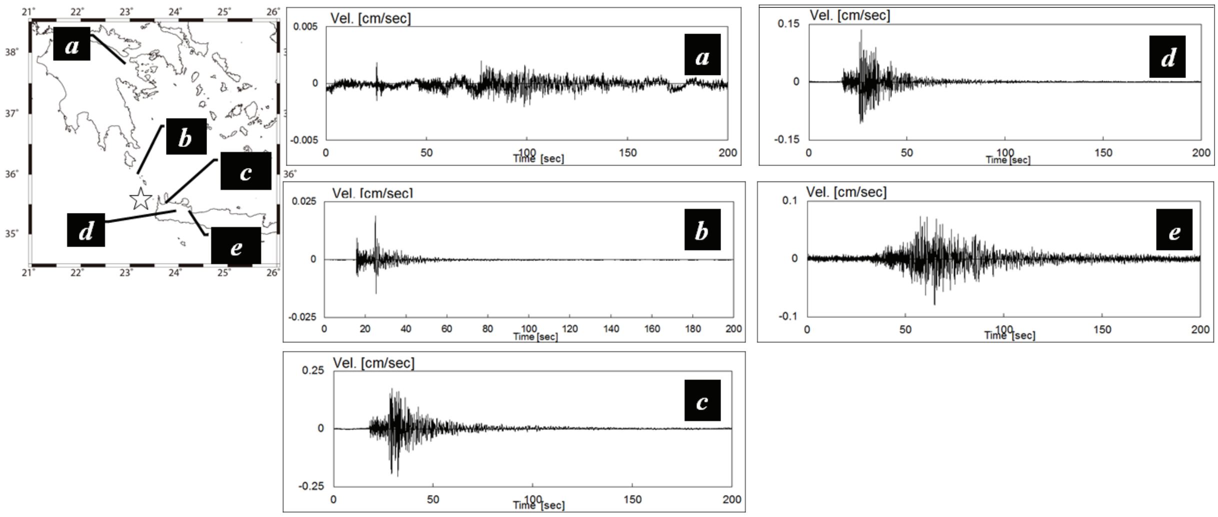

Aftershock records of the Crete Island, *Mw*4, 12, Oct. 2013.

Fig.4. Earthquake records of the Crete Island, 12, Oct. 2013.

3-2. Estimation of the Earthquake Ground Motions

This study estimated the earthquake ground motions by the stochastic Green's function method. **Table 1** shows parameters determined by several research groups. Fischer (2007) set the dip as 13 degrees and a low angle along the subducting plate, and set the slip to 42 m. Shaw *et al.* (2008), Stiros (2010) and Papadimitriou and Karakostas (2008) suggested parameters set that the shallow branch of the subduction zone dips at low angle and couples with the Aegean lithosphere, while the deep branch dips freely (without coupling) at a high angle beneath the south Aegean trough. Stiros (2010) conducted an elastic inversion analysis of the coastal upheaval and suggested that this earthquake had a minimum magnitude of 8.5 and was due to the reverse fault located offshore of south-western Crete. Shaw *et al.* (2008) proposed a fault model that accounted for upheaval on the Crete Island. Based on an investigation of the strike of the Aegean arc and the depth of hypocenters for small earthquakes, Stiros (2010) suggests that the depth of the fault is shallower than 70 km.

Table 1 Parameters setting

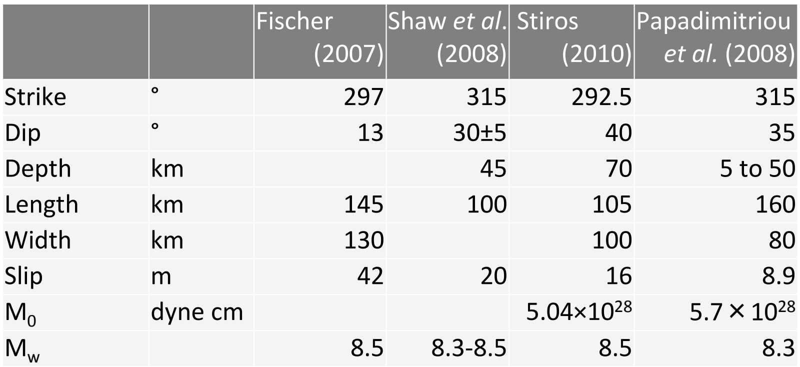

		Fischer (2007)	Shaw *et al.* (2008)	Stiros (2010)	Papadimitriou *et al.* (2008)
Strike	°	297	315	292.5	315
Dip	°	13	30±5	40	35
Depth	km		45	70	5 to 50
Length	km	145	100	105	160
Width	km	130		100	80
Slip	m	42	20	16	8.9
M_0	dyne cm			5.04×10^{28}	5.7×10^{28}
M_w		8.5	8.3-8.5	8.5	8.3

3-3. Parameter Setting

Pirazzoli (1996) suggested that there is a trace of upheaval along the Crete coast from radiocarbon dating and detailed survey with evidence of Holocene coseismic **(Fig.5**). By using this data, comparison of uplift distribution performed with these parameters.

Since Fischer (2007) had set dip angle at 13 degrees and a low angle along a subduction plate, and set slip distance to 42 m. According Murotani *et al.* (2013), the average slip distance was around 10 m during the Chili earthquake, 1960 and the Tohoku earthquake, 2011. 42 m was 4 times value of the Chili earthquake, 1960 and the Tohoku earthquake, 2011. Moreover, there is not sufficient value of upheaval distribution using the calculation formula of Okada (1992) (**Fig.6 *a***).

Shaw *et al.* (2008) shows the seismicity and topography in the area of Crete with the seismicity of the region corresponding to the AD 365 earthquake. According Shaw *et al.* (2008), the distribution of upheaval suggested that the AD365 Crete earthquake occurred not on the subduction interface beneath Crete, but on a fault dipping at about 30° within the overriding plate. The shallow branch of the subduction zone dips at low angle to and couples with the Aegean lithosphere, while the deep branch dips freely (without coupling) at a high angle beneath the south Aegean trough. This study applied the crustal upheaval modeling study by Shaw *et al.* (2008) using the calculation formula of Okada (1992) (**Fig.6 *b***).

Shaw *et al.* (2008) had set the dip angle at 30 degrees and a high angle within the overriding plate; the strike was set at 315 degrees, slip distance at 20 m and fault depth at 45 km. The strike angle of 315 degrees was the same as that of Papadimitriou and Karakostas (2008). Stiros (2010) had set dip angle as 40 degrees and a high angle within overriding plate; the strike angle was set at 292.5 degrees and slip distance to 16 m. Stiros (2010) showed that elastic dislocation analysis of coastal upheaval data reveals that this earthquake was associated with a reverse fault offshore of southwestern Crete, that its minimum magnitude was 8.5. This model was consistent with the approximate seabed trace of the fault, which observed and calculated displacements due to the modelled fault, and fault depth was a deeply as 70 km. This study applied the crustal upheaval by Stiros (2010) modeling study using the calculation formula of Okada (1992) (**Fig.6 *c***).

Papadimitriou and Karakostas (2008) set a direction of 315 based on seismology and topography of Papazachos (2000, 2001). The earthquake seismic moment was assumed as 5.7×10^{28} dyne·cm considering the area of the dislocation and an elastic coefficient.

According to Papadimitriou and Karakostas (2008), seismic coupling has been correlated with the maximum size of earthquakes that occur at a subduction zone. Subduction zones that are strongly coupled seismically periodically produce great earthquakes (Mw > 8.0) (Kanamori 1977), while those that are seismically uncoupled produce only moderate to large earthquakes (Mw < 8.0) (Ruff and Kanamori 1980). Reverse faulting is observed on planes with a NW or NE strike, and with approximately E-W P axis, the larger of them occurring in 1982 beneath the Mediterranean ridge. The slip distribution by Papadimitriou *et al.* (2008) had non-uniform distribution in the fault plane (**Fig.7**). This study was in the upheaval by using each of the 128 mesh division to give her the slip distance. In addition, the geometry of the fault was almost same as Shaw *et al.* (2008)'s setting, except the fault length was set at 160 km. Shaw *et al.* (2008) 's fault length at 100 km square, Mw scale become 8.0 class by using a scaling low formulae of earthquake size and fault area (*e.g. R.* Sato: $\log S = M$-4.07). *M*8 level is difference from 8.3 to 8.5 class, which each researcher defined. Thus, ground motion estimation by the stochastic Green's function method using the parameters of Papadimitriou and Karakostas (2008).

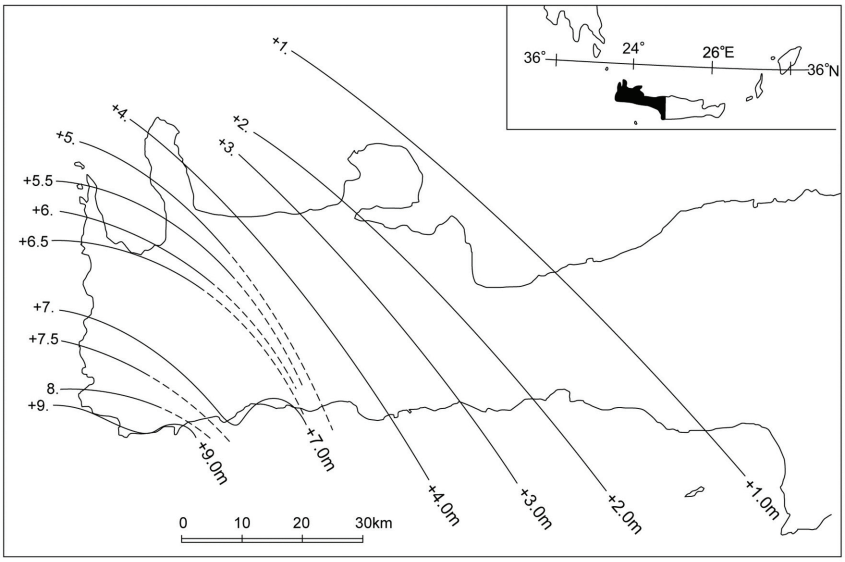

Fig.5. Contour of upheaval Crete (up to 9 m of the island southwest) modified from Pirazzoli *et al.* (1996)

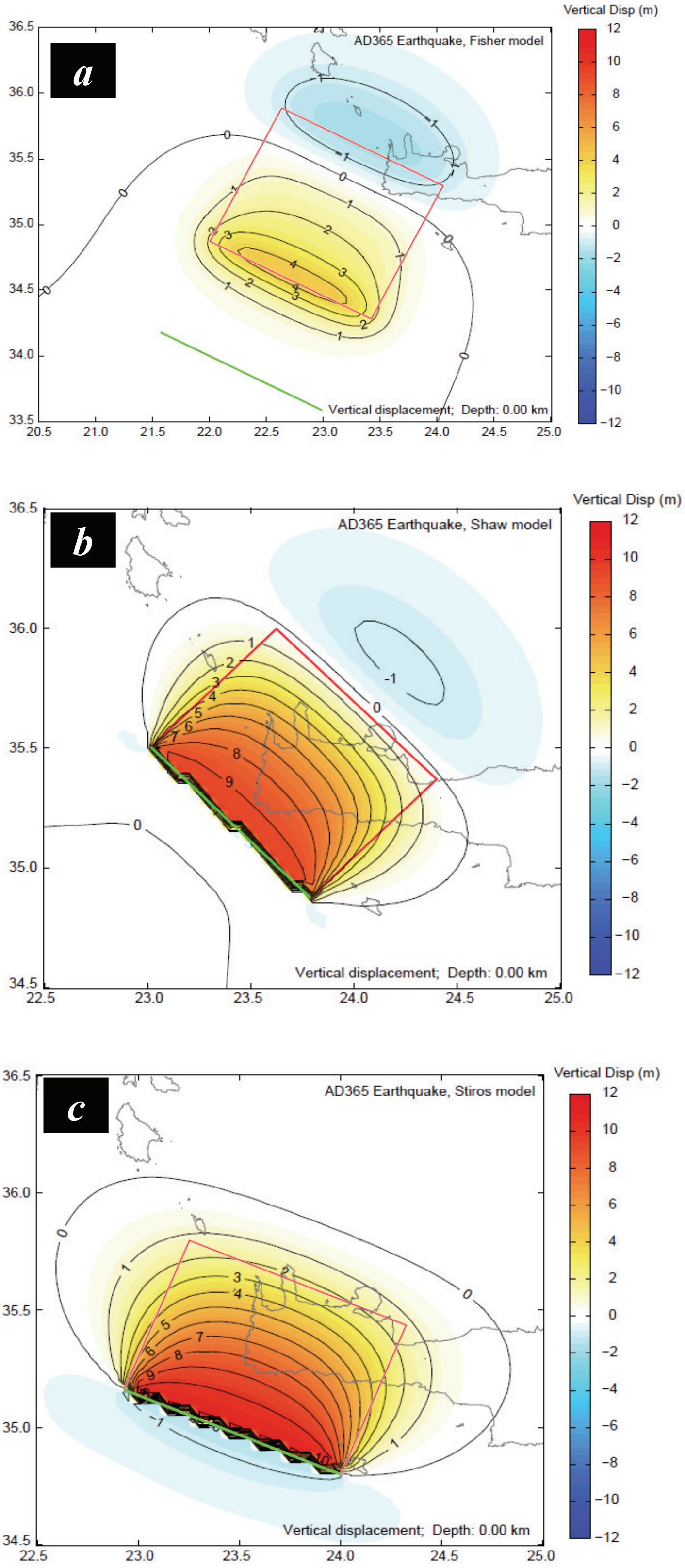

Fischer (2007)

Shaw *et al.* (2008)

Stiros (2010)

Fig.6. Crustal Displacements, Upheaval Generating Area by Fischer (2007) , Shaw *et al.* (2008) and Stiros (2010) models.

(Coulomb 3.3 software - Toda *et al.*, 2011 - was used in the computations)

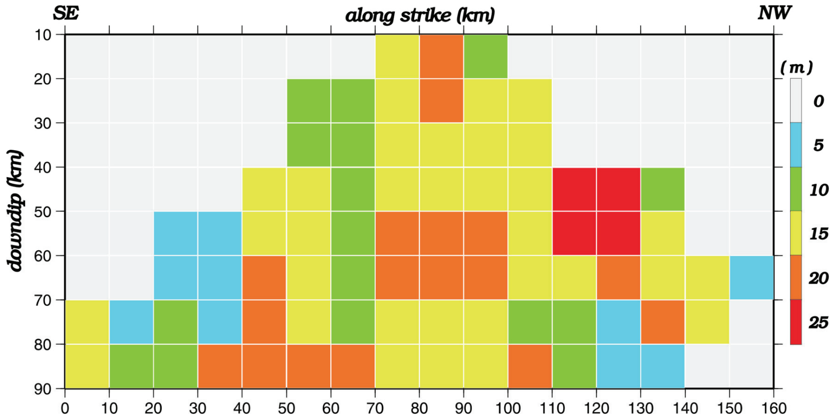

Fig.7. Characteristics of slip distribution of *M*~9 earthquakes in the world Scaling relations of seismic moment, rupture area, average slip, and asperity size for *M*9 subduction-zone earthquakes. (Courtesy of Papadimitriou *et al.*, 2008)

3-4. Site-specific Data

This method requires the underground velocity structure beneath the observation stations. The vertical shear velocity: *Vs* value in the North-West area defined by Karagianni (2005). *Vs* value set at a typical value of Athens, Antikythera and Aptera as *Vs* 3.5 km/sec is 5 km from 2.5 km depth and *Vs* 1.5 km/sec is shallower than 2.5 km depth, for using site-specific amplifications. Subsurface structures were referred as deep *Vs* values provided from Karagianni (2005). Site amplification characteristics of the surface layer ground configuration to fit the transfer function of the one-dimensional wave theory. GL-100 m to 200 m could be *Vs* 700 m/sec among surface 200 m.

At Chania with thick sedimentary layers, and Iraklio, GL-0 m to 100 m calculated the *H*/*V*-spectrum-ratio from the portion of Coda waves from a seismic observation result. As a result, the configuration predominant frequency of 100 m from GL-0 m. *H*/*V*-spectrum-ratio measurement has become a powerful tool for engineers for estimating ground motion characteristics, amplification of soil deposits by horizontal/vertical (*H*/*V*)-spectrum-ratio.

The most efficient way to determine dynamic behaviour of structures is to use the *H*/*V*-spectrum-ratio technique. Spectral analyses were performed from measured data at different down-hole locations. It can be seen that the horizontal motions of the surface waves are very similar to the bottom waves. Result of the calculation (**Fig.8**), the *H*/*V* spectrum peak appeared 0.4 Hz and 1.2 Hz in Chania (set the configuration layer at a depth of 100 m in seismic response analyses of horizontally layered for one-dimensional soil deposits correspond to the *H*/*V*-spectrum-ratio). The *H*/*V*-spectrum-ratio has two peaks at 3 Hz and 0.7 Hz at Iraklio (the soil profile of 100 m surface layer arranges in seismic response analyses of horizontally layered for one-dimensional soil deposits correspond to the peak of the primary and secondary).

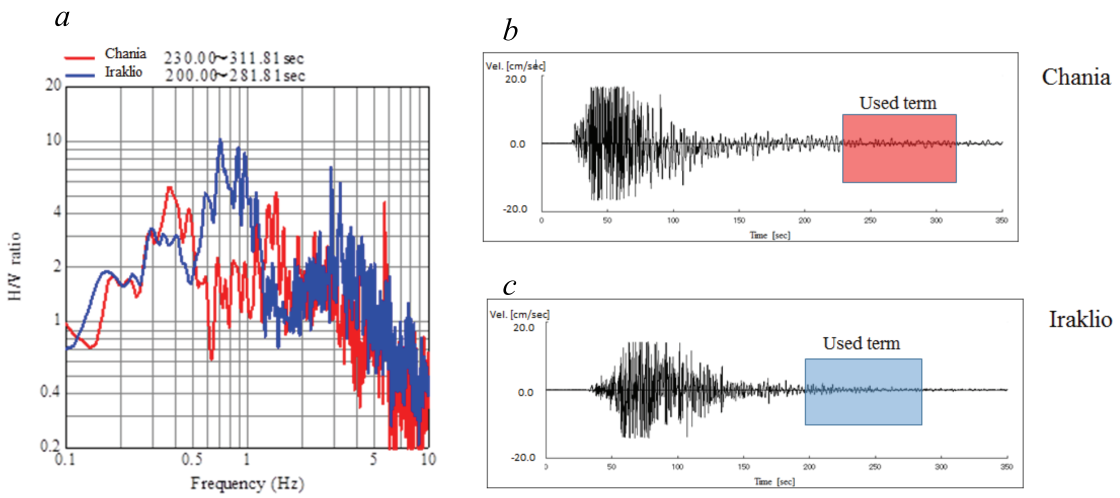

Fig.8. *H*/*V* Spectrum at Chania and Iraklio site. At Chania with thick sedimentary layers, and to 100 m calculated the *H*/*V* spectrum (*a*) from the portion of Coda waves (Chania: 230.00 to 31 Iraklio: 200.00 to 281.81 sec (*c*)) of a seismic observation result.

3-5. Estimation of the AD 365 Earthquake Ground Motions Waveforms

Ground motions estimated by using the stochastic Green's function method. The stochastic Green's function method, which has been discussed in detail by Irikura (1986) and Kamae & Irikura (1994) is a method to simulate ground motions from an extended fault on the basis of the representation theorem of elastodynamics (see Appendix).

Fig. 9 and **Fig.10** shows the estimation of the AD 365 earthquake velocity synthetic waveforms and response spectrum. At Phalasarna, 10 km from the epicentre, estimated velocity was 102 cm/sec. At Antikythera Island, 50 km from the epicentre, the estimated velocity was 57 cm/sec. At Chania, 50 km from the epicentre, the estimated velocity was 108 cm/sec. At Aptra, 75 km from the epicentre, the estimated velocity was 55 cm/sec. At Iraklio, 150 km from the epicentre, the estimated velocity was 41 cm/sec. At Athene, 270 km from the epicentre, the estimated velocity was 2 cm/sec, these values reduce by distance from the epicentre although the duration time expands to 200 sec. The velocity response spectrum for the synthetic waveforms at Chania and Irakio sites show dominant natural period at 0.5 sec (2 Hz), this periods cause a non-liner effect for a sedimentary layer.

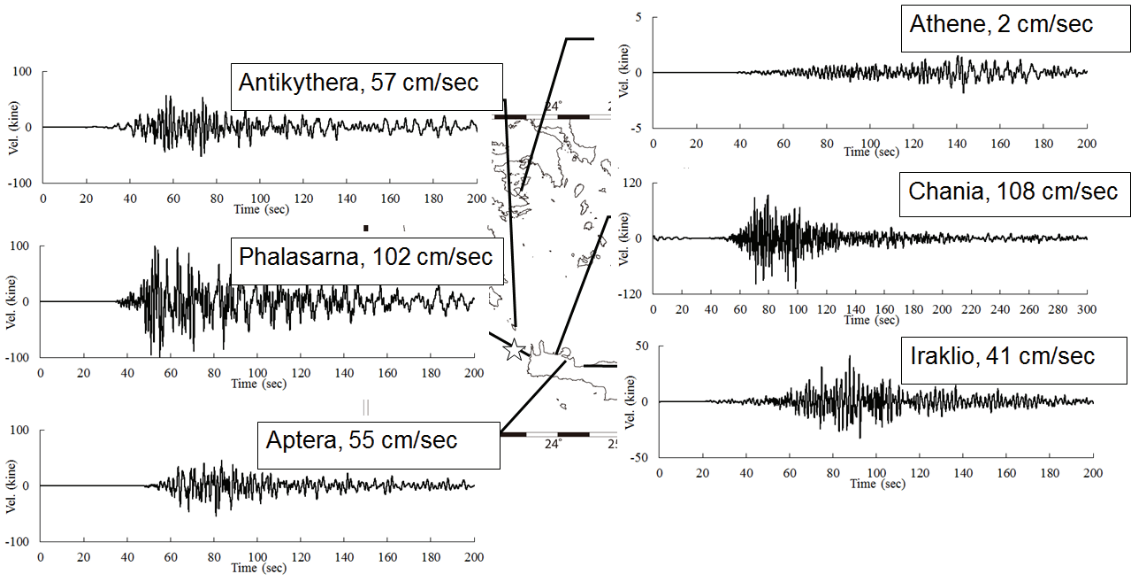

Fig. 9. Estimation of the AD 365 Earthquake synthetic velocity waveforms.

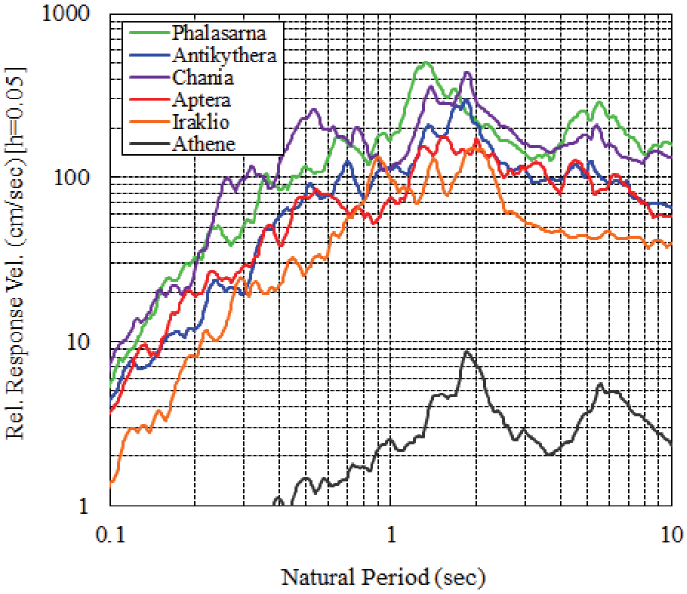

Fig. 10. Comparison of the velocity response spectrum for the synthetic waveforms.

Evidence of 9 m upheaval by the AD 365 earthquake movement are first: detailed survey and radiocarbon dates by Pirazzoli *et al.* (1996), second: the date of casualties' by coins found in a collapsed house by Stiros (2010), third: the ruins of an old harbor and it's quay wall. Moreover, value of upheaval distribution using the calculation formula of Okada (1992) compared to Stiros (2010), Shaw *et al.* (2008) and Papadimitriou *et al.* (2008) model.

Comparision of upheaval distribution using the calculation formula of Okada (1992), set low dip angle along a subduction plate and set high dip angle within overriding plate, the low angle was not suficent for an upheaval, which Pirazzoli (1996) suggested. Shaw *et al.* (2008), Stiros (2010) and Papadimitriou *et al.* (2008) suggested parameters setting that the shallow branch of the subduction zone dips at low angle to and couples with the Aegean lithosphere, while the deep branch dips freely (without coupling) at a high angle beneath the south Aegean trough. According Murotani *et al.*(2013), the average slip distance was around 10 m during the Chili earthquake, 1960 and the Tohoku earthquake, 2011. Thus, this earthquake's slip distance was below 10 m.

Stiros (2010) had set dip angle at 40 degrees and a high angle along within the overriding plate, the strike angle was 292.5 degrees, slip distance to 16 m. Stiros (2010) shaw that elastic dislocation analysis of coastal upheaval data revealed that this earthquake was associated with a reverse fault offshore of southwestern Crete, that its minimum magnitude was 8.5. This model was consistent with the approximate seabed trace of the fault, which observed and calculated displacements due to the modelled fault, and fault depth was a deep as 70 km. This study apply the crustal upheaval by Stiros (2010) modeling study using the calculation formula of Okada (1992).

Shaw *et al.* (2008) suggested that the same process takes place along the entire Hellenic subduction zone, such events may occur approximately once every 800 yr. The stochastic Green's function uses random phases or realistic phases. This study use realistic phases from earthquake records. First, this study used the earthquake records of the Crete Island, *Mw*6.4, 12 Oct. 2013, and used these phases as the stochastic Green's function. Some of these velocity records were saturated (over scale) at Antikythera, Chana and Iraklio. Since the data was saturated at several stations, this study used smaller magnitude records. This study consider that the scaling relationship, *Mw*6.4 was a better selection as a small event. Although, This study used *Mw*4, 12 Oct. 2013, the aftershock of *Mw*6.4, 12 Oct. 2013. Thus, the aftershock of *Mw*6.4, 12 Oct. 2013 record was used as the small event except for Athene.

The Earthquake map of the Crete Island shows high risk area in Chania and Iraklio. Comparison with estimated velocity and this map, high level velocity occurs in Phalasarna (102 cm/sec) and Chania (108 cm/sec). These velocity level correspond to the Great Hanshin-Awaji Earthquake, Japan (1995). Irakulio, even at 150 km from the epicentre, the estimated velocity and velocity was 41 cm/sec, and duration time was 100 sec. This velocity level and duration time will cause a riquefaction in a wide area.

At Aptra, 75 km from the epicentre, estimated velocity is 55 cm/sec. This level will cause heavy damage to a masonry structure. At Aptra, the fortification tower and the entrance collapsed in the AD 365 earthquake.

4. Discussion

4-1. Characteristic of this Earthquake

By using the AD 365 earthquake parameters obtained by Shaw *et al.* (2008) and Papadimitriou and Karakostas. (2008). This study calculated the earthquake's motions.

Observed phase records at seismometer sites located in Crete Island are estimated by using the stochastic Green's function methods for the AD 365 earthquake.

By applying three Green's functions to the fault geometry with a size of 160 km, the shallow branch of the subduction zone dips at low angle to and couples with the Aegean lithosphere gave very good results. Thus, this stochastic simulation this study was applied Papadimitriou and Karakostas (2008)'s parameters. Their study was in the upheaval by using each of the 128 mesh division to give this slip distance. This stochastic Green's function uses these slip distributions at each of the 128 division.

The comparison of the velocity response spectrum for the synthetic waveforms at Chania and Irakio sites show dominant natural periods at 0.5 sec (2 Hz) and 1.0 sec (1 Hz) , these periods will cause a non-liner effect in the sedimetal layer.

Chania and Iraklio sites used *H*/*V*-spectrum-ratio. This *H*/*V*-spectrum-ratio was an effective method for sites with less ground information.

Considering the sediment layer, and the synthetic velocity record of Chania site, which was 50 km from the epicentre, was larger than Phalasarna site velocity, which was 10 km from the epicentre.

The velocity response spectrum for the synthetic waveforms at Chania and Irakio sites show the dominant

4-2. Ancient earthquake damage

Aptra is an ancient city located 30 km east of Chania and 120 km west of Iraklio. It was built in the 15th to 14th centuries BC and was severely damaged by huge earthquakes in the 4th and 7th centuries. Roman occupation of Aptra began in 69 BC, as evidenced in ancient temple ruins, a castle gate, and walls. Catastrophic earthquake damage occurred in 365, concurrent with the fall of the Roman Empire (**Fig.11**).

This study used the inversion results of the Characteristics of slip distribution by Papadimitriou and Karakostas (2008).

Although, the position of the unreliable hypocentre using the position shown in these historical earthquakes. Thus, at Aptra, this study examined three places of the lower fault shown in **Fig.12.** The velocity response spectrum and velocity waveform by the parametric study in the hypocentre position as Case 1 to 3 (**Fig.13**). There was not significant change in the difference of the hypocentre positions in the velocity response spectrum (**Fig.14**). Case 3 cased the maximum value of 78 cm/sec, this value corresponds to 328 gal (**Fig.15**). This study verified that the estimation of damage to masonry by the maximum acceleration. A building inventory survey was conducted in Nepal, Ohsumi *et al.* (2002) and Segawa *et al.* (2002) defined fragility curves from building inventory database including structural type and vulnerability function for each structural type (**Fig.16**). At Aptra, housing and structures might be correspond to AD (adobe) and BM (brick with mud mortar).

By using these fragility curves, this result estimated more than 50% of structure destroyed / partially destroyed.

Also, at Chania with thick sedimentary layers, this study examined three places of the lower fault shown in **Fig.12.** The velocity response spectrum and velocity waveform by the parametric study in the hypocentre position as Case 1 to 3 (**Figs. 17 and 18**). Case 2 cased the maximum value of 126 cm/sec, this value corresponds to 913 gal (**Fig.19**). By using these fragility curves, this result estimated more than 80% of structure destroyed / partially destroyed.

Sieberg (1932) created a seismic map of the Levant. **Fig. 20** show the distribution of seismic intensity for ancient earthquakes (1886, 1903, 1926, 1956) around Crete (Sieberg, 1932). According to Wyss and Baer (1981), the characteristics of these earthquakes may be summarized as below.

1) Rupture influenced the whole Hellenic arc.
2) The earthquake motions were felt over vast area.
3) Isoseismal contours were asymmetric. Fairly high intensities were observed in areas distant from the Hellenic arc, while intensities at the other side of the arc decreased sharply.
4) Epicentres were located in the south of Crete Island and the assumed intensities of all these earthquakes reached a degree XI. **Fig. 21** shows the Crete region, with extensive damage to buildings shown in red. In the 1926 earthquake (*M*7.5), the area stretching from Iraklio to Knossos recorded modified Mercalli seismic intensity of 9 to 10. Chania in the north-west of Crete is expected to be high seismic intensity area. Comparison of this seismic map and the examined acceleration at Chania is well explained. Thus, it is necessary to pay attention to the seismic risk at the high densely area with thick sedimentary layers.

Fig.11. Left: Hypothetical representation of the fortification tower and entrance (from Information plate of National Strategic Reference Framework (NSRF) 25th Department of Antiquities) . Right: Entrance of the castle gate of Aptra,. (photo by T. Ohsumi)

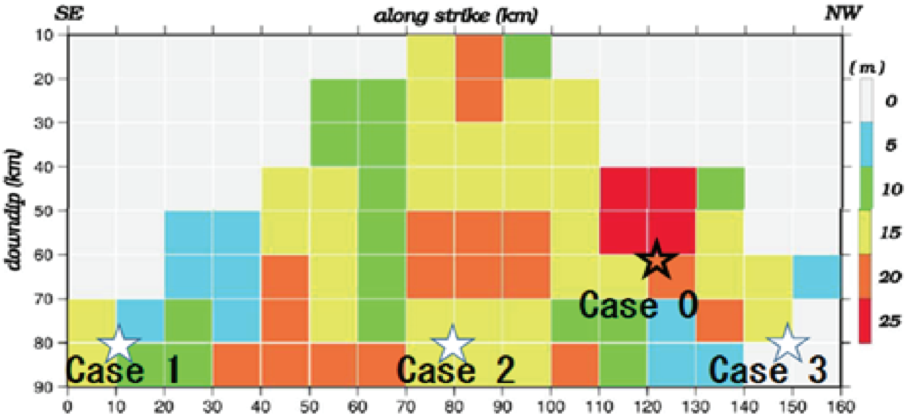

Fig.12. Evalutation of hypocentre positions

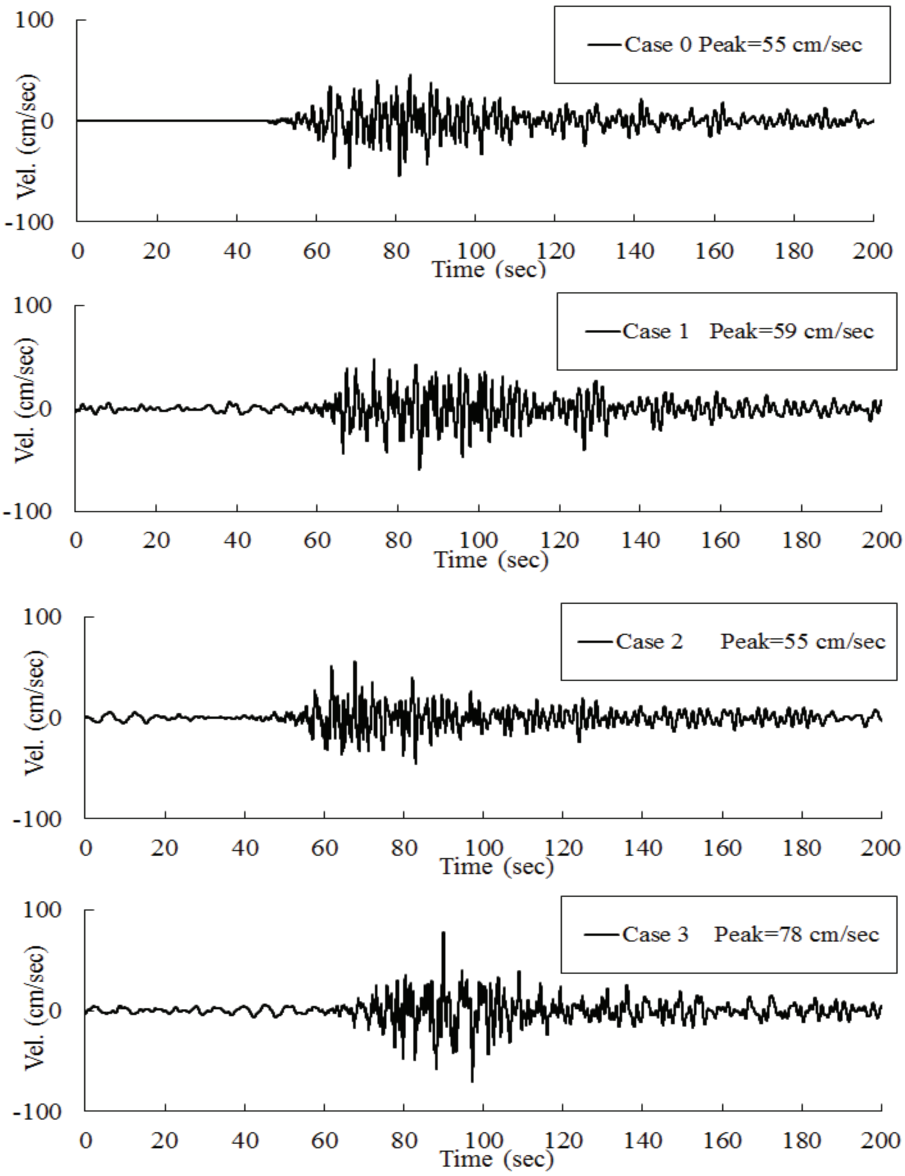

Fig.13. Comparison of velocity waveforms by hypocentre positions at Aptera.

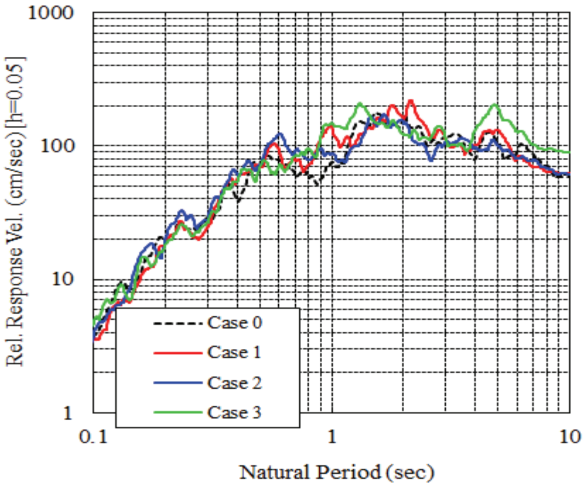

Fig.14. Comparison of velocity response spectrum by hypocentre positions at Aptera.

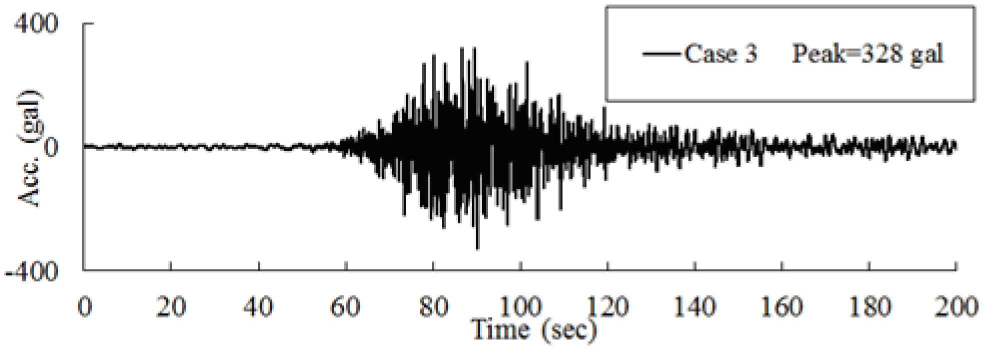

Fig.15. Acceleration waveform (Case 3 : Aptera)

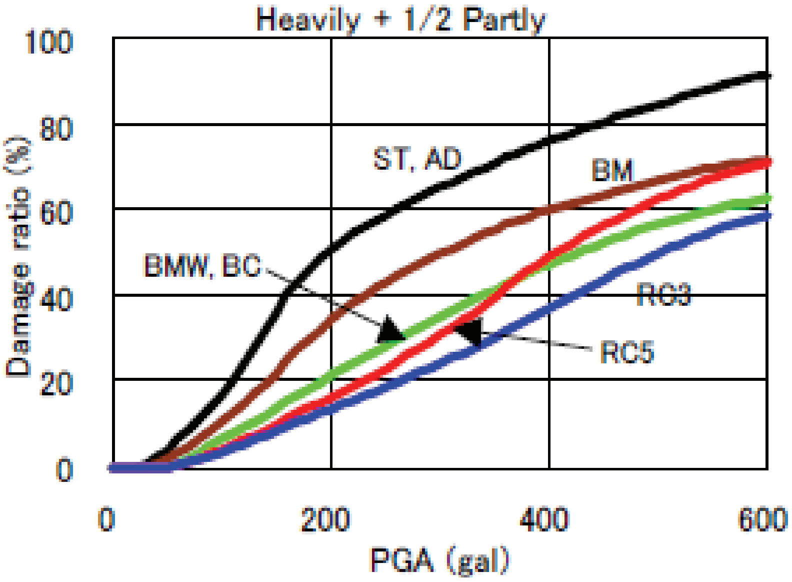

Fig.16. Vulnerability function for each structural type, in Nepal. (Segawa and Ohsumi, *et al* (2002))

AD (adobe) and BM (brick with mud mortar), BC(brick masonry of fired bricks with cement or lime mortar), RC3 (Reinforced concrete frame & un-reinforced brick masonry infill wall with cement mortar. Mostly: 3-storey), RC5 (RC 5-storey)

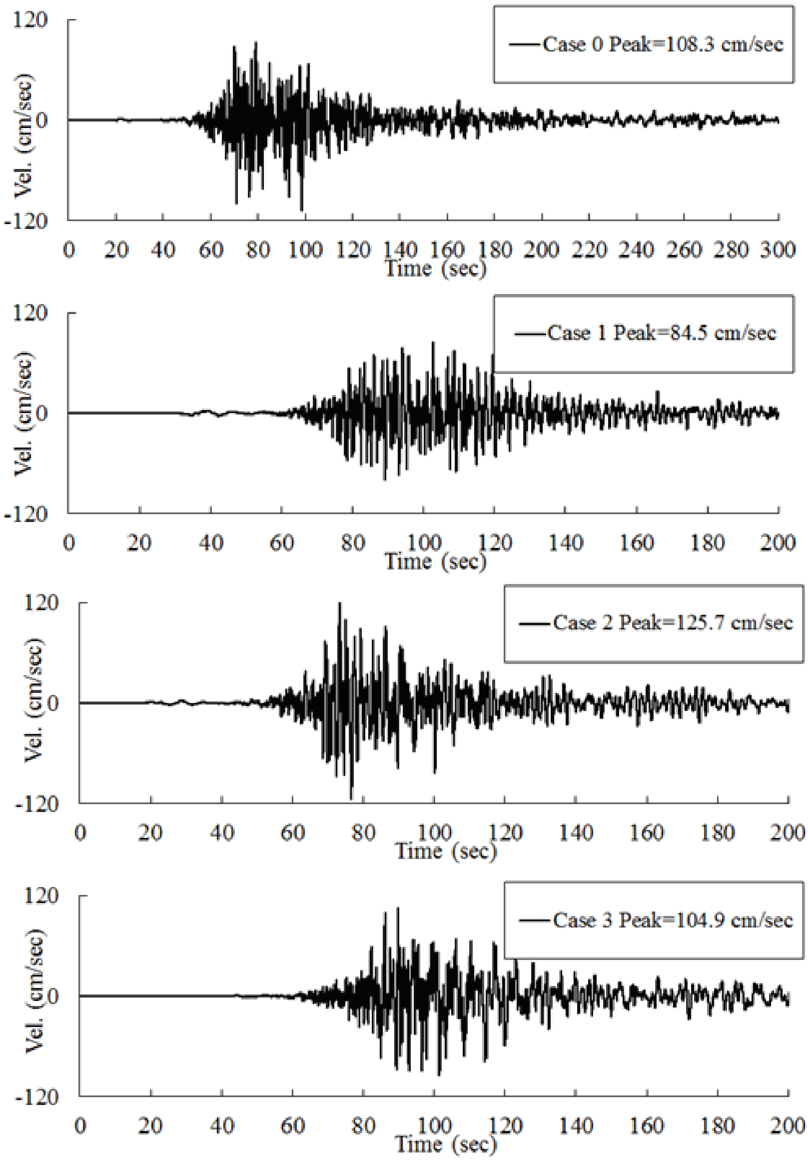

Fig.17. Comparison of velocity waveforms by hypocentre positions at

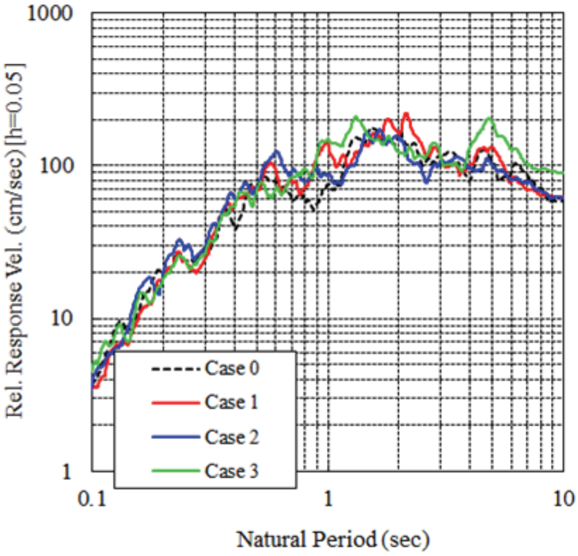

Fig.18. Comparison of velocity response spectrum by hypocentre positions at Chania.

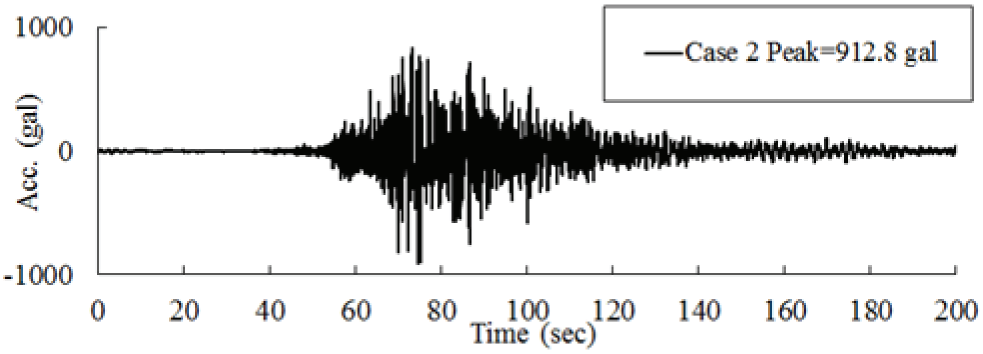

Fig.19. Acceleration waveform (Case 2 : Chania)

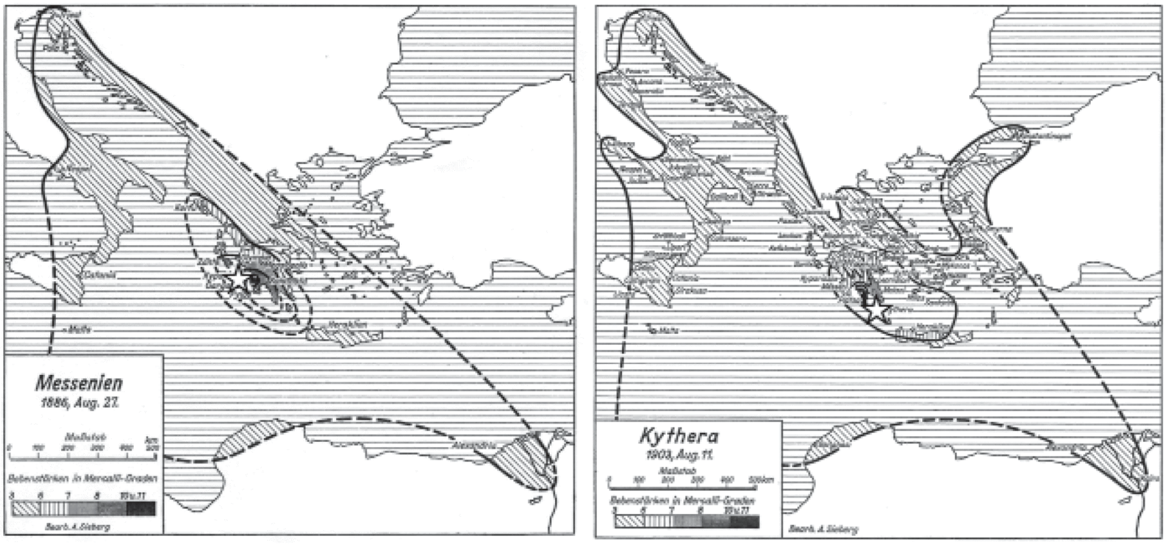

27 August 1886, *M*7.5

11 August 1903, *M*7.9

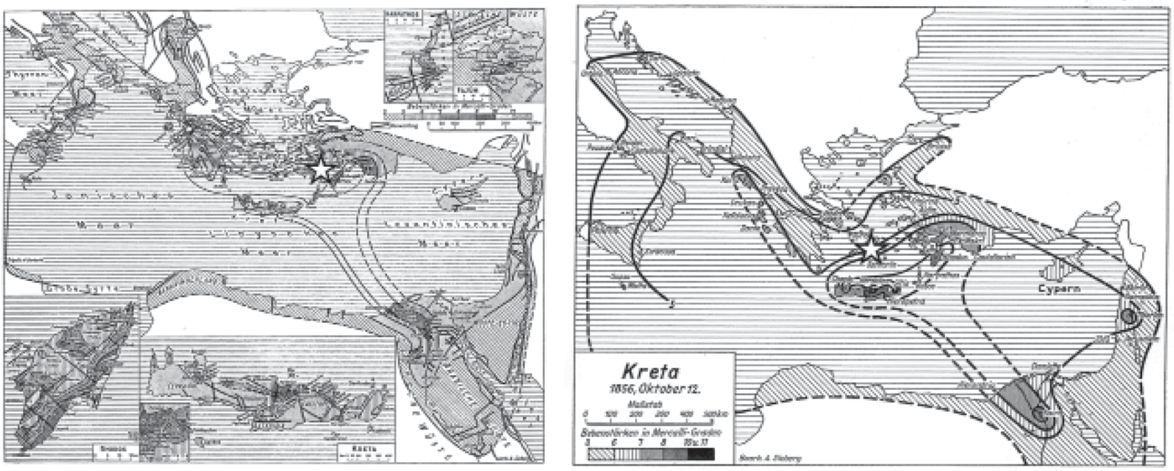

26 June 1926, *M*7.5

12 October 1956, *M*7.5

Fig. 20. The distribution of the seismic intensity of the ancient earthquakes (1886, 1903, 1926, 1956) around Crete. Sieberg (1932).

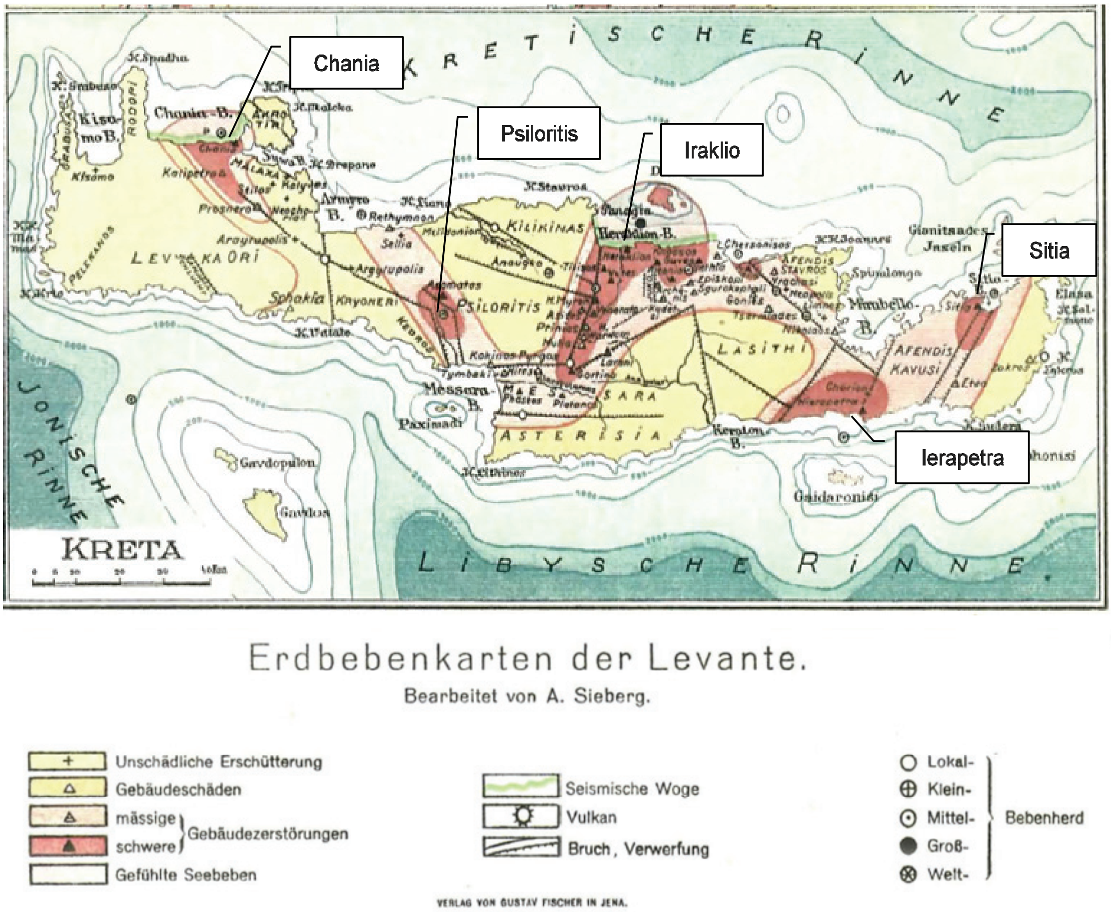

Fig.21. Earthquake map of the Crete Island. (modified from Sieberg ,1932)

Acknowledgments

The authors acknowledge gratefully the kind help during their reconnaissance given by Professor Gerassimos A. Papadopoulos, Institute of Geodynamics National Observatory of Athens, who provided the authors with important shear velocity structures in the Aegean area. The authors are indebted to Professor Eleftheria Papadimitriou and Associate Professor Vassilis Karakostas, Aristotele University of Thessaloniki, who have provided the authors with important data of the waveform data obtained from the Crete Island.

The authors were provided important information and constructive comments for the stochastic Green's function method by Mr. Yasuhiro Fukushima, Eight-Japan Engineering Consultants Inc.

This study was supported by Grant-in-Aid for Scientific Research No. 24101012 of the Japan Ministry of Education, Culture, Sports, Science and Technology.

Chapter 4

Investigation of Rock Thin Sections from Landslide Screes due to the 2008 Eastern Honshu Earthquake

1. Introduction

An earthquake with a magnitude of 7.2 occurred on June 14, 2008. As a member of the Emergency Survey joint team of the Japan Society of Civil Engineers, the Japanese Geotechnical Society, the Japan Association for Earthquake Engineering and the Japan Landslide Society, this study investigated into the damaged area mainly in Iwaigawa, Ichihazamagawa and Aratozawa from June 15 the day after the earthquake happened. The joint survey team prepared reports from each society and they are submerged in Nakamura (2008) and Miyagi (2008). Focusing on slope failure that caused extensive damage, this study observed the collapse phenomenon from various viewpoints. Housing damage due to this earthquake was quite light. On the other hand, heavy damage was sustained due to landslides. There was a strong possibility that the landslide dams left over had been able to cause debris flow. Since the first activity of Kurikoma volcano 50,000 years ago, volcanic ash has been widely spread throughout this area. In this study, in order to investigate the lake data was taken from geotechnical viewpoints. In addition, typical rock samples were obtained from small, middle and large-scale landslides.

2. Characteristics of this Earthquake

The characteristic of this earthquake were: housing was lightly damage, on the other hand, landslide was heavily damage. The characteristics of the ground motion were calculated by waveforms and response spectrum estimated by empirical Green's function at Aratozawa point.

2-1. Characteristics of the ground motion

For the characteristics of the ground motion, as the yield of housing damage was very slight (**Fig. 1**). Although, Landslides were enormous. Accoding to Goto (2008), **Fig. 2** shows the pseudo velocity response spectra (h=0.05) of these components. Goto (2008) was also shown for comparison to the three K-NET and KiK-net records, which were IWATE25 (Ichinoseki-nishi), IWATE 26 (Ichinoseki-higashi) and MYG005 (Naruko), during 1995 Hyogoken-Nambu (Kobe) earthquake and 2004 Niigata Chuetsu-Oki earthquake in the severely damaged areas. Generally, a peak is located in the record of an earthquake in periods less than 0.5 seconds whereas a severe earthquake has the peak value in periods 1-2 seconds. Hayashi and Mori (2008) compared of earthquake records to wooden housing damage. This case also features experienced such past results as the housing damage.

Fig. 1. Comparison of the lightly damaged house, which was built in 1980, Iwate-Miyagi inland earthquake, 2008 (*Mj*7.2), Ishinomaki, Miyagi prefecture (left: photo. by T. Ohsumi photo taken on 15 June, 2008) and the collapsed house in Niigata Chuetsu-Oki earthquake, 2004 (*Mj* 6.8), Kawaguchi, Nigata, prefecture, (right: photo. by T. Ohsumi taken on Oct.,2004).

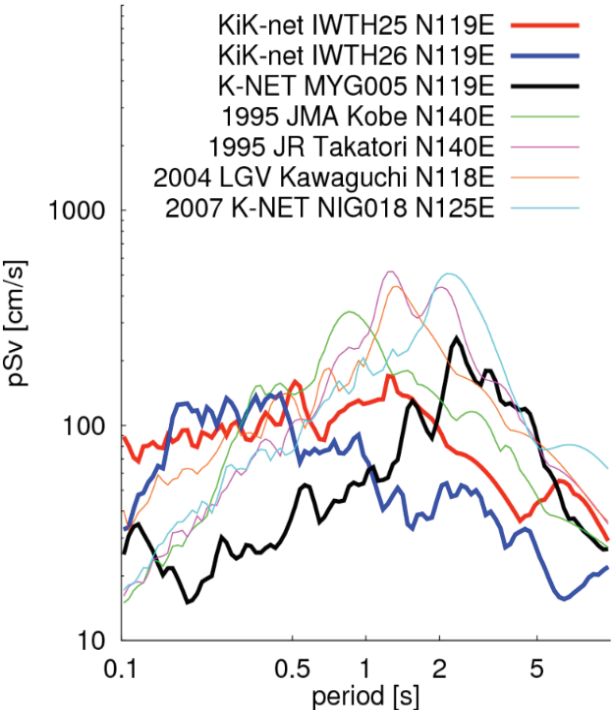

Fig. 2. The pseudo velocity response spectra (h=0.05) of these components. Courtesy of Goto (2008).

A peak is located for the record of this earthquake in periods less than 0.5 seconds whereas a damage earthquake has the peak value in degree for 1-2 seconds in a period.

2-2 Characteristics of the Aratozawa landslide

The large-scale collapse at Aratozaw dam site lies to the south of the Kurikoma mountain caldera. Since the first activity of Kurikoma volcano 50,000 years ago, the volcanic ash has been spread widely throughout the western area from the volcano. In this article, the scale of the caldera is compared to that of the landslides. The collapsed area estimates the quantity of sediment. Sediments from the caldera period accumulated on the large scale pyroclastic flow sediments which filled the caldera. Based on the photomicrograph investigations, rock materials are investigated.

Since the first activity of Kurikoma volcano 50,000 years ago, the volcanic ash has been spread widely throughout the western area of the volcano. Large-scale collapse occurred at the Aratozawa dam. The first activity of Kurikoma volcano 50,000 years ago, the volcanic ash had been spread widely to the western area from the volcano. Large-scale collapse occurred at the Aratozawa dam, in the upper stream part which is located in Kurihara, Miyagi Prefecture. In the collapsed area was estimated of the quantity of sediment to be 1.2 km long and 0.9 km wide, and a maximum thickness was over 50 meters with 70,000,000 m^3. The pumice moved and it continuously filled up the four or five mass movements caused from the quake (**Fig. 3**).

The collapsed gliding slopes were mainly white pumice tuff, others were grain tuff and welded tuff. These were regarded as pyroclastic flow sediment. The landslide topography existed in this area before this earthquake occurred. The collapse was in the upper part of the welded tuff. In the middle part of alternation of strata were white tuffaceous pumice. In the bottom of the laminated retainer consisted of tuffaceous siltstone and tuffaceous sandstone. The upper part of the welded tuff used to be water level surface. The welded tuff was created by the dead-weight of a high density layer. The region that collapsed was formed in strata of about 5 million years ago, called Ono Matsuzawa layer. This layer is composed of pumice tuff substantially horizontal primarily.

According to Nunohara, *et al.* (1999) , Yoshida, *et al.*(1999) , the large-scale landslide which occurred in the Aratozawa Dam upper stream part is located near the caldera rim of the Kurikoma Mts. south crest caldera (**Fig. 4**). In this Figure, the Aratozawa landslides is a small 1/20 part of the caldera of about 15 km width. Moreover, the minor scale landslides also occurred inside the caldera. The lacustrine deposit of the late caldera phases appears on the large-scale pyroclastic flow sediment which fills up the inside of the caldera. By this large-scale collapse, it is observed in the higher rank of the massive pumice tuff, which has a thickness more than 50 m and is covered by the 60-m-thick welded tuff of dacite.

The upper part of the gliding slope is consists of high density welded tuff due to gravity. On the other hand, below the high density sediments low density pumice exists causing instability.

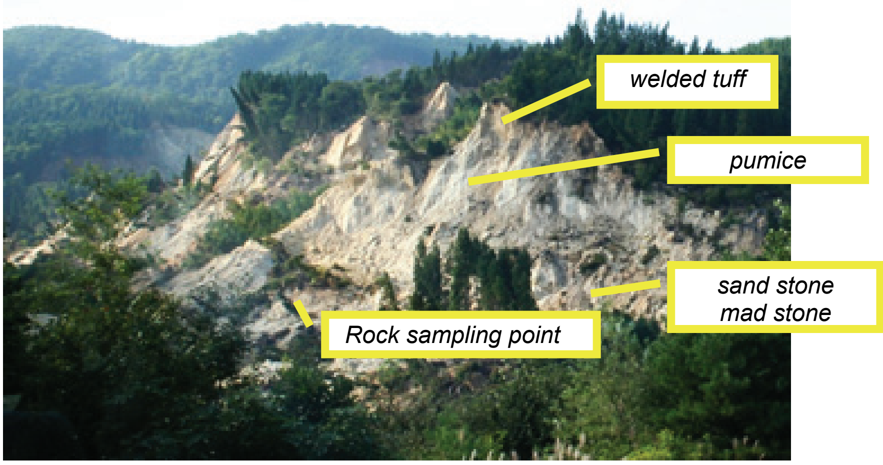

Fig. 3. Full view of the Aratozawa landslide and rock section sampling point (Photo. by T. Ohsumi taken on 10 Sep., 2008) .

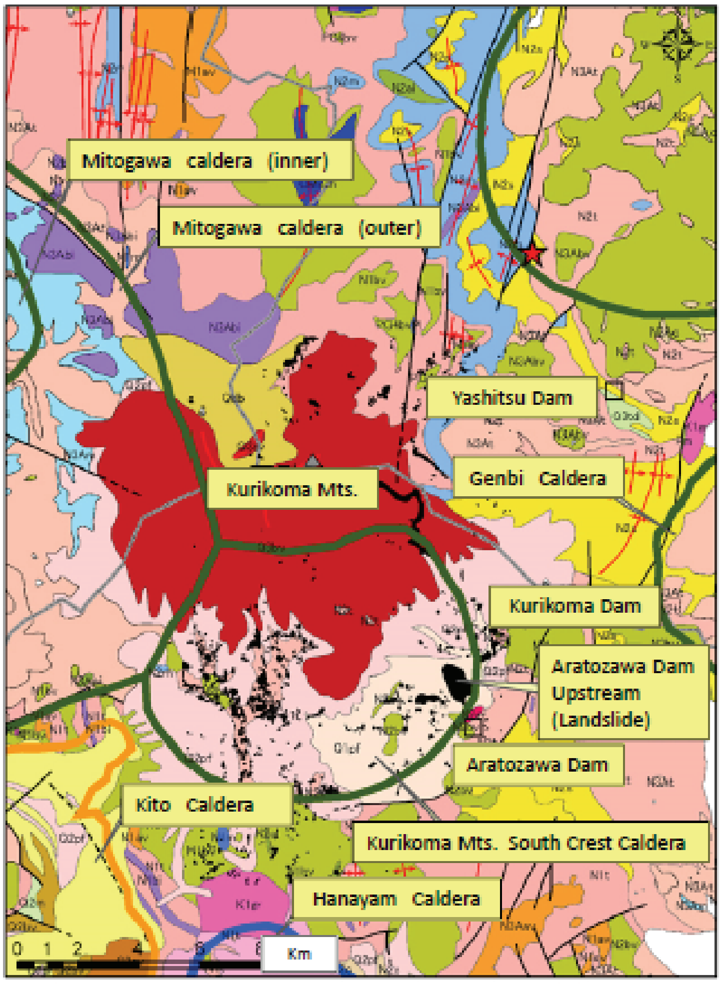

Fig. 4. The GIS database suggested that the caldera structure is closely related to the distribution of the large scale landslides.
(Courtesy of K. Nunohara)

2-3 Estimated erathquake ground motions at Aratozawa

Extremely high accelerations were recorded at the KiK-net IWTH25. The peak acceleration in the vertical component of the surface record was about 4G. Hata, Ohsumi, Nozu and Kamai (2010) estimated based on empirical site amplification and phase effects by seismic waveform at the Aratozawa landslide. Site amplification characteristics at the Aratozawa landslide were evaluated based on the aftershock observation records. Moreover, a characterized source model for strong ground motion prediction was constructed based on the results of waveform inversion for this earthquake. In this study, two sites (L-1, L-2: **Fig. 5**) were observed using the aftershock records. **Fig. 6** shows observation condition and maximum acceleration. L-1 point was landslide prediction area after landslides expansion. L-2 point was extended collapse area after the earthquake. L-3 point was unmoved area. L-3 point is outcropping point. Immediately after the earthquake, accretion value of L-3 and L-1 was same levels. Although, after the land slide extended, accretion value of L-1 was reduced and less than L-3.

According to Ohyagi's aerial photo interplitation (**Fig. 7**), L1 was the point of extended collapse after a few days from the landslide and L-3 was the point of unmoved area. Inoguchi (2010) showed landslide map of Kurikoma mountan and source area of the Aratosawa landslid (**Fig. 8**). In this map, the red line is the landslide area, some of the other landslides also occurred on landslide landform features and L-3 point is out of the landform feature area.

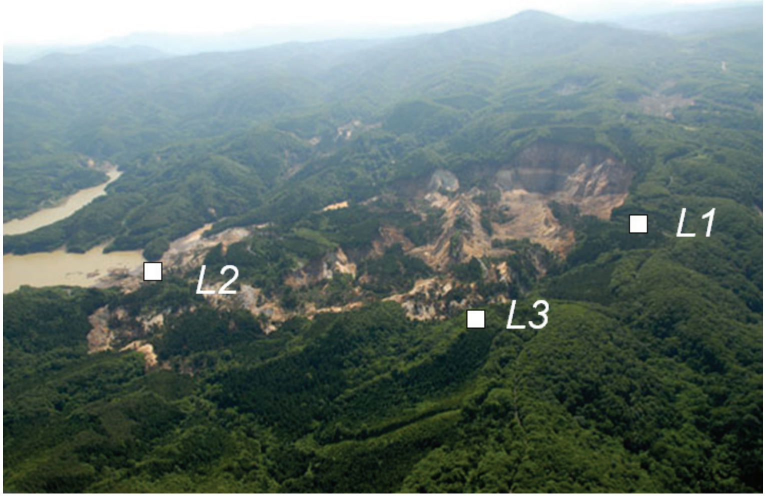

Fig. 5. Bird's-eye view of the Aratozawa landslide and survey points.

（ Photo taken by T. Kamae on July., 2008 ）

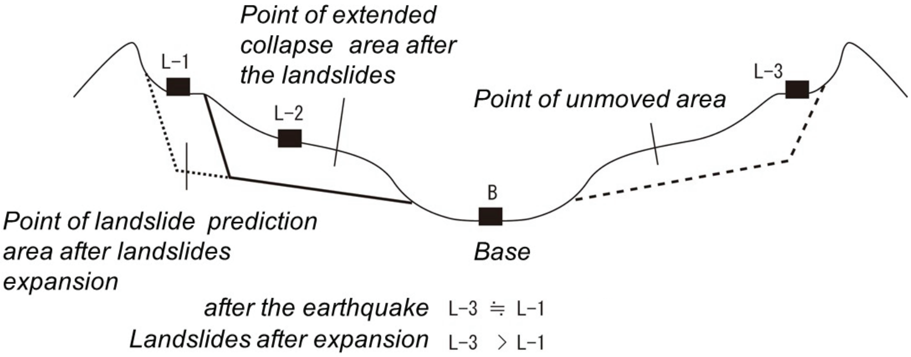

Fig. 6. Observation condition and Maximum acceleration. Courtesy of T. Kamae.

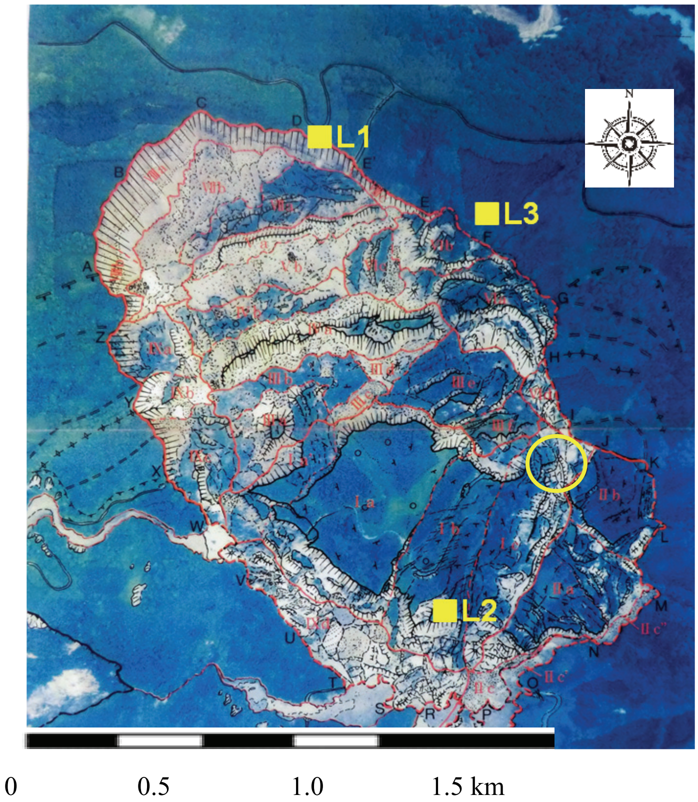

Fig. 7.
Aerial photo interplitiation (Courtesy of N Ohyagi, Photo taken on 16 June, 2008).
Yallow squares are sismogrph setting ponts. Yallow sercle is rock thin section sampling point.

Fig. 8. Landslide map of Mt. Kurikoma and source area of the Aratosawa landslide.

Empirical Green's function method

This study have reproduced the waveforms of the main shock using the empirical Green's function method (Irikura, 1986) by using aftershock records of Aratozawa landslide site (see Appendix). The target site is located in the seismic fault area, and its location is marked by a filled back circle in **Fig. 9.** Hata, Ohsumi, Nozu and Kamai (2010) used the aftershock record, which occurred 15:14 7th July, 2008, as the empirical Green's function method. **Fig. 10** shows the characterized source model. This characterized source model was set a rectangular asperity area of the larger slip area in the final slip model by Nozu (2008) waveform inversion.

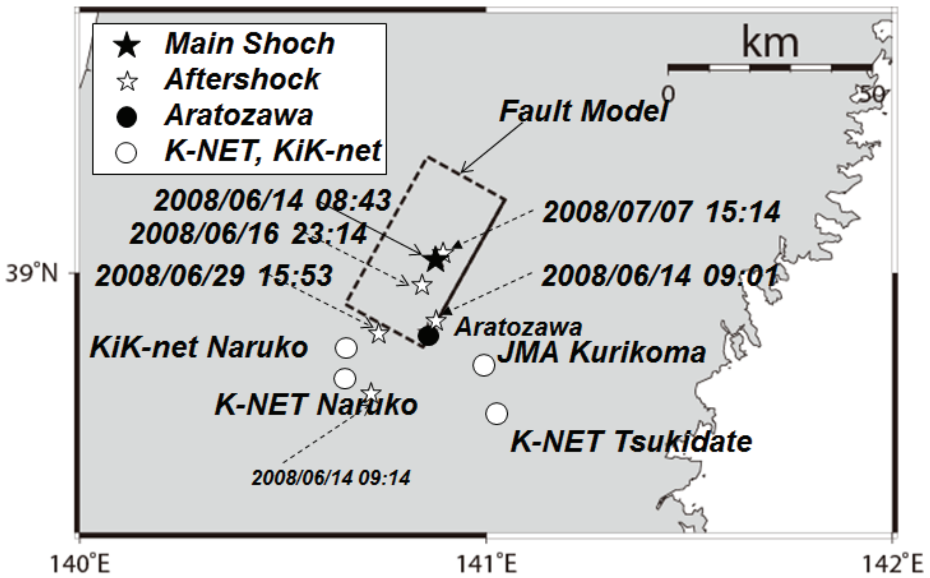

Fig. 9. The characterized source

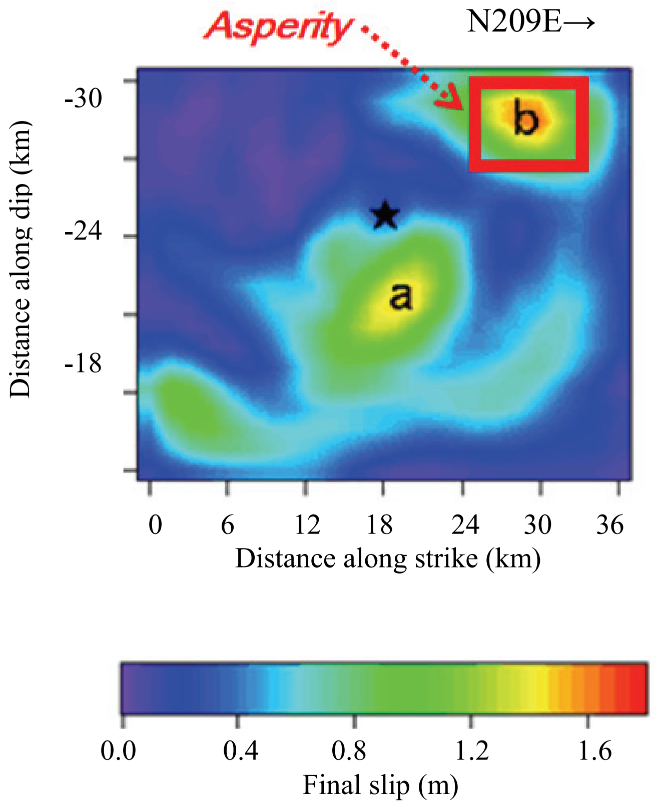

Fig. 10. The characterized source model for strong ground motion prediction, Courtesy of Nozu (2008).

As a result, the maximum horizontal acceleration was estimated L1 at 841 Gal and L-3 at 2,931 Gal during the main shock at the Aratozawa survey points (**Figs. 11**). The comparison of the acceleration response spectrum shown in **Fig. 12**. The maximum horizontal velocity was estimated L1 at 27 cm/sec and L-3 at 34 cm/sec during the main shock at the Aratozawa survey points (**Figs. 13**). The comparison of the velocity response spectrum shown in **Fig. 14**. Reasons for the estimated large ground motion at the L-3 point: the effect of differences in the surface layers thickness of shallower engineering basement, the effect of the seismic characteristic of the gliding slopes and Influence by the topography effect etc.

At L-3, the estimated ground acceleration was approximately 3G, which dominant period was 0.16 second. Thus, large ground motion and dominant 6 Hz frequency caused the landslides in this area. The Great Wenchuan earthquake's dominant frequency was 4 Hz (Zifa, 2008). The Chi-Chi earthquake's dominant frequency was 4 Hz (Chen, 2008) . Dominant frequency around 5 Hz might be a relationship with landslides.

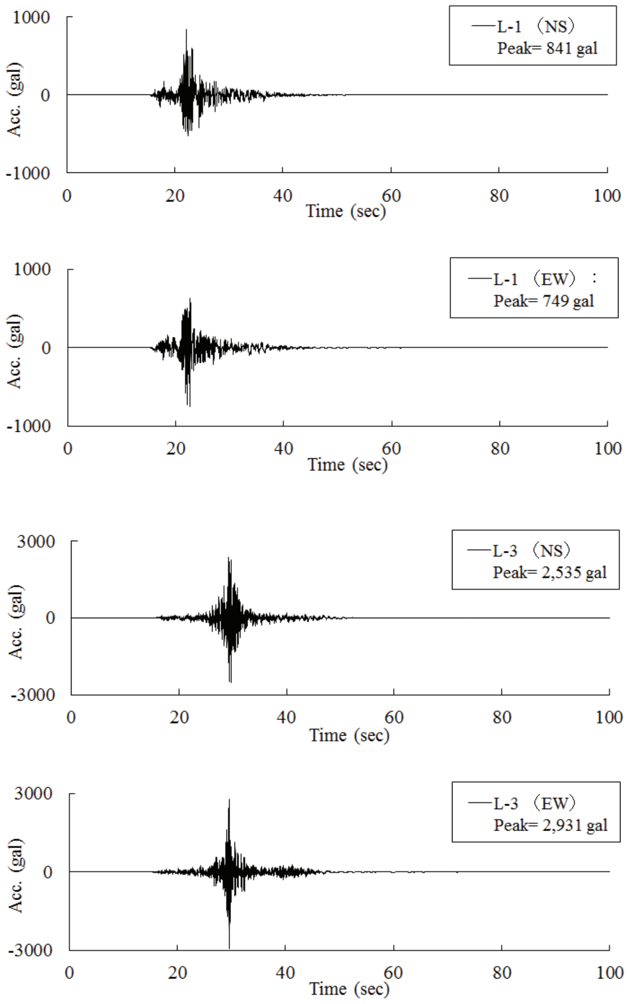

Fig. 11. The estimation of the acceleration waveform at the Aratozawa landslide point during the main shock.

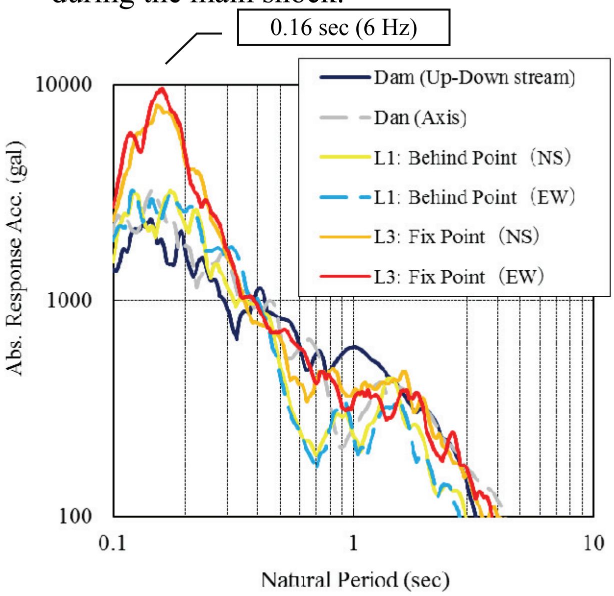

Fig. 12. The comparison of the acceleration response spectrum.

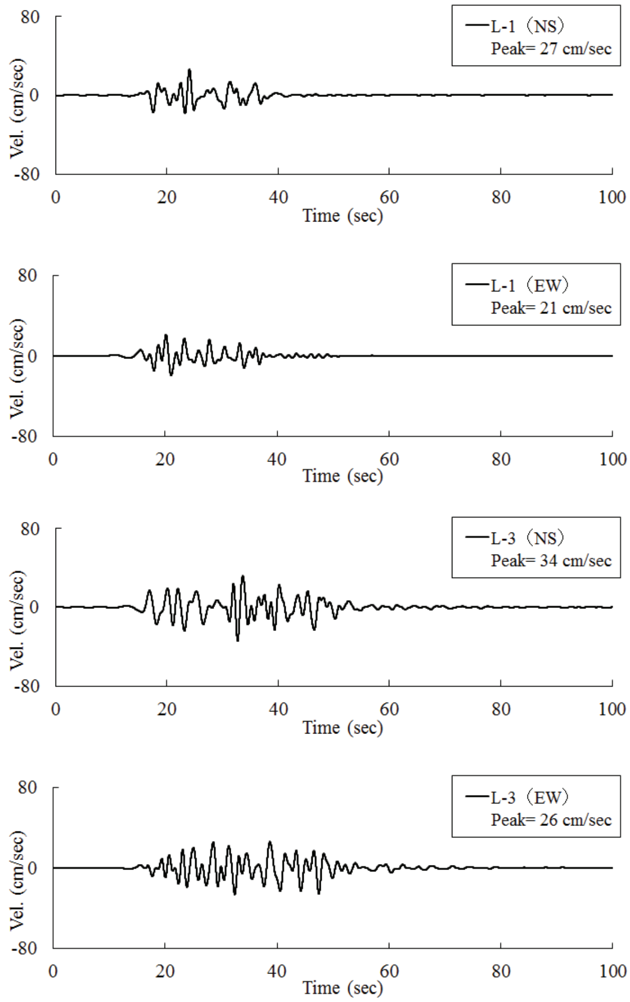

Fig. 13. The estimation of the velocity waveform at the Aratozawa point landslide during the main shock.

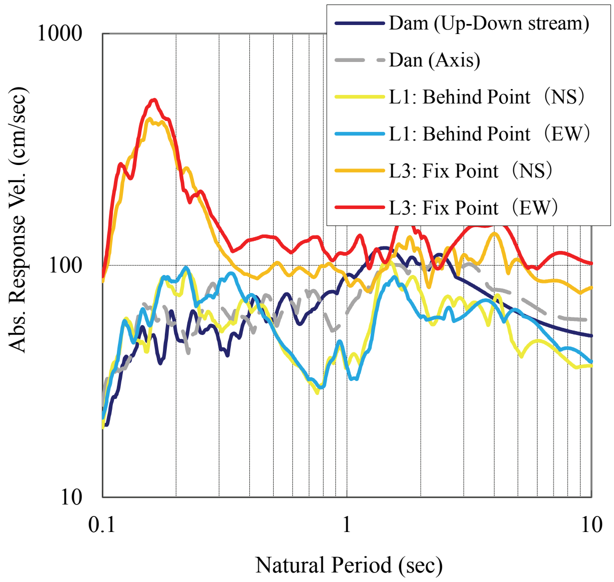

Fig. 14. The comparison of the velocity response spectrum.

3. Photomicrograph Investigation of Rock Thin Sections

The greatest landslide on record in Japan occurred at Aratozawa near the the Eastern Honshu Earthquake fault. Therefore, evaluation by high resolution of the strong seismic motion at the Aratozawa landslide is very important in analyzing the landslide's mechanism. Hence, the evaluation of seismic response characteristics at this site is necessary. Many landslides occurred in a large area during the Eastern Honshu Earthquake. The number of slope failures were enormous, this earthquake cased 10 or more landslide dams.

At one landslide dam, the high water level was reached the day after the earthquake occurred, 15th June (**Fig. 15**). On the main road close to the river, a police vehicle was calling a warning to residents to be vigilance for sudden debris flow due to river blockage up river (**Fig. 16**).

In **Fig. 17**, the small-scale collapse points is located on a slope at the side of National Route 342, and the medium-scale collapse point is located on a down slope very close to the Yabitsu Dam / Weir. At each of the two points in **Fig. 18**, rock samples were retrieved and their thin sections were studied under a polarizing microscope.

Typical rock samples were obtained from the small, middle and large-scale landslides. Based on the photomicrograph investigations, factors for each scale thier collapse and rock materials were cmpared.

Fig. 15. Landslide dam created at Iwai River.

(Photo. by T. Ohsumi taken on 15 June, 2008)

Fig. 16. Police vehicle was calling a warning to residents to be vigilance for sudden debris flow due to river blockage up river.

(Photo. by T. Ohsumi taken on 15 June, 2008)

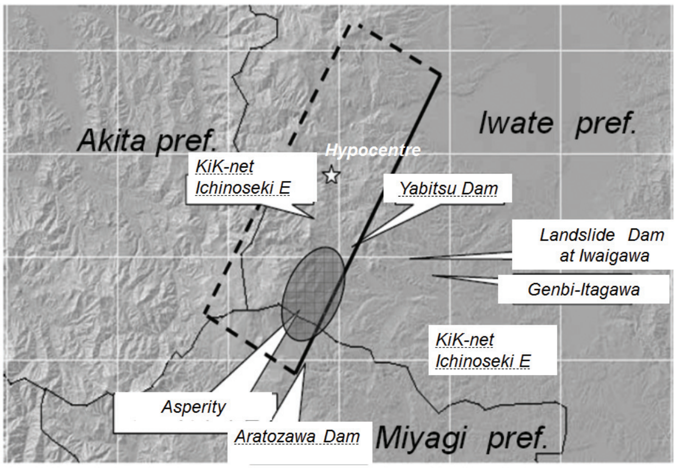

Fig. 17. Fault model.

(Kashmir 3D use,
Courtesy of Yagi and Nishimura by Fault model)

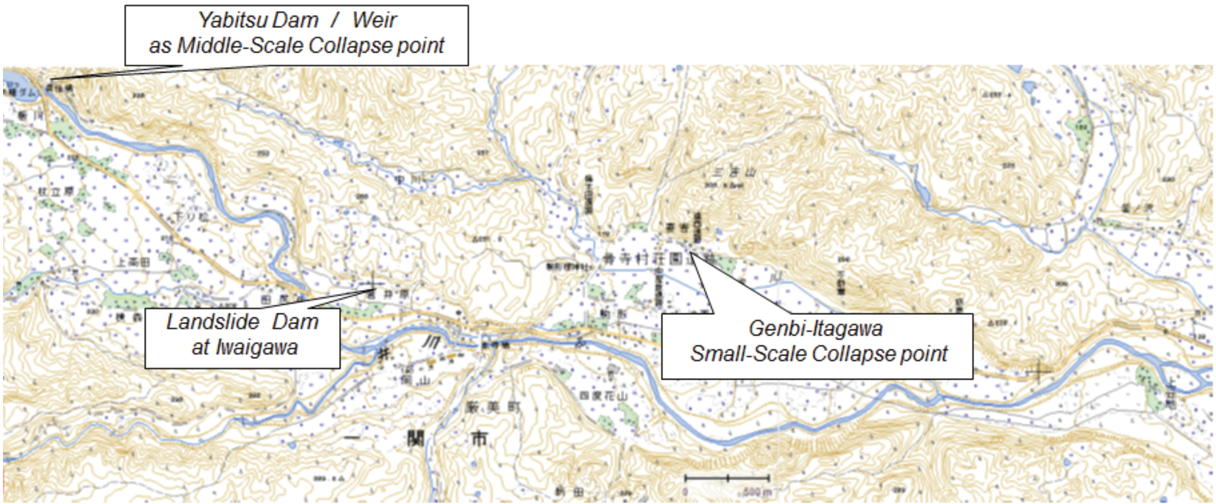

(Wachi-zu, Geospatial Information Authority of Japan)

Fig. 18. Survey points.

3-1 Small-Scale Collapse point: Genbi Itagawa

On National Route 342 parallel to Ichinoseki Genbi-Itagawa in Iwate Prefecture, a lot of the small-scale slope collapses occurred (**Figs. 19, 20 and 21**). Collapsed slope caused road and river blockages, many road closures were long term.

Fig. 19. Full view of Ichinoseki Genbi-Itagawa small-scale slope collapses near National Route 342.

Fig. 20. Close-up of Ichinoseki Genbi-Itagawa small-scale slope collapses near National Route 342.

Fig. 21. Landslide Scree from the middle-scale collapse near National Route 342.

A piece of the rock sample at the Genbi Itagawa point Quarternary andesite lava consisted of volcanic glass, homblende, cleavage and pagioclase (**Fig.22**).

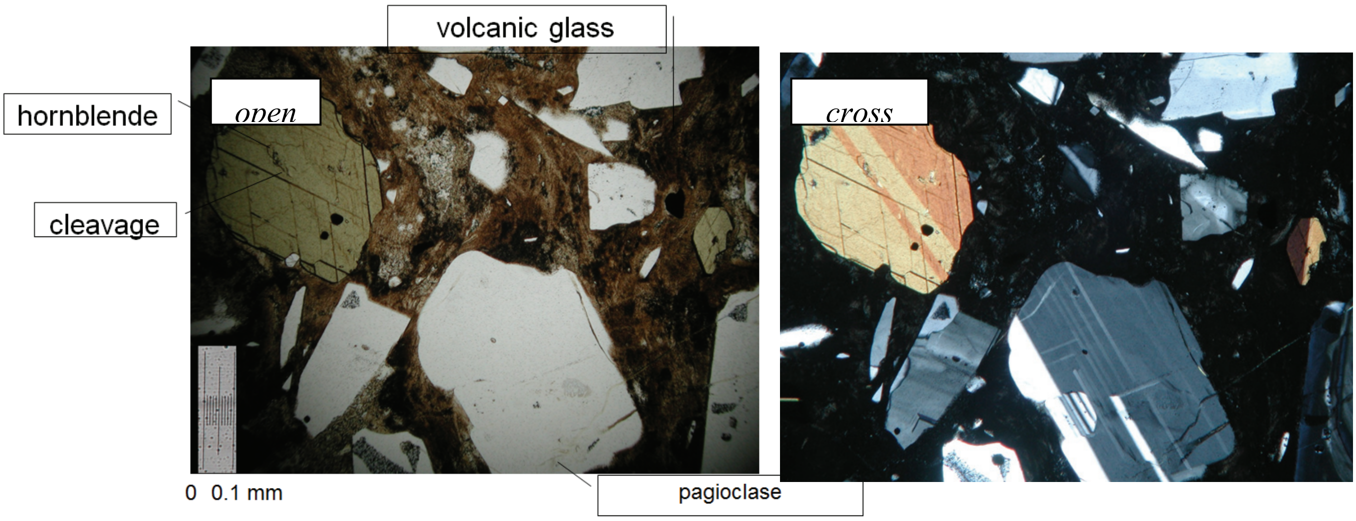

Fig. 22. Thin section (Quality andesite lava) of the small-scale collapse near National Route 342.

3-2 Middle-Scale Collapse: Yabitsu Dam / Weir

Upstream of the Iwai River Yabitsu Dam / Weir, the left bank is cap rock with andesite on the top of the Neogene tuff layer. Along the clear knick line boundary between the tuff layer and andesite, slope failure occurred in several places. At Yabitsu Dam / Weir site, a footbridge downstream, (length is 24 m), collapsed (**Fig. 23**). Because the left bank exfoliated, the bridge collapsed by the bedrock of the abutment.

Close to the bridge, another slope also collapsed,this slope “Sanno-Iwaotani” has been revered as jinushigami (Tutelary deity) of the Enryaku-ji temple on Mt Hiei (**Fig. 24**). It is evidence that this slope had been stable for several hundred years. A piece of the rock sample Yabitsu Dam / Weir point volcanic ashes sediment consisted of quartz, volcanic glass, pore, pumiceous volcanic glass and rockfragment (**Fig. 25**).

Fig. 23. Collapsed footbridge downstream (length is 24 m) at Yabitsu Dam / Weir site.

（Photo taken by T. Ohsumi on 15th July, 2008.）

Fig. 24. Full view of downstream left bank occurred the middle-scale collapses. Close to the bridge, another slope also collapsed,this slope “Sanno-Iwaotani” has been revered as jinushigami (Tutelary deity) of the Enryaku-ji temple on Mt Hiei. It is evidence that this slope had been stable for several hundred years.
(Photo. by T. Ohsumi taken on 15th July, 2008.)

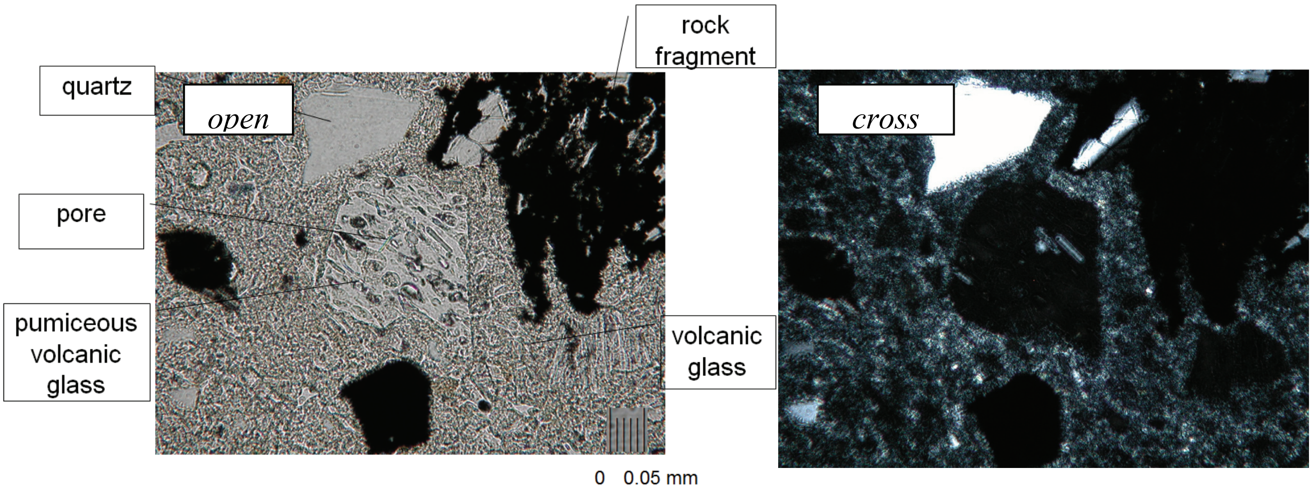

Fig. 25. Thin section (volcanic ashes sediment (tuff)) from the middle scale collapse near Yabitsu Dam / Weir site.

3-3 Large-Scale Collapse: Aratozawa Dam Site

A piece of the mudstone at the Aratozawa point consisted of lamination and sand-mud alternating strata (alternating strata of sand and mud are also distributed at the bottom of the Aratozawa lake). This sedimentation (mudstone) is thought to be from the Quarternary Period. A piece of sandstone also obtained from the Aratozawa point (**Fig. 3**) consisted of quartz, pumice, volcanic fragments, feldspar, pyroxene and diatom (**Fig. 26**). Diatoms can be clearly seen in the mudstone at the Aratozawa point obtained from the Aratozawa large-scale landslide. Thus, this proves that sediment from the caldera period accumulated on the large scale pyroclastic flow sediment, which filled the caldera.

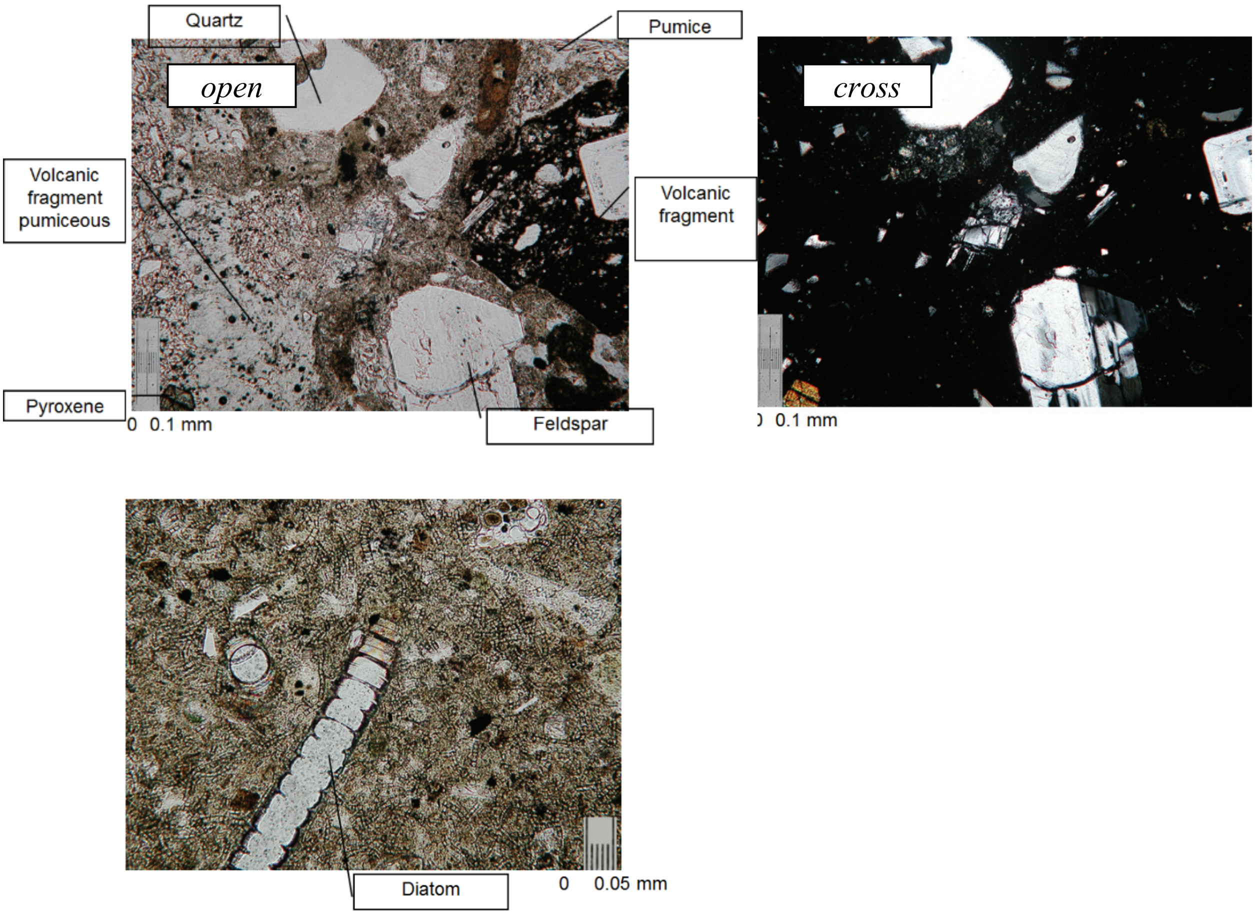

Fig. 26. Photomicrography of rock thin sections from Aratozawa landslide point.

4. Characteristic of this Earthquake Summary and Conclusions

1) At Aratozawa landslide point, the estimated ground acceleration was approximately 3G. Thus, large acceleration caused landslides in this area. Since the first activity of Kurikoma volcano 50,000 years ago, the volcanic ash has been spread widely throughout the western area from the volcano.

2) A sample of mudstone from the Aratozawa point consisted of lamination, and sand mud alternating strata. This shows evidence that it is very similar and probably from the alternating strata of sand and mud that were distributed at the bottom of a lake in the past. This sedimentation is thought to be from the Quarternary Period.Diatoms can be seen clearly in the mudstone at Aratozawa Point. Thus, this proves that sediments from the caldera period accumulated on the large scale pyroclastic flow sediments which filled the caldera.

3) During the volcanic activity period the pyroclastic flow widely covered the surface due to the fact that the gliding slope was not very steep as section **Fig.27** A-A' solid line. The extensive area of gentle slope caused a wide collapse as section **Fig.27** B-B' broken line. The landslide slope was found by boring exploration by MAFF.

6) Aratozawa landslide was lateral spread and attributed to the fact that many landslides were translational slides of the bedding plane-slide type, and a slippery stratum were caused by the earthquake.

7) The upper part of the gliding slope of the Aratozawa Point consists of high density welded tuff due to gravity. This is evidence that water above the present ground water level used to exist. On the other hand, below the high density sediments low density pumice exists causing instability.

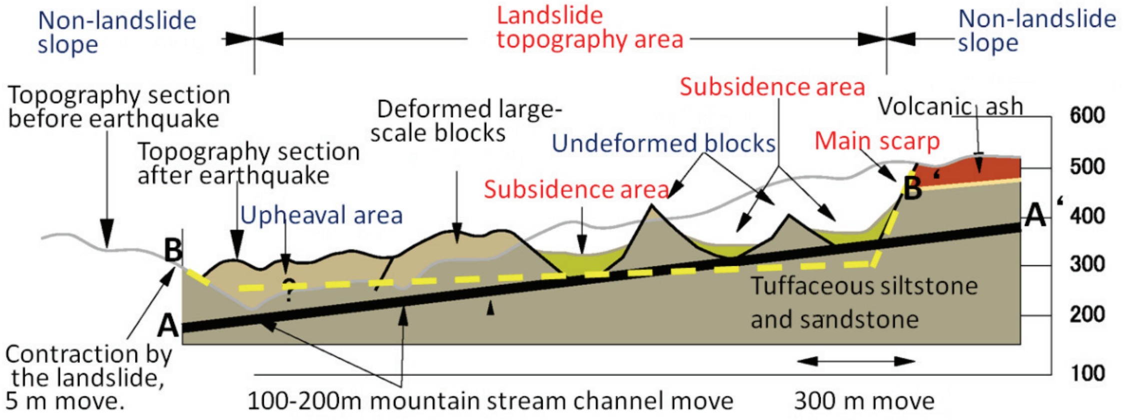

Fig. 27. Aratozawa landslide cross section (Modified from JGS; Miyagi, 2008).
JGS defined very steep as section A-A'. MAFF defined widely collapse as section B-B' from the boring exploration.

Acknowledgments

This research of photomicrograph investigation for rock thin sections was supported by Emirates Professor Yujiro Ogawa with Tsukuba University. I also thank Dr. Norio Ohyagi with the Fukada Geological Institute provided which valuable geological information from the Aratozawa landslide.

Chapter 5

Final Remarks

The vein structure is the starting point of the rupture shape. A vein structure is a distinct structure found in deep sea sediment at convergent plate boundaries of closely spaced mud-filled veins which form an array mostly parallel to the bedding plane in hemipelagic clay and siliceous mudstone from around the Myosin age. The regular spacing order, the constant ratio between array height and vein spacing reflects resonance. The shape of the veins and their arrangement cause reflects Riedel shearing.

In analog experiments, at both ends of the shear box, clockwise rotation of blocks are generated, which is indicated by the discontinuous displacement of the markers. In a strike-slip fault, fractures are generated in the region under the tension area. In numerical experiments, the model in which both ends are free indicated the development of extensional basins or sag ponds along the strike-slip fault. The extensional fields are susceptible to subsidence, while contraction fields are susceptible to upheaval. This result explains the typical dextral fault as a pull-apart basin (*e.g.*, the Mineoka Tectonic Belt in the Boso Peninsula, Japan).

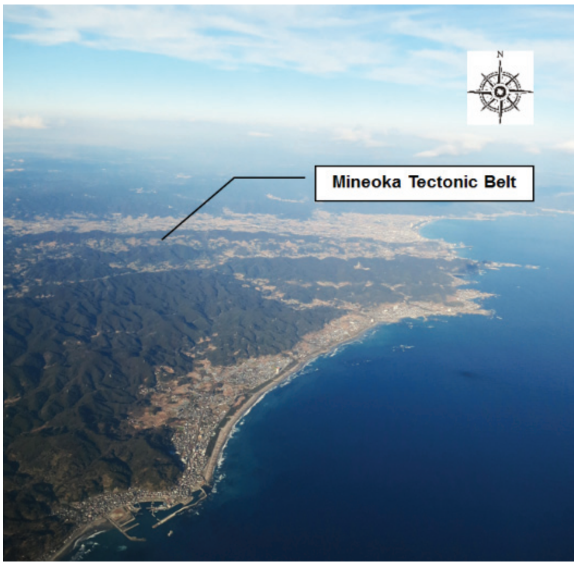

Fig. 1. Eastern Mineoka Belt, Kamogawa City, Chiba Prefecture (Photo by T. Ohsumi, looking to North)

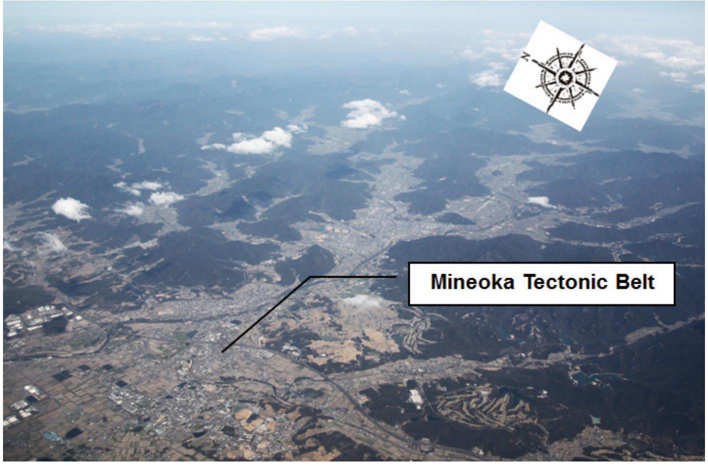

Fig. 2. Western Mineoka Belt, Kamogawa City, Chiba Prefecture (Photo by T. Ohsumi, looking to East)

The ancient upheaval of the Crete Island earthquake can be estimated for the AD 365 earthquake's waveform. This H/V-spectrum-ratio was an effective method for sites with less ground information. The calculation of the AD365 earthquake's waveform gave an indication of the maximum acceleration. Thus, an estimation of the damage to masonry structures could be made. The ancient Crete city of Aptra amd Chania were both hit by the AD365 earthquake. Aptera built on out-cropping rock will be 80 % destroyed whereas Chania built on thick sedimentary layers will be completely destroyed. Chania in the north-west of Crete is expected to be high seismic intensity area. Thus, it is necessary to pay attention to the seismic risk at the high densely populated area with thick sedimentary layers.

At the Aratozawa landslide point, the estimated ground acceleration was approximately 3 G. Thus, the large acceleration caused landslides in this area. At Aratozawa there were lateral spread landslides and these attributed to the fact that many landslides were translational slides of the bedding plane-slide type. The upper part of the gliding slope of the Aratozawa Point consists of high density welded tuff, under welded tuff pumice exists, which is low density, such an unstable situation causes landslides. Japan has very active volcanic activity which can cause wide spread damage.

Acknowledgments

I express my indebtedness and deep sense of gratitude to my supervisor Associate Professor Yuji Yagi, Faculty of Life and Environmental Science, University of Tsukuba, for his continuous support, advices and guidance throughout the course of this study, preparing this thesis and related manuscripts. I am deeply indebted to Professor Yoji Arakawa, Associate Professor Bogdan Enescu and Dr. Shigeru Takizawa for helpful advice and for reading the manuscript. I would like to express my gratitude to Professor Kenichiro Hayashi, Dr. Ryo Anma and Specially Appointed Professor Yoshiyuki Kaneda with Nagoya University, for his kind help.

To the NIED majestic members, I will not forget their kind and sincere help. I thank Dr. Hiroyuki Fujiwara, Dr. Shin Aoi, Dr. Hiromitsu Nakamura and Dr. Katsumi Kimura for their kind and sincere help.

I pay my sincere gratitude to my wife Yuri who gives me strong encouragement. My special thanks to Emeritus Professor Yujiro Ogawa, for inviting me to study this field.

To the spirits of my beloved mother and elder sister, I will never forget the dearest persons forever.

References

Chapter1

Arthur, M. A., Carson, B., Von Huene, R., 1980. Initial tectonic deformation of hemipelagic sediment at the leading edge of the Japan convergent margin. In : Langseth, M., Okada, H. *et al.* (Eds.), *Initial Report of DSDP* 56/57, 569-613.

Bagnold, R.A., 1946. Motion of waves in shallow water, interaction between waves and sand bottom. *Proceedings of Royal Society of London* 187, A., 1-18.

Brothers, R. J., Kemp, A. E. S., Maltman, A. J., 1996. Mechanical development of vein structures due to the passage of earthquake waves through poorly-consolidated sediments. *Tectonophysics* 260, 227-244.

Cowan, D. S., 1982. Origin of 'vein structure' in slope sediments on the inner slope of the Middle America Trench off Guatemala. In: Von Huene, R., Aubouin, J. *et al.* (Eds.), *Initial Report of DSDP* 57, 645-50.

Hanamura, Y., Ogawa, Y., 1993. Layer parallel faults, duplexes, imbricate thrusts, and vein structures of the Miura Group: Keys to understanding the Izu forearc sediment accretion to the Honshu forearc. *The Island Arc* 3, 126-141.

Helm, R., Vollbrecht, A., 1985. Brittle-ductile shear zones in slope sediments off Guatemala, Site 568 and 569, Deep Sea Drilling Project Leg 84. *Initial Report of DSDP*.

Inokuchi, M., 1975. Hydrology of drift and flow sands. *Kokinshoin*, Tokyo, 290pp.

Kemp, A.E.S., 1990. Fluid flow in "vein structures" in Peru forearc basins: Evidence from back-scattered electro microscope studies. In: Suess, E., von Huene, R., et al. (Eds.), *Proceedings of ODP,* Scientific Results 112, 33-41.

Kemp, A.E.S., Lindsley-Griffin, N., 1990. Variations in structural style within Peruvian forearc sediments. In: Suess, E., von Huene, R., *et al.*, (Eds.), *Proceedings of ODP,* *Scientific Results* 112, 17-31.

Knipe, R.J. 1986. Microstructural evolution of vein arrays preserved in Deep Sea Drilling cores from the Japan Trench, Leg 57. *Geological Society of America Memoir* 166, 75-87.

Leggett, J. K., Lundberg, N., Bray, C. J., Cadet, J. P., Karig, D. E., Knipe, R. J., von Huene, R. 1987. Extensional tectonics in the Honshu forearc, Japan: integrated results of Deep Sea Drilling Project Legs 57, 87, and reprocessed seismic reflection profiles. *Geological Society of London,* Special Publication 28, 593-609.

Lindsley-Griffin, N., Kemp, A., Swartz, J.F. 1990. Vein structures of the Peru margin, Leg 112. In: Suess, E., von Huene, R., *et al.,* (Eds.), *Proceedings of ODP*, Scientific Results 112, 3-16.

Ogawa, Y., 1980. Beard-like veinlet structure as fracture cleavage in the Neogene siltstone in the Miura and Boso Peninsulas, central Japan. *Science Report, Department of Geology,* Kyushu University, Japan 13, 321-327.

Ogawa, Y., Miyata, Y., 1985. Vein structure and its deformation history in the sedimentary rocks of the Middle America Trench slope off Guatemala, Deep Sea Drilling Project Leg 84. In von Huene, R., Aubouin, J., (Eds.), *Initial Report of DSDP*, Washington (U.S. Govt. Printing Office) 84, 811-529.

Ogawa, Y., Ashi, J., Fukioka, K. 1992. Vein structure and their tectonic implication for the development of the Izu-Bonin forearc, ODP Leg 126. In: Taylor, B., Fujioka, K. et al. (Eds.), *Proceedings of ODP,* Scientific Results 126, 195-207.

Ohsumi, T., Takami, Y., Ogawa, Y. 2002, Tectonic Interpretation based on Riedel Shear Experiments and Analysis, *Geol. Soc. Japan*.

Ohsumi, T., Nagayama, T., Makinou, T. 2006. Study of detection system for debris flows, earthquakes and noise by vibration sensor. *Journal of Sabo Society* 59, 38-43.

Skempton, A. W. 1966. Some observations on tectonic shear zones. *Proceedings of the International Congres on Rock Mechanics, 1st Lisbon* 1, 329 -35.

Yalin, M. S. 1972. Mechanics of sediment transport. *Pergamon Press*, Oxford, U.K., 290pp.

Chapter2

Aki, K., and Richards, P. G. 2002, Quantitative Seismology, second edition, *University Science Books*, Saualito, California, 80 p.

Cristallini, E.O., Giambiagi, L., and Allmendinger, R.W. 2004, True three-dimensional trishear: A kinematic model for strike-slip and oblique-slip deformation. *GSA Gulletin*, v. 116, p. 938-952.

Dresen, G. 1991, Stress distribution and the orientation of Riedel shears, *Tectonophysics*, v. 188, p. 239-247.

Geographical Survey Institute of Japan, 2005, *Numerical Map 50 m Grid (Elevation)*, Second Edition, Tsukuba, Japan, p. 366.

Hori, T. 2006, Mechanisms of separation of rupture area and variation in time interval and size of great earthquakes along the Nankai Trough, southwest Japan, *Journal of Earth Simulator*, v. 5, p. 8-19.

Kanaori, Y. 1997, Fault Systems and their Activity, Kinmiraisha, Tokyo, Japan, p. 33.

Maruyama, T., 1963, One the force equivalents of dynamic elastic dislocations with reference to the earthquake mechanism, *Bulletin of the Earthquake Research Institute, University of Tokyo*, v. 41, p. 467-486.

Martel, S. 1997, Effects of cohesive zones on small faults and implications for secondary fracturing and fault trace geometry, *J. Struct. Geol.*, 19(6) , 835-847.

Mitchell, J. K. 1993, Fundamentals of Soil Behavior, *University of California, Berkeley, California.*

Nakata, T., and Goto, H. 1998, New geometric criteria for active fault segmentation; Fault branching and dip-slip distribution pattern along strike-slip faults, *Active Fault Research*, Research Group for Active Faults of Japan, v. 17, p. 43-53.

Naylor, M. A., Mandl, G., and Sijpesteijin, C. H. 1986, Fault geometries in basement-induced wrench faulting under different initial stress states, *Journal of Structural Geology*, v. 8, p. 737-752.

Ogawa, Y., Seno, T., Tokuyama, H., Akiyoshi, H., Fujioka, K., and Taniguchi, H. 1989, Structure and development of the Sagami Trough and off-Boso triple junction. *Tectonophysics*, v. 160, p.135-150.

Ogawa, Y., and Taniguchi, H. 1988. Geology and tectonics of the Miura-Boso Peninsulas and the adjacent area, *Modern Geology*, v. 12, p. 147-168.

Pubic Works Research Institute, Japan, 1998, Public Works Research Center, 17 Private Firms: Report of the Joint Research on Seismic Isolation Design of Underground Structures, *-Draft Manual for Seismic Isolation Design of Underground Structures-*, *PWRI Joint Research Report*, No.211, (in Japanease).

Riedel, W. 1929, Zur Mechanik geologischer Brucherscheinungen, Zentralbruch der Mineraloisch, *Geologish und Palaeontolgie*, p. 354-368.

Skempton, A. W. 1966, Some observations on tectonic shear zone, *Proceedings of First International Congress of Rock Mechanics*, v. 1, p. 329-335.

Takami, Y. 2002, Tectonic Interpretation of Submarine Topography in the Sagami Bay Based on Riedel Shear Experiments, *Graduation Thesis, College of Natural Science,* University of Tsukuba, Japan, 35 p.

Tchalenko, J.S., and Ambraseys, N.N. 1970, Structural analysis of the Dasht-e Bayaz (Iran) earthquake fractures. *GSA Gulletin*, v. 81, p. 41-60.

Woodcock, N. H. and Fischer, M. 1986, Strike-slip duplexes, *Journal of Structural Geology*, v. 8, p. 725-735.

Chapter3

Ambraseys, N., C. Melville and R. Adams. 1994, The Seismicity of Egypt, Arabia and the Red Sea, *Cambridge University Press*, Cambridge.

Fischer, K. D. 2007 , Modelling the 365 AD Crete Earthquake and its Tsunami, *Geophysical Research Abstracts*, Vol. 9, 09458.

Flemming, N.C. 1978, Holocene eustatic changes and coastal tectonics in the northeast Mediterranean: implications for models of crustal consumption. Philos. *Trans. R. Soc. London, Ser. A*, 289 (1362): 405-458 + Appendix I.

Hori, T. and Kaneda, Y. 2013, Giant earthquakes and tsunamis in the world: Mediterranean Sea, *Report of CCEP* 89.

Irikura, K. 1986, Prediction of Strong Acceleration Motion using Empirical Green' s Function, *Proc. 7th Japan Earthquake Engineering Symposium*, 151-156.

Karagianni, E.E. 2005 , Shear velocity structure in the Aegean area obtained by inversion of Rayleigh waves, *Geophysical Journal International*, 160, 1, 127-143.

Kamae, K.and Irikura, K. 1994 , Simulation of Seismic Intensity Distribution During the 1946 Nankai Earthquake Using a Stochastically Simulated Green's Function, *Proc. of 9th Japan Earthquake Engineering Symposium*, 1, 559-564.

Murotani, S., Satake, K. and Fujii, Y. 2013, Scaling relations of seismic moment, rupture area, average slip, and asperity size for M~9 subduction-zone earthquakes, *Geophysical Research Letters*, 40, 19, 5070–5074.

Ohsumi,T., Kaneko, F., Dixit, A., Fujitani, H. 2002, A Building Inventory of the Kathmandu Valley for Vulnerbility Analysis & Disaster Mitigation Planning, *11th The Japan Earthquake Engineering Symposium*, No.411, pp.2231-2236, 2002.

Okada, Y. 1992 ,Internal deformation due to shear and tensile faults in a half-space, *Bull.Seismol. Soc. Am.* 82, 1018-1040.

Papadimitriou, E. and Karakostas, V. 2008, Rupture model of the great AD 365 Crete earthquake in the south-western part of the Hellenic Arc, Acta Geophysica, 56, (2), 293–312.

Pirazzoli, P.A, Thommeret, J. Thommeret, Y., Laborel, J. and Montaggioni, LF. 1982, Crustal block movernents from Holocene shorelines: Crete and Antikythira (Greece) , *Tectonophysics*, 86, 27-43.

Pitazzoli, P.A., Laborel, J., Stiros, S. C. 1996 , Earthquake clustering in the Eastern Mediterranean during historical times, *Journal of geophysical research*, 101, B3, 6083-6097, Solid earth.

Pitazzoli, P.A. 1986, The Early Byzantine Tectonic Paroxysm. Z. Geomorph. N.F., Suppl.-Bd, 62, 31-49.

Ruff, L. and Kanamori, H. 1980, Seismicity and the subduction process, *Phys. Earth Planet.Inter*. 23, 240-252.

Shaw, B., Ambraseys, N., England, P.C., Floyd, M.A., Gorman, G.J., Higham, T.F.G., Jackson, J.A. 2008, *Nocquet, J.-M., Pain*, C.C., Piggott., M.D.

Segawa, S., Kaneko, F., Ohsumi,T., Kagawa, H., Fujitani, H. 2002, Damage Estimation of Buildings in Kathmandu Valley and Proposal for Improvement of the Earthquake-Resisting Capacity, *11th The Japan Earthquake Engineering Symposium*, No.410, pp. 2225-2230.

Sieberg, A. 1932, Isoseismal contours crete ad 365 crete earthquake intensity Isoseismal contours crete, *Untersuchungen uber Erdbeben und Bruchschollenbau im Oestlichen Mittelmeergebiet*, Jena: [s.n.], BA49737430.

Stiros, S. C. 1996, Late Holocene relative sea level changes in SW Crete: evidence of an unusual earthquake cycle, *Annali di geofisica*, 39 (3), 677-687.

Stiros, S. C. 2010, The AD 365 Crete earthquake and possible seismic clustering during the fourth to sixth centuries AD in the Eastern Mediterranean: a review of historical and archaeological data, *Journal of Structural Geology*, 23, 545-562.

Thommeret, Y., Thommeret, J., Pirazzoli, P.A., Montaggioni, L.F. and Laborel, J. 1981, Nouvelles donnees sur les rivages souleves de I'Holocene dans l'ouest de la Crete, Oceanis, 7 (4): 473-480.

Toda,S., Stein, R. S., Sevilgen,V. and Lin, J., Coulomb 3.3 Graphic-Rich Deformation and Stress-Change Software for Earthquake, Tectonic, and Volcano Research and Teaching--User Guide, *Revision History for USGS Open-File Report 2011-1060*, October 4, 2011, http://pubs.usgs.gov/of/2011/1060/

Wyss, M. and Baer, M. 1981, Earthquake Hazard in the Hellenic Arc, *Maurice Ewing Series*, Vol. 4, pp. 153-172.

Chapter4

Chen, Y. and Yanxiang, Y. 2007, Characteristics of response spectra for long-periods of main-shock recordings of the Chi-Chi earthquake, *Earthquake Engineering and Engineering Vibration*, Volume 6, Issue 2, pp 111-121, June 2007.

Forestry Agency Tohoku Forest Management Bureau, Ministry of Agriculture, 2008, Forestry and fisheries (MAFF), *Mountains disaster Study Measures Handouts of the 2008 Iwate-Miyagi Nairiku Earthquake* (in Japanese).

Goto, H., 2008. A summary of an earthquake / earthquake ground motions in the 2008 Iwate-Miyagi Nairiku Earthquake, 2008 (in Japanese).

Hata, Y., Ohsumi, T., Nozu, A., and Kamai, T. 2010, Evaluation of the strong motion at the Aratozawa site induced by the 2008 Iwate-Miyagi Nairiku Earthquake based on empirical site amplification and phase effects, *Journal of the Japan Landslide Society*; ISSN:1348-3986; VOL.47; NO.5; PAGE.247-254 (in Japanese with English abstruct).

Hayashi, Y., Morii, Y. 2008, The 2008 Iwate-Miyagi Nairiku Earthquake (in Japanese).

Inoguchi, T., Oyagi, N., Uchiyama, S. 2010, And Snimizu, F., Topographical and Geological Features of Landslide Disasters Caused by the 2008 Iwate-Miyagi Nairiku Earthquake, *Natural Disaster Research Report of the National Research Institute for Earth Science and Disaster Prevention*, 43 (in Japanese with English abstruct).

Irikura, K. 1986, Prediction of Strong Acceleration Motion using Empirical Green’s Function, *Proc. 7th Japan Earthquake Engineering Symposium*, 151-156.

Miyagi, T. 2008, Flash report of the 2008 Iwate-Miyagi Nairiku Earthquake, *Japanese Geotechnical Society* (in Japanese).

Nakamura, S. 2008, Flash report of the 2008 Iwate-Miyagi Nairiku Earthquake, Emergency Survey on joint team of the Japanese Geotechnical Society, the Japan Association for Earthquake Engineering and the Japan Landslide Society, *JSCE Magazine*, pp.42-45, vol.93 no.8 (in Japanese).

Nozu, A. 2008, Source model for the 2008 Iwate-Miyagi Nairiku Earthquake (in Japanese with English abstract), *PARI research note*, No.30.

Nunohara, K., Yoshida, T., Yamada, R. 1999, Relationship between earthquake disasters and caldera structures using of GIS, *The Geological Society of Japan* (in Japanese with English abstract), http://www.geosociety.jp/hazard/content0035.html

Yoshida T, Nagahashi Y, Oguchi T, Ohira H, Aizawa K, Sato H, *et al.* 1999, Geohistory of the active periods of volcanoes and the formation of Late Neogene calderas in northeastern Honshu Arc. *Chikyu Monthly/Extra* 27: 123–129 (in Japanese).

Zifa, W. 2008, A preliminary report on the Great Wenchuan Earthquake, *Earthq Eng & Eng Vib* 7:225-234 DOI: 10.1007/s11803-008-0856-1.

Appendix

Boore, D.M., Stochastic simulation of high-frequency ground motions based on seismoogical models of the radiated spectra, *Bull. Seism. Soc. Amer.*, 73, 1865-1894,1983.

Central Disaster Management Council: On countermeasures for the Tokai Earthquake, (No, 11), 2001. http://www.bousai.go.jp/jishin/tokai/senmon/

Ikeda, T., Kamae, K., Miwa, S. and Irikura, K., Source Charactreization and Strong Ground Motion Simulation of The 2000, Tottori-ken Seibu Earthquake using The Empirical Green's Function Method, J.Struct. Constr. Eng., AIJ, No.561, 37-45, Nov., 2002. (in Japanese with English abstract)

Irikura, K., Prediction of strong acceleration motion using empirical Green's function, *Proceeding of 7th Japan Earthquake Symposium*, 151 – 156, 1986.

Irikura, K. and Kamae, K, Estimation of strong ground motion in broad-frequency based on a seismic source scaling model and an empirical Green's function technique, *Annali Di Geofisica*, **XXXVII** (6), 1721 – 1743, 1994.

Technical Standards and Commentaries for Port and Harbour Facilities in Japan, The Overseas Coastal Area Development Institute of Japan, 2007.

http://www.ocdi.or.jp/pdf/main-contents.pdf

Appendix

Chapter4 used the empirical Green's function method and **Chapter3** used the stochastic Green's function method.

Chapter4 have reproduced the waveforms of the main shock using the empirical Green's function method (Irikura, 1986) by using aftershock records of Aratozawa landslide site. The empirical and stochastic Green's function method is a technique to synthesize seismic records of a large event using the recorded data of small events as Green's functions. Following the recommendation of the Japan Society of Civil Engineering (JSCE), after the Southern Hyogo prefecture earthquake in 1995, the simulation of earthquake ground motions using the Green's function approach for a potential fault rupture, has been included in one of the seismic resistant design codes. Since the empirical Green's function method mainly depends on and uses small ground motion histories, small events selected as Green's functions should share the same path and site effects with the target event. Seismic waveforms recorded at the base of Aratozawa landslide site are suitable for this analysis, since seismic motion is less affected by sedimentary layers. The small earthquakes used as Green's functions should be selected in such a way that their source, path and site effects are similar with those of the main shock. The target site is located in the seismic fault area.

The empirical Green's function method is a technique to create the ground motion of large earthquakes waveform by the synthetic ground motion due to small and medium-sized events, such as aftershocks as Green's function. This method has the advantage of being able to create a ground motion that reflects the epicenter of the rupture process, pass-specific and site-specific characteristics. Schematic illustration of fault parameterization used for computing Green's functions is shown in **Fig. 1.**

Earthquake ground motions are the result of propagating waves in the earth medium originated from a seismic source. Therefore, it is natural to conclude that the artificially generated earthquake ground motions for the seismic design of structures must be developed, by reflecting on such physical wave propagation processes and then, these techniques depend on seismic source parameters as well as physical parameters of the crustal and surface soil structures through which the seismic waves propagate.

For practical applications, detailed design guidelines were required for the estimation of earthquake motion, such as how to select scenario earthquakes and how to deal with the uncertainty inherent in the fault rupturing mechanism of future events (*e,g.* Central Disaster Management Council (2001), Technical Standards and Commentaries for Port and Harbor Facilities in Japan (2007)）. As the development of the technique, Ikead *et al.* (2002) attempted to construct a source model for broad-band strong ground motions by the forward modeling using the empirical Green's function method.

In **Chapter3**, ground motions estimated by using the stochastic Green's function method. The stochastic Green's function method, which has been discussed in detail by Irikura (1986) and Irikura and Kamae (1994) is a method to simulate ground motions from an extended fault on the basis of the representation theorem of elastodynamics. The stochastic Green's function method is an effective technique when a proper observation record cannot be obtained. The stochastic simulation method for a point source (Boore, 1983) is a useful and practical tool to simulate strong ground motions. In Chapter3, this study was using only the phase characteristics of the observed seismic waves close to the assumed source in the Crete Island.

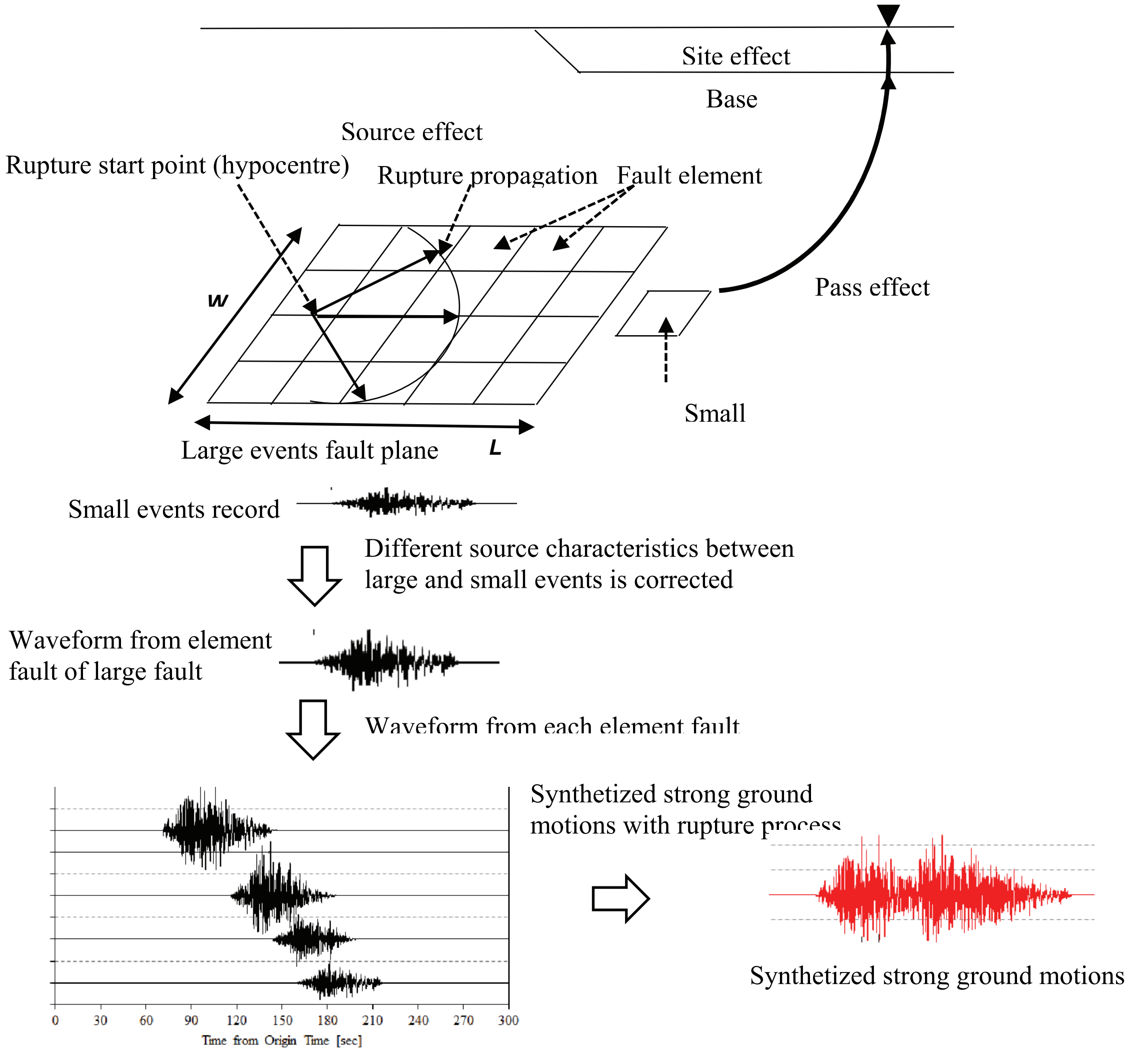

Fig.1. Schematic illustration of fault parameterization used for computing Green's functions. (modified from Generation Guide for Seismic Input Motions Based on recent Advancement of Ground Motion Studies)

The synthetic method of strong ground motions is studied to match the spectral scaling relation using empirical Green's function technique Irikura (1986). Irikura and Kamae (1994) used a generalized method for simulating strong ground motion from large earthquakes by summing sub-event records to follow the ω^2 law. c is the stress drop ratio. Then the subfault size is equivalent to the small event (hence-forth called subevent). $F_{ij}(t)$ is a filtering function to adjust a difference in slip time function between the large and small events. The seismogram *U(t)* for the target event is expressed in terms of the seismogram $c \cdot u(t)$ of the subevent as follows:

$$U(t) = \sum_{i=1}^{N_\mathrm{L}} \sum_{j=1}^{N_\mathrm{W}} \frac{r}{r_{ij}} \cdot F_{ij}(t) * \{c \cdot u(t)\} \qquad \text{(EQ.1)}$$

$$F_{ij}(t) = \delta(t - t_{ij}) + \frac{1}{n'} \cdot \frac{1}{1-e^{-1}} \sum_{k=1}^{(N_\mathrm{D}-1)n'} \exp\left(-\frac{k-1}{(N_\mathrm{D}-1)n'}\right) \cdot \delta\left\{t - \frac{(k-1)\tau}{(N_\mathrm{D}-1)n'} - t_{ij}\right\} \qquad \text{(EQ.2)}$$

$$t_{ij} = \frac{r_{ij} - r_0}{V_S} + \frac{\xi_{ij}}{V_r} \qquad \text{(EQ.3)}$$

where * represents the convolution, r is the hypocentral distance from the observation point to the subevent, r_{ij} is the distance from the observation point to the *ij-th* subfault, ζ_{ij} is the distance from the rupture nucleation point to the *ij-th* subfault, V_r is the rupture speed, τ is the rise time of the target event, n' is an appropriate integer to eliminate spurious periodicity, N_L (L=length), N_W (W=width) are number of large and small events, L and l are fault length, W and w are width, defined to be L x W and l x w, respectively. L_D is number of the dislocation model. Case of different stress drop between large and small events is corrected for a difference in stress drop between large and small events.